



ADVANCED ELECTROMAGNETIC METHODS FOR AEROSPACE VEHICLES

Semiannual Progress Report
(January 1 - June 30, 1993)

Handwritten:
11/1/93
91

N93-31036

Unclass

G3/32 0177078

by

Constantine A. Balanis
Weimin Sun
El-Budawy El-Sharawy
James T. Aberle
Craig R. Birtcher
Jian Peng
Panayiotis A. Tirkas
David Kokotoff
Frank Zavosh

(NASA-CR-193468) ADVANCED
ELECTROMAGNETIC METHODS FOR
AEROSPACE VEHICLES Semiannual
Progress Report, 1 Jan. - 30 Jun.
1993 (Arizona State Univ.) 91 p

Prepared by

Telecommunications Research Center
College of Engineering and Applied Science
Arizona State University
Tempe, AZ 85287-7206

Sponsored by

Grant No. NAG-1-1082
National Aeronautics and Space Administration
Langley Research Center
Hampton, VA 23665



Contents

I. INTRODUCTION	1
II. COMPOSITE MATERIALS	4
A. Introduction	4
B. Antenna Patterns of Low Conductivity Composite Materials	5
C. Guidelines of Green's Function Analysis of Composite Material Structures	8
D. FD-TD Modeling of Volumetric Composite Materials	10
E. FDTD Modeling of Pyramidal Horns With Composite E-plane Walls	11
F. Efficiencies of Horn Antennas Loaded with Composite Materials	14
III. ANTENNA TECHNOLOGY	44
A. Introduction	44
B. Cavity-Backed Microstrip Patch Antennas	44
C. Ferrite-Controlled Cavity-Backed Slot Radiators	48



I. INTRODUCTION

The Advanced Helicopter Electromagnetics (AHE) Industrial Associates Program has continuously progressed with its research effort focused on subjects identified and recommended by the Advisory Task Force of the program. The research activities in this reporting period have been steered toward practical helicopter electromagnetic problems, such as HF antenna problems and antenna efficiencies, recommended by the AHE members at the annual conference held at Arizona State University on October 28-29, 1992 and the last biannual meeting held at the Boeing Helicopter on May 19 - 20, 1993. The main topics addressed include

- Composite Materials
- Antenna Technology

and the research work on each topic is closely tied with the AHE Consortium members' interests. Significant progress in each subject is reported.

Special attention in the area of Composite Materials has been given to:

- a. Modeling of material discontinuity and their effects on towel-bar antenna patterns;
- b. Guidelines for composite material modeling by using the Green's function approach in the NEC code;
- c. Measurements of towel-bar antennas grounded with a partially material-coated plate.
- d. Development of 3-D volume mesh generator for modeling thick and volumetric dielectrics by using FD-TD method;
- e. FDTD modeling of horn antennas with composite E-plane walls;
- f. Antenna efficiency analysis for a horn antenna loaded with composite dielectric materials.

The research in the area of Composite Materials has long been focused on 1) Analytic modeling of composite sheets by using the Green's function approach; 2) Evaluation of their equivalent surface impedances; 3) NEC code simulation by taking into account of the surface impedances of the materials. Some simple composite geometries such as the thin plate, wedge, and square plate grounded monopole have been previously designed to verify the Green's function approach in composite material modeling. Using the surface impedance concept, the approach showed encourage agreement with measurements. Based on these previous work, this technique has been coupled into the NEC code to provide an equivalent surface impedance distribution, which is subsequently used by the NEC code for pattern predictions. To provide a guideline for using the surface impedance concept in antenna modelings, some conclusive remarks are provided in the report to help the AHE consortium members in their numerical work.

In addition to the Green's function modeling technique, the FD-TD has been demonstrated in previous reports to be a powerful and accurate technique in dealing with composite structures. The direct application of the technique or direct use of an FD-TD code solely relies on the discretization of a complex geometry. In previous research periods, an FD-TD mesh generator has been developed; however it is based on surface mesh generation which is only applicable to objects consisting of conducting surfaces and thin dielectrics. The work on FD-TD modeling in this period has been extended by developing the volume FD-TD mesh generator. The automatic 3-D volume mesh generation allows the modeling of geometries involving thick and volumetric composite materials. To demonstrate the 3-D volume mesh generation, the numerical modelings of a lossy dielectric sphere and a grounded monopole on a thick composite substrate are reported.

Antenna efficiency and pattern control are key issue in design of antennas mounted on helicopter platforms, especially when the antennas are loaded with lossy composite materials. In this report, the work on antenna efficiency modeling and bandwidth improvement of a horn antenna loaded with composite sheets is discussed.

In the area of Antenna Technology, new progresses have been achieved primarily in investigations of cavity-backed microstrips and arrays, and ferrite-loaded cavity-backed slots. These cavity-backed antennas are not only conformal to airplane fuselage, but also overcome the tradeoff between bandwidth and scan volume in an array, or provide tunable characteristics. Most

importantly, these antennas have a potential use in UHF or even VHF frequencies. In the past, a two-dimensional analytical model of a magnetically-tuneable cavity-backed slot antenna was introduced. In this report, a three-dimensional analytical model of a cavity-backed slot antenna is provided with specific intent of analyzing the tuning capabilities of such an antenna at VHF and UHF frequencies. While the theoretical analysis work is on going, some fundamental experiments on these ferrite-loaded cavity backed antennas have also been conducted. More interesting experiment results of S-parameter measurements are reported. These measurements provide some valuable insights for exciting the cavity-backed antennas by using microstrip lines.



II. COMPOSITE MATERIALS

A. Introduction

The research in the area of Composite Materials has long been focused on the modeling of composite materials on complex structures by the approach of

- a. Analytic modeling of composite sheets by using the Green's function technique;
- b. Evaluation of their equivalent surface impedances;
- c. NEC code simulation taking into account of the surface impedance of the materials.

Some composite geometries, such as the thin plate, wedge and square plate grounded monopole, have been previously designed to verify the Green's function approach in composite material modeling. Using the surface impedance concept, the approach showed encouraging agreement with measurements. Based on the results of the previous work, this technique has been coupled into the NEC code to provide an equivalent surface impedance distribution, which is subsequently used by the NEC code for pattern predictions. Using this approach, numerical investigation on the radiation of a towel-bar antenna grounded with material discontinuity has been conducted. The results are compared with experiments performed at ASU. Moreover, to provide a guideline for using the surface impedance concept in antenna modelings, some conclusive remarks are provided in the report to help the AHE consortium members in their numerical work.

In addition to the Green's function modeling technique, the FD-TD has been demonstrated in the previous reports to be a powerful and accurate technique dealing with composite structures. The theory of FD-TD has been very well developed. The direct application of the technique or direct use of an FD-TD code solely relies on the discretization of a complex geometry. For a complex structure involving composite materials, the FD-TD mesh generation is not a easy task. In previous research periods, an FD-TD mesh generator has been developed; however it is based on surface mesh generation which is applicable to objects consisting of conducting surfaces and thin

dielectrics. The work on FD-TD modeling in this period has been extended by developing the volume FD-TD mesh generator. The automatic 3-D volume mesh generation allows the modeling of geometries involving thick and volumetric composite materials. To demonstrate the 3-D volume mesh generation, the numerical modelings of a lossy dielectric sphere and a grounded monopole on a thick composite substrate are reported

The recent research revealed a significant improvement in bandwidth of a horn antenna loaded with composite materials. It was found that the FDTD method coupled with the contour path integrals is a robust approach to model this type of antennas. New results on radiation patterns of a horn loaded with composite materials have been obtained numerically and experimentally. They are presented in the report.

Antenna efficiency is a key issue in design of antennas mounted on helicopter platforms, especially when the antennas are loaded with lossy composite materials. The research on this subject has been recommended by the AHE Advisory Task Force at the biannual meeting held at the Boeing Helicopter on May 19 -20, 1993. In this report, the work on antenna efficiency modeling of a horn antenna loaded with composite sheets is described.

B. Antenna Patterns of Low Conductivity Composite Materials

1. Introduction

The objective of this work is to model low conductivity composite materials on antenna systems, mounted on helicopter platforms. Preliminary work has been done in this area last year, but further investigation and verification is required. In our previous reports we presented theory and measurements of:

- a. Antenna and RCS patterns on composite materials of high conductivity such as graphite epoxy and fiberglass with screens near the surface.
- b. Antenna patterns on composite materials of low conductivity including microwave absorbers.
- c. RCS patterns of low conductivity materials.

In the above cases, the surface impedance of the composite material is evaluated using a spectral domain Green's functions approach and utilized

to model the structure under investigation as a wire grid. The pattern of the structure is then computed using the wire grid option of NEC code. Monopole antennas on composite materials have been built and tested. Good agreement between predictions and measurements of radiation patterns of these antennas have been observed. The RCS patterns of structures made of composite materials were also predicted and are in good agreement with measurements.

In this report, the analysis criteria, developed and presented in our 1992 annual progress report, are tested and verified for the towel bar antenna. The towel bar antenna is used quite often in modern helicopter platforms and has certain advantages in composite material structures. This report shows that the radiation efficiency of towel bar antenna may not be reduced by implementing composite materials in the helicopter structure. The difference in absolute values of the measured patterns for the radiated fields is only about 1 dB.

2. Theory

It has been shown in our previous reports that the surface impedance Z_s of a two-layer media including a layer of composite material, can be written as

$$\bar{Z}_s = (\bar{T}_E + \bar{Z}_T \bar{G}_s)(\bar{Y}_T + \bar{T}_J \bar{G}_s)^{-1} \quad (1)$$

$$\bar{G}_s = \bar{T}_{LJ} \bar{Z}_{LT}^{-1}$$

where \bar{Z}_T , \bar{Y}_T , \bar{T}_E , \bar{T}_J are the transmission matrices of the composite material and the subscript L denotes the medium below the composite material. At the limit when the thickness d of the bottom layer equal zero, the surface impedance becomes

$$\bar{Z}_s = \bar{Z}_T \bar{T}_J^{-1} \quad (2)$$

If the structure under investigation is to be modeled using the two-impedance sheet method, as discussed in our previous progress reports, the contributions of the ground plane are duplicated. The surface impedance in (1) assumes a ground plane at the back of the composite material. In addition, a PEC sheet is introduced again in the two-sheet wire grid model. This

is most likely to increase the predicted RCS and antenna patterns of composite materials. To solve this problem, the free space ground plane admittance is subtracted from the above surface admittance as

$$\bar{Z}_s^m = (\bar{Y}_s - \bar{Y}_s^a)^{-1} \quad (3)$$

where \bar{Y}_s^a is the free space admittance (can be found using (2)) and \bar{Z}_s^m is the modified surface impedance to avoid the inclusion of the ground plane twice.

3. Measurements and Predictions of Towel bar Antenna Patterns on Composite Materials

To show the effects of composite materials on the towel bar antenna patterns, a bar antenna was measured at 4 GHz and 5 GHz on a 6"x6" ground plane. The ground plane was partially covered with a 6"x3" microwave absorber (Figure 1). The thickness of the absorber was 40.0 mil (about 1.0 mm). The length and the height of the antenna were 3" and 0.3", respectively. As shown in Figures 2 and 3, the measured patterns of the towel bar antenna on composite materials were slightly different from the pattern of the same antenna on PEC (the composite material is removed). Thus, the radiation efficiency is not significantly sacrificed due to the composite material. In fact, at 4 GHz, the measured gain of the antenna increased by adding the composite material. This can be explained by the fact that, the image of the towel bar antenna counteracts the antenna element itself. This usually occurs when the antenna current is parallel to the ground plane. The composite material in this case weakens the effects of the image resulting in the observed improvement in the radiation pattern. This in contrast with other types of antennas, such as the monopole antenna, where the image co-acts with the antenna. This occurs when the antenna current is perpendicular to the ground plane. In this case, the reduction in the radiation efficiency due to composite materials can be significant. As presented in our 1992 annual progress report, the effect of the composite material on monopole antennas is to reduce the overall pattern by as much as 10 dB.

We measured the material properties between 8.2-12.4 GHz using the waveguide technique. The measured properties were then interpolated to $\epsilon_r = 14.9 - j0.1$, $\mu_r = 2.0 - j1.6$ at 5 GHz. The structure was modeled as two wire

grids with upper grid loaded with the computed surface impedance of the composite material ($6+j38$ ohms). The ratio of the mesh size of the upper grid (the composite material surface) to the wire radius was about 7. In the computation, only one value of the surface impedance, calculated at a radiation angle of 45° , was used. Initially, we had numerical problems in running the NEC code to model the above structure. These numerical problems were attributed to the presence of an excitation nearby the edge of the composite material. The edge singularity interfered with the calculations and resulted in a negative value of the input impedance of the antenna. This problem was solved by connecting the edges to the ground plane. The computed versus measured radiation patterns at 5 GHz are shown in Figures 4 and 5. The measured and computed patterns of the antenna on a PEC are also displayed in Figures 4 and 5. Reasonably, good agreement is observed between theory and measurements, except at the back of the antenna where the discrepancy was about 4 dB. This is expected since the feed cables and circuits are not included in the model.

4. Conclusion

The effects of low conductivity composite materials on the towel bar antenna patterns is analyzed and presented. The code has been validated by computing the surface impedance and comparing predicted patterns to measurements of an antenna partially covered with a microwave absorber material. Small differences in the pattern of the towel bar antenna was observed due to the inclusion of composite materials in the structure. This suggests that the towel bar antenna may be an attractive antenna for platforms that employs composite materials of low conductivity.

C. Guidelines of Green's Function Analysis of Composite Material Structures

The objective of this section is to develop parameters and criteria necessary for accurately predicting and analyzing the effects of composite materials on antenna systems mounted on helicopter platforms. The analysis employs the concept of the equivalent surface impedance. The surface impedance of the composite material is evaluated using a spectral domain Green's functions approach and is utilized to model the composite material structure as a wire

grid. The electromagnetic characteristics of the structure are then computed using the wire-grid option of the NEC code. The parameters and criteria for using the wire grid model are:

- Wire radius; for PEC the wire radius can be chosen with a great deal of flexibility and is usually equal 0.01λ . For composite materials, the radius should equal the thickness of the composite material for best agreement with measurements. If there is a ground plane at the back of the composite material, the radius is chosen slightly less than the thickness of the composite material to avoid contact between the wire grid representing the composite material and the wire grid representing the ground plane.
- Mesh size; the standard mesh size is $0.1\lambda \times 0.1\lambda$ for PEC. The mesh size for composite materials has to be chosen such that the surface area of the wire equal approximately the surface area of the composite material. A typical ratio between the size and the radius of the wire is 7. Since the radius equal approximately the thickness, the mesh size is about 7 times the thickness. As the thickness of the composite material gets smaller compared to wavelength, a finer wire and smaller mesh is required to model the composite material.

Work, as discussed in the previous section, has been done to verify the above criteria. The predicted RCS patterns of structures made of composite materials were in good agreement with measurements. Also, monopole antennas on low conductivity composite materials have been built and tested. Good agreement between predictions and measurements of radiation patterns of these antennas has been observed.

The radiation characteristics of towel bar antennas have also been presented. The radiation efficiency of a towel bar antenna may not be reduced by implementing composite materials in the helicopter structure. The difference in the measured patterns values for the radiated fields is only about 2 dB. Our prediction for this type of antenna shows some discrepancy due to the interference of edge singularities and the calculations of the antenna input impedance. Without some precautions, the edge singularity may even result in a negative input impedance in which case the NEC code terminates the calculations prematurely. We detected this problem with an all PEC

towel bar antenna. This leads to the conclusion that this problem is inherent with the NEC code itself. In a personal discussion with Dr. Granzella from ESL, a subsidiary of TRW, he confirmed the same problem with the NEC code.

The above problem can be due to numerical inaccuracy or lack of the appropriate boundary conditions. To insure that this problem is not due to the latter, the NEC code was utilized to plot the current distribution of a $\lambda/2 \times \lambda/2$ sheet of composite material due to a plane wave incident at an angle $\theta = 45$ degrees, as shown in Figure 6. The material has a surface impedance of $5+j5$ ohms. Figures 7 and 8 shows the current distribution on the sheet. The current behavior shows that the NEC code predicts the appropriate current edge conditions; the perpendicular currents vanish at the edges and the parallel currents increase near the edge.

In conclusion, we found that the Green's function approach provides good results in all cases that we tested except when an edge singularity is close to the excitation of the antenna. The combination of the Green's function surface impedance software/NEC code can handle a wide variety of scattering and antenna structures, including composite material with or without a metal backing.

D. FD-TD Modeling of Volumetric Composite Materials

The FD-TD has been demonstrated in the previous reports to be a powerful and accurate technique in dealing with composite structures. The direct application of the technique or direct use of an FD-TD code solely relies on the discretization of a complex geometry. Previously, an FD-TD mesh generator has been developed; however it only allows surface mesh generation. Thus it can only be used for objects consisting of conducting surfaces and thin dielectrics. Recently we developed a 3-D volume FD-TD mesh generator. The automatic 3-D volume mesh generation allows the modeling of geometries involving thick and volumetric composite materials. The algorithm used for 3-D volume mesh generation is based on the previous surface mesh generation algorithm and the algorithm connecting volume mesh from boundary (or surface) elements. The 3-D volume mesh generation has been tested by modeling a lossy dielectric sphere and a monopole antenna grounded with

both conducting and thick composite substrate.

First, a dielectric sphere shown in Figure 9 was tested. The sphere has been used only as a demonstration simply because of the availability of analytic solutions. The sphere has a radius of one half wavelength and its permittivity is $\epsilon_r = 2.0$, conductivity $\sigma = 0.001$, and permeability $\mu_r = 1.0$. The sphere is illuminated by a plane wave incident in the negative z -direction and polarized in x -direction at 300 MHz. A FD-TD lattice is automatically generated by the 3-D volume mesh generator with 30 cells per wavelength. The radar cross sections of the sphere in the planes of $\phi = 90^\circ$ and $\phi = 0^\circ$ are plotted in Figures 10 and 11. The FD-TD predictions have been compared with the exact solutions of Mie Theory. It is seen that the FDTD results agree with the Mie Theory quite well except in the backscattered directions. This discrepancy is due to the error of the stair-case modeling of smooth spherical surfaces.

The second example tested was a monopole antenna mounded on a ground plane. But the ground plane is placed on a very thick composite substrate. The geometry of problem is shown in Figure 12 where the ground plate is 2λ by 2λ and the composite is one λ thick. The electric parameters of the composite material is the same as that used in the first example. The antenna radiation patterns in three principal planes are plotted in Figures 13 - 15. The significant backlobes, due to the contribution of the material substrate can be seen in the patterns.

From the two examples, it is seen that the FD-TD method plus the 3-D volume mesh generator will facilitate the modeling of volumetric composite materials by using the FD-TD technique. This approach is fairly accurate and versatile, and can be applied to composite platforms such as helicopter tails and wings. In the following research period, antennas grounded on composite platforms will be modeled by using this technique, and the consequent results will be reported.

E. FDTD Modeling of Pyramidal Horns With Composite E-plane Walls

The Contour-Path Finite-Difference Time-Domain (CPFDTD) method is getting more widespread attention since its introduction to the electromagnetics community [1, 2]. The CPFDTD method is primarily suited for mod-

eling structures that cannot be gridized using the standard Yee's rectangular or cubic grid. The method modifies the grid near the surface of the curved structure only and retains its basic cubic grid in the remaining computational domain. The magnetic field components in the distorted grid are updated through modified equations that assume no field variation within the distorted area. The second-order accurate central difference approximations are, therefore, reduced to first-order approximations only at the grid points near the structure surface and retain their second-order accuracy elsewhere in the domain. Distorting the electric field contours is avoided by the method. The electric field points where necessary are obtained through a "near neighbor" approximation, i.e., if a field value is not available, the value of the field component closest to the component that is required is taken. The CPFDTD approach presents an efficient and still accurate approach to extend the application of the conventional FDTD method to model smoothly curved surfaces.

1. Analysis of Pyramidal Horn Antennas

The application of the staircase FDTD method to model pyramidal horn antennas was reported in [3]. It was found that to obtain acceptable radiation patterns, compared to measured ones, grid sizes on the order of 30 cells per wavelength were required. It is demonstrated here that using the CPFDTD method with 12 cells per wavelength yields accurate antenna gain patterns. For this application, seventh-order accurate absorbing boundary conditions as reported by Tirkas, Balanis and Renaut [4] were used.

The flared parts of the antenna surface are modeled by distorting the contours that update the magnetic field components next to the antenna surface. Distorting the electric field contours is avoided. In the E-plane direction the contours for the x and z components of the magnetic field are distorted to conform to the antenna surface. In the H-plane direction, the contours for the y and z components of the magnetic field are distorted.

Furthermore, modifications were made in the basic CPFDTD approach to include the effect of electrically thin (less than the size of the FDTD cell) magnetic coatings. When magnetic materials are applied in the E-plane walls of the pyramidal horn, diffractions from the antenna edges are reduced. This results in reduced side lobe levels in the backside of the antenna. Depending on the extent to which the E-plane wall is coated, nearly symmetric E-plane

and H-plane antenna patterns can be obtained.

2. Numerical Results

In this section we present some of the computed antenna patterns that were obtained from a $5'' \times 5''$ square aperture pyramidal horn antenna and compare them with measurements. The geometry of the horn is shown in Fig. 16. The frequency of operation was 10 GHz. The aperture of the antenna was $5'' \times 5''$, whereas the waveguide aperture was of standard X-band dimensions, i.e., $0.9'' \times 0.4''$. The transition length from the waveguide aperture to the antenna aperture was $10.5''$. A section of $3''$ long composite material was then glued on the upper and lower E-plane walls as shown in Figure 16. The electrical parameters of the composite material were measured to be $\epsilon_r = 15.95 - j0.45$ and $\mu_r = 1.58 - j1.18$ and its thickness was 40 mils.

The grid size was $0.1''$ (about 12 cells per wavelength), i.e., the waveguide was 9×4 cells whereas the antenna aperture was 50×50 cells. The distance from the waveguide transition to the antenna aperture was 105 cells. Between the antenna and the outer boundary 14 cells were allowed. The overall grid size was $78 \times 78 \times 144$ cells. The CPFDTD program was run for 40 cycles to reach steady state, on a RISC/6000. The CPU time was 4,200 seconds for obtaining the E- and H-plane gain patterns over 360° (at 1° steps). Figure 17 exhibits the computed E-plane gain pattern of the antenna without the presence of composite material and compares it with measurements. The agreement between the CPFDTD results and measurements is very good. Figure 18 compares the computed gain pattern in the H-plane with measurements.

Figure 19 compares the E-plane pattern of the same antenna with measurements when the lossy coating in the E-plane wall is applied. With the application of composite material the maximum gain at broadside is reduced by 1.6 dB, but the first side lobe in the pattern is eliminated. The side lobes in the backside of the antenna are also much lower with the composite wall.

3. Conclusions

The CPFDTD method was used for analysis of pyramidal horn antennas with or without composite E-plane walls. For the metallic horn very accurate antenna gain patterns were computed and compared to measurements.

When the E-plane walls are coated with lossy magnetic material, for gain pattern control, the CPFDTD yields acceptable gain patterns compared to measurements.

F. Efficiencies of Horn Antennas Loaded with Composite Materials

The antenna patterns of a horn loaded with composite materials have been predicted by using the FD-TD method and reported in the previous section. However the antenna efficiency has not been discussed. The analysis of antenna efficiency can also be performed by using the same FD-TD technique. Specifically, the contour path finite-difference time domain (FDTD) method was used for modeling pyramidal horns with or without composite E-plane inner walls. To model the pyramidal horn surface, a locally distorted grid was used. Modified equations are obtained based on the locally distorted grid and the assumptions of the contour path method, which was briefly introduced in previous progress reports. The developed algorithm was validated by comparing computed antenna gain patterns, with and without the presence of composite material, with available measurements. The approach to calculate the horn input power, E- and H-plane gain patterns, radiation power and antenna radiation efficiency is outlined and numerical results are presented.

1. Pyramidal Horn Antenna Input Power, E- and H-plane Gain Patterns, Radiated Power and Radiation Efficiency

The geometry of a partially coated pyramidal horn is shown in Fig. 16. A section of composite material of thickness t and length l_m is placed on the upper and lower E-plane walls of the horn for pattern control purposes. The effect of the lossy material on the antenna performance is analyzed in this section.

The pyramidal horn was fed by a rectangular waveguide operating in the dominant TE_{10} mode whose tangential electric field at the aperture is represented by

$$E_y(x, y, z) = E_0 \sin\left(\frac{\pi}{a}x\right) \sin(\omega t - \beta_z z) \quad (4)$$

where $0 \leq x \leq a$ and $0 \leq y \leq b$. The constant β_z represents the waveguide propagation constant. At the reference feed plane, $\beta_z z$ was set to zero.

Using this feed scheme, the input power to the horn was estimated by integrating the input power density over the waveguide cross section, and it is given by

$$P_{10}^{input} = \frac{1}{2} E_0^2 \left(\frac{\beta_z}{\omega \mu_0} \right) \left(\frac{ab}{2} \right) \quad (5)$$

The radiated far-zone E_θ and E_ϕ electric fields are obtained from the FDTD code through a near-to-far field transformation. The E-plane gain pattern was calculated using

$$G_E(\theta, \phi = 90^\circ) = \frac{4\pi E_\theta^2(\theta, \phi = 90^\circ)}{P_{10}^{input}} \quad (6)$$

Similarly, the H-plane gain pattern was calculated using

$$G_H(\theta, \phi = 0^\circ) = \frac{4\pi E_\phi^2(\theta, \phi = 0^\circ)}{P_{10}^{input}} \quad (7)$$

The antenna radiated power was estimated by integrating the far-zone fields over a sphere, and it is represented by:

$$P^{rad} = \int_0^\pi \int_0^{2\pi} U(\theta, \phi) \sin \theta d\theta d\phi \quad (8)$$

where $U(\theta, \phi)$ is the radiation intensity and is given by

$$U(\theta, \phi) = \frac{1}{2\eta_0} [|E_\theta(\theta, \phi)|^2 + |E_\phi(\theta, \phi)|^2] \quad (9)$$

where $\eta_0 = 120\pi$ is the free-space impedance. One important design parameter of pyramidal horns with lossy materials on the E-plane walls is the power loss or the antenna efficiency calculated using

$$\eta = \frac{P^{rad}}{P_{10}^{input}} \quad (10)$$

2. Numerical Results

A 20-dB standard gain pyramidal horn antenna with conducting inner walls was analyzed using the contour path FDTD method. Figs. 20 and 21 compare the computed E- and H-plane gain patterns, respectively, of the pyramidal horn with measurements. As illustrated by both figures, there is very good agreement between the computed and measured results over a dynamic range of 60 dB. The computed gain patterns agree very well with the measured ones when a standard cell size of $\lambda/12$ was used (0.1"). The overall FDTD grid required for this problem was $76 \times 60 \times 142$ cells. This simulation was run for 40 cycles to reach steady state and took about 2,500 seconds on an IBM-RISC/6000 computer for computing the E- and H-plane gain patterns over 360° at 1° steps.

The antenna radiation efficiency for the pyramidal horn with conducting walls was estimated by integrating the far-zone fields to obtain the radiated power. The amplitude of the y-directed electric field was set equal to $E_0 = 1$ V/m producing a reference input power of $P_{10}^{input} = 0.116226 \times 10^{-6}$ Watts. By evaluating the far fields and then integrating them (1° step), the radiated power was estimated to be $P^{rad} = 0.115077 \times 10^{-6}$ watts. The corresponding antenna radiation efficiency was $\eta = 0.99011 \simeq 99\%$. Therefore, most of the input power is radiated except for a small portion which is reflected back into the antenna.

For pattern control purposes, sections of ECCOSORB GDS composite material, with measured electrical parameters $\epsilon_r = 14.9 - j0.25$ and $\mu_r = 1.55 - j1.45$ at 10 GHz, were placed on the inner E-plane walls of the horn as illustrated in Fig. 16. The nominal thickness of the composite material section was $t = 30$ mil (0.0762cm). The material thickness, however, was measured to be $t = 33$ mil (0.08382cm).

For the FDTD simulations a grid size of 0.1" was used. The material thickness was about a third of the FDTD cell. The composite material sections influence mainly the E-plane pattern. Thus, only results from the E-plane gain pattern calculation of the coated 20-dB standard gain horn are presented. Fig. 22 compares the FDTD computed results with measurements, when a 2" section of composite material was used. The agreement between the computed and measured results is good. As illustrated in the figure, the first side lobe of the pattern is eliminated. Because of the presence of the material in the inner walls, the broadside antenna gain was reduced

by 2.69 dB. In this case the antenna radiated power was estimated to be $P^{rad} = 0.0886980 \times 10^{-6}$ watts, resulting in an antenna efficiency of $\eta = 0.7631493 \simeq 76.3\%$. The reduced antenna efficiency in this case is due to the power dissipated in the 2" section of lossy magnetic material.

Fig. 23 compares the computed and measured E-plane patterns when a section of 4" GDS material is used for coating the E-plane walls of the 20-dB standard gain horn. As illustrated in the figure, good agreement between the computed and measured gain patterns is obtained in this case also. With 4" of GDS material the second side lobe in the pattern is almost eliminated. However in this case, the broadside gain is reduced by 4.98 dB. The radiation efficiency was reduced to $\eta = 0.63870 \simeq 63.9\%$. In this case a significant amount of power is dissipated in the lossy magnetic material.

Fig. 24 compares the FDTD computed gain pattern with measurements when a section of 66 mil thick and 2" long GDS material is used for coating the E-plane walls of the 20-dB standard gain pyramidal horn. In this case two sections of 33 mil GDS material were glued together to form a 66 mil section. As illustrated in the figure, good agreement between the computed and measured gain patterns is obtained in the main lobe. There are, however, some differences between the computed and measured results in the side lobes of the pattern. With the 66 mil section of GDS material the broadside gain of the pattern is reduced by 2.64 dB. The antenna radiation efficiency in this case was estimated to be $\eta = 0.70004 \simeq 70.0\%$.

The FDTD results of the broadside gain and efficiency calculations for the different antenna geometries are summarized in Table 1.

Table 1: Broadside gain and radiation efficiency of a 20-dB standard gain horn at 10 GHz, partially coated with composite material.

Antenna type	$G_E(\theta = 0^\circ, \phi = 90^\circ)$ dB	Efficiency, η
Conducting walls	20.65	0.99011
GDS material, $l_m = 2''$, $t = 33$ mil	17.96	0.76315
GDS material, $l_m = 4''$, $t = 33$ mil	15.67	0.63870
GDS material, $l_m = 2''$, $t = 66$ mil	18.01	0.70004

To examine the effect of material thickness and length on the antenna radiation pattern, the broadside gain loss of the 20-dB standard gain horn was

calculated for different GDS material thickness and lengths. The variation of the broadside antenna gain loss versus the GDS material thickness, for different material lengths, is illustrated in Fig. 25. As illustrated in the figure the broadside antenna gain loss is largest for thickness in the range of 25 - 30 mil, and decreases for larger material thickness. Thus thickness range is not strongly influenced by the material length.

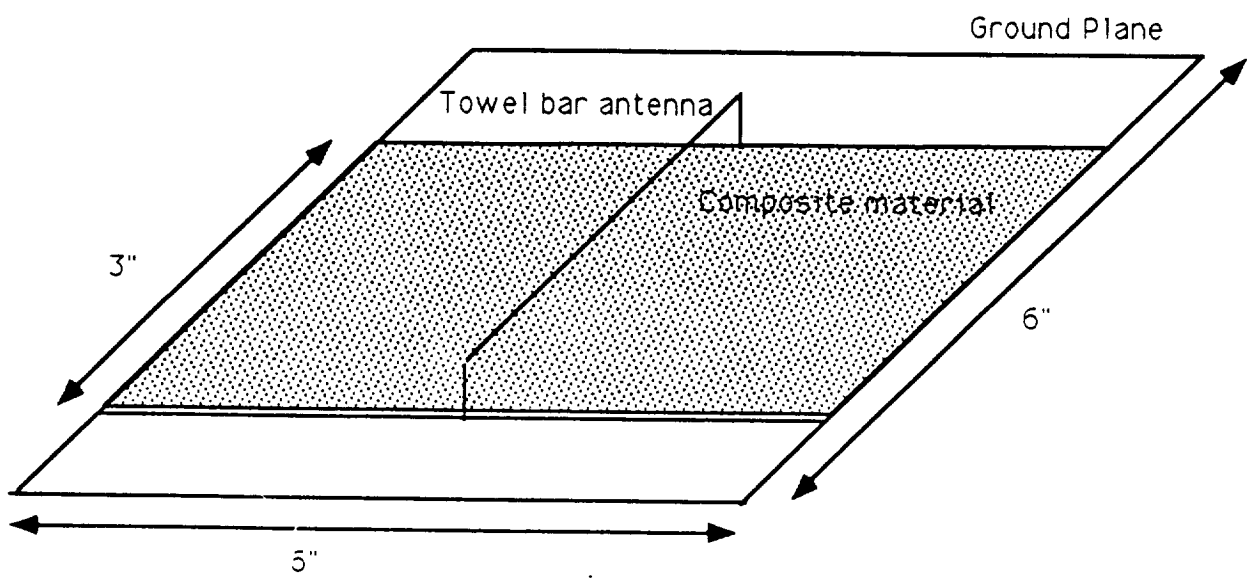


Figure 1: Geometry of a towel-bar antenna mounted on a composite material-coated plate

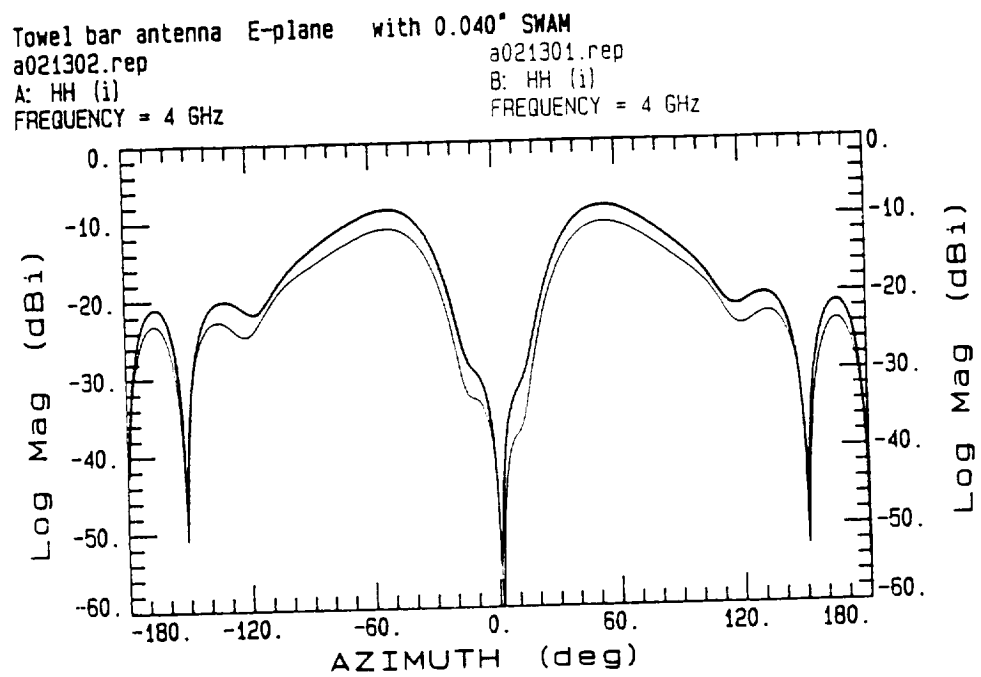


Figure 2: Measured yz-plane pattern of the towel bar antenna on composite materials at 4 GHz

Towel bar antenna with SWAM y-z plane
a032502.rep a032503.rep
A: HH (i) B: HH (i)
FREQUENCY = 5 GHz FREQUENCY = 5 GHz

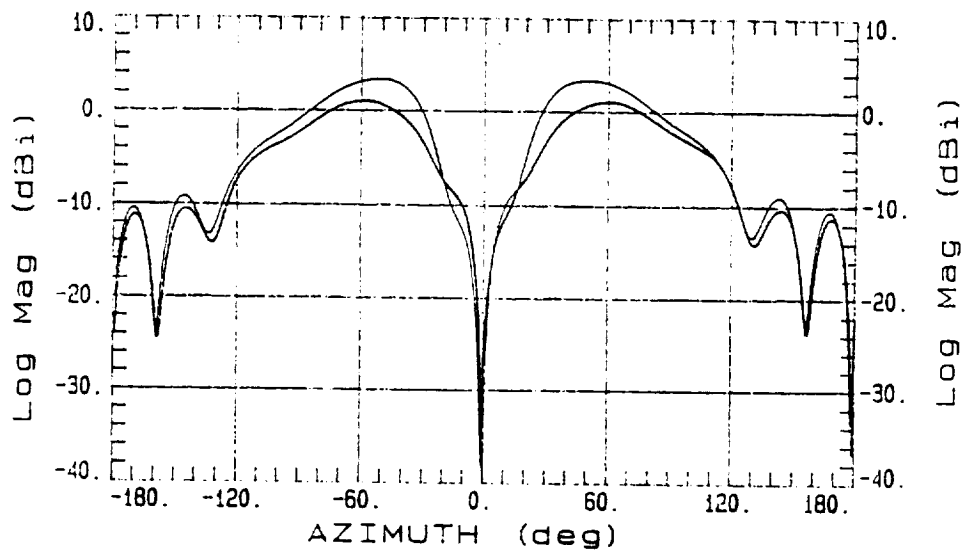


Figure 3: Measured yz-plane plane pattern of the towel bar antenna on composite materials at 5 GHz

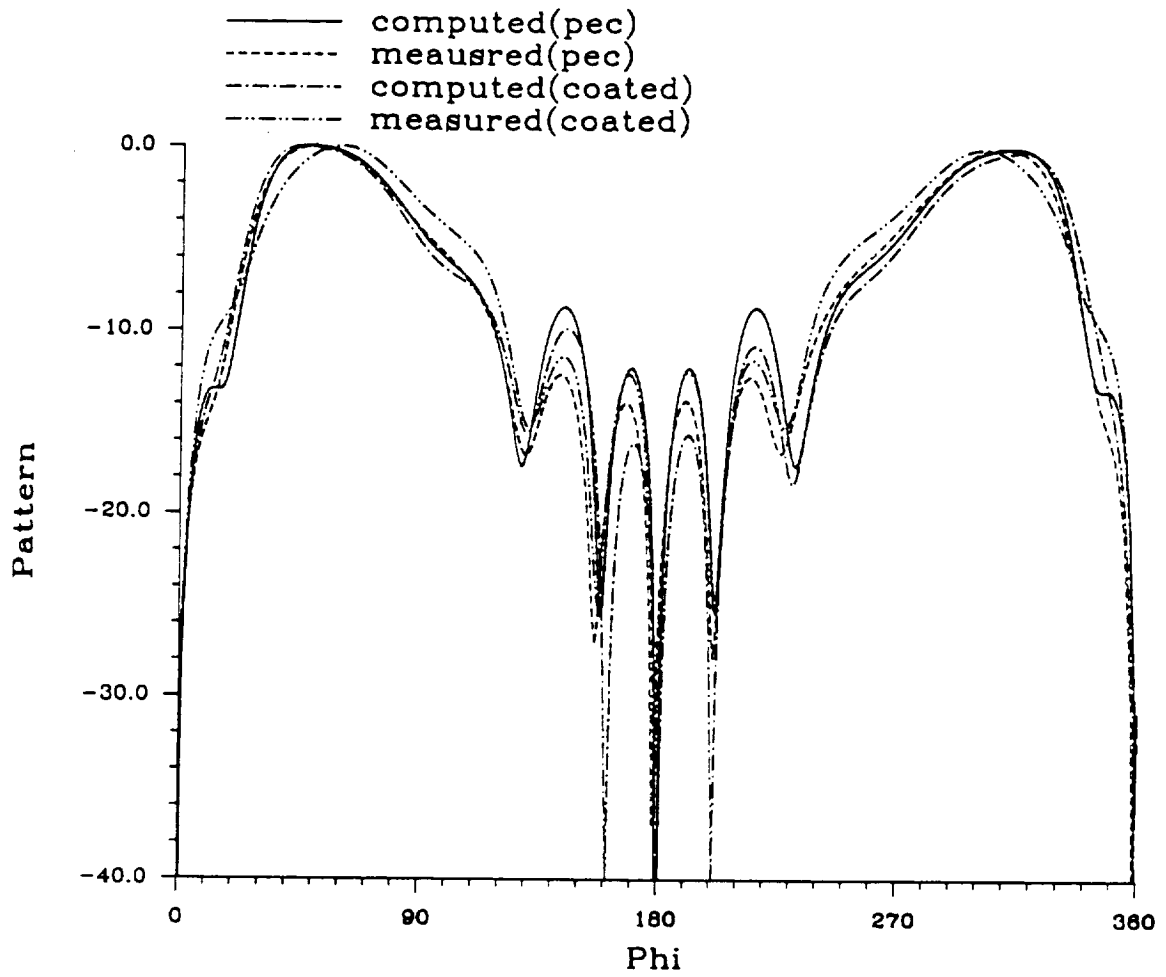


Figure 4: Predicted and measured radiation pattern of the towel-bar antenna in yz plane (the plane perpendicular to both the towel-bar plane and the ground plane).

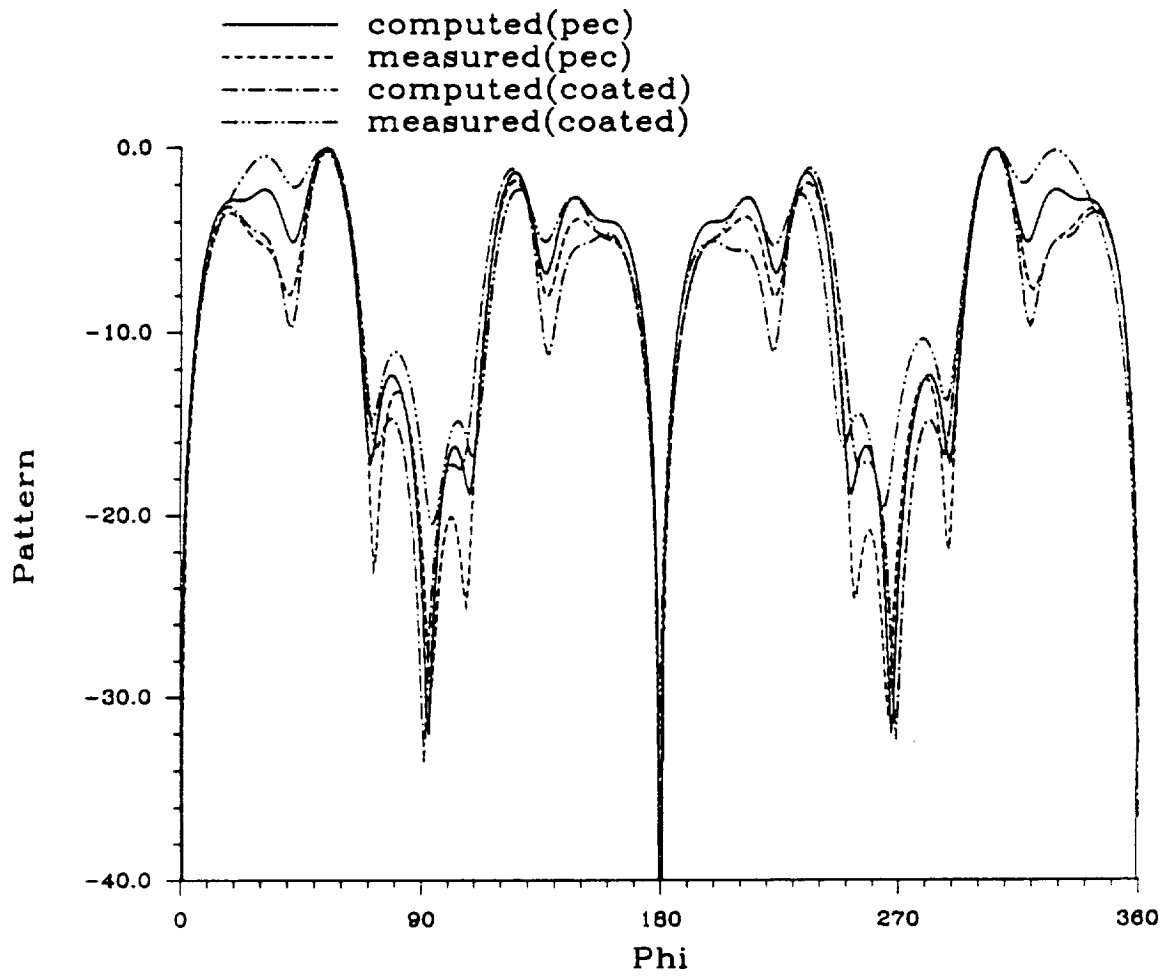


Figure 5: Predicted and measured radiation pattern of the towel-bar antenna in xy plane (the ground plane).

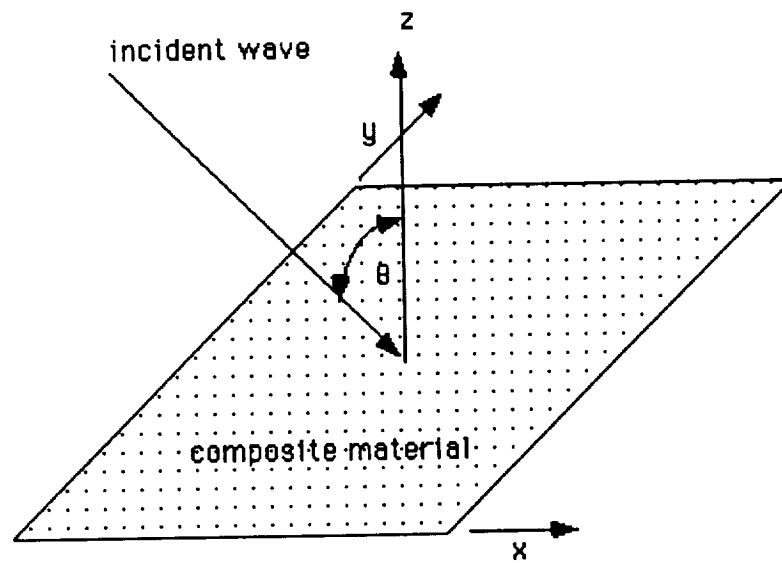


Figure 6: The geometry used to compute current distribution on a $\lambda/2 \times \lambda/2$ composite plate.

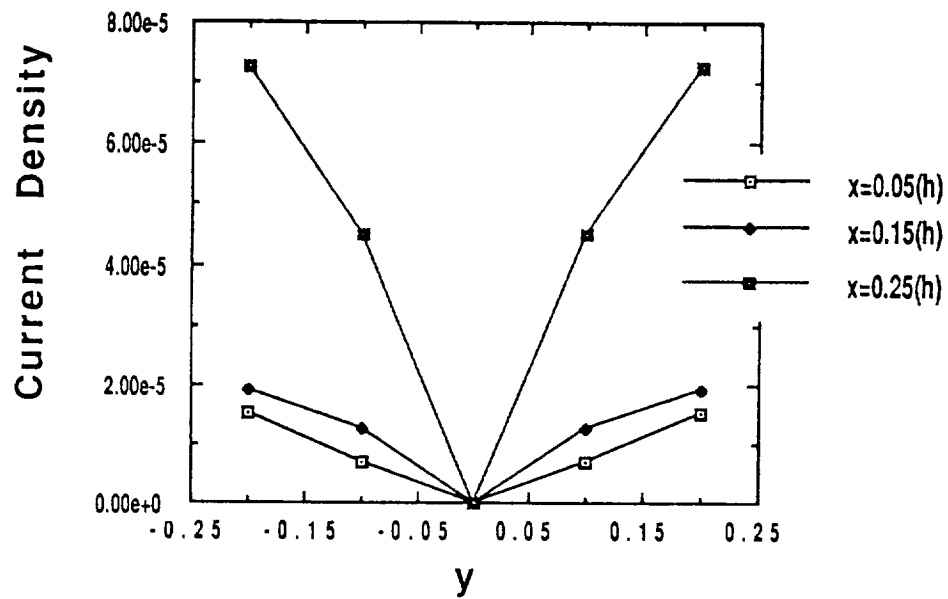


Figure 7: Current distribution along constant x lines. Hard polarization.

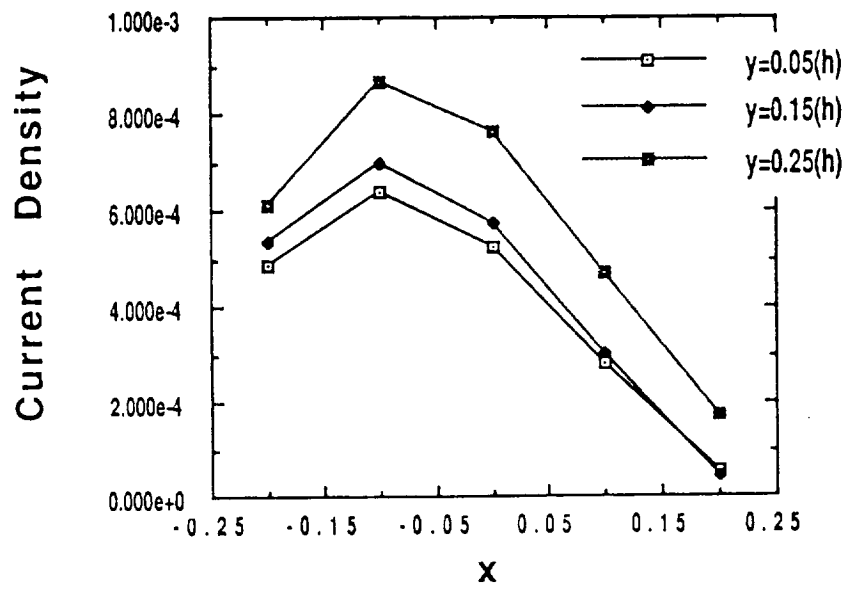


Figure 8: Current distribution along constant y lines. Hard polarization.

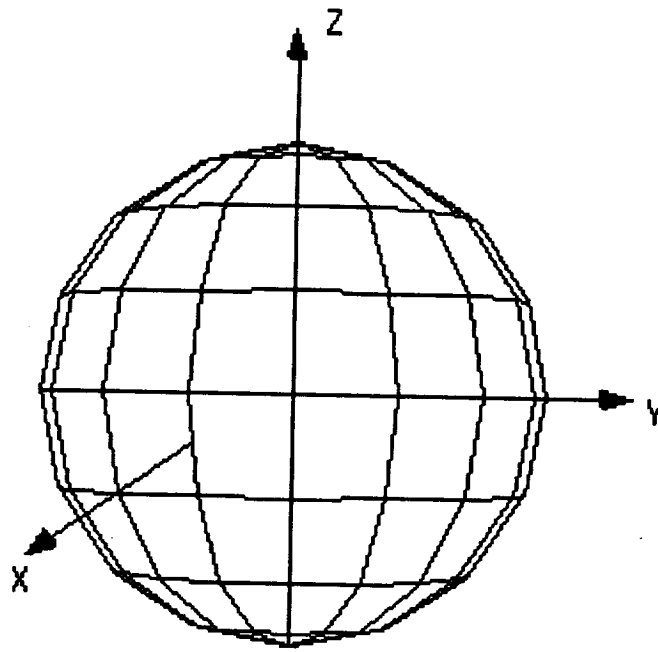


Figure 9: The geometry of a dielectric sphere with radius of 0.5λ .

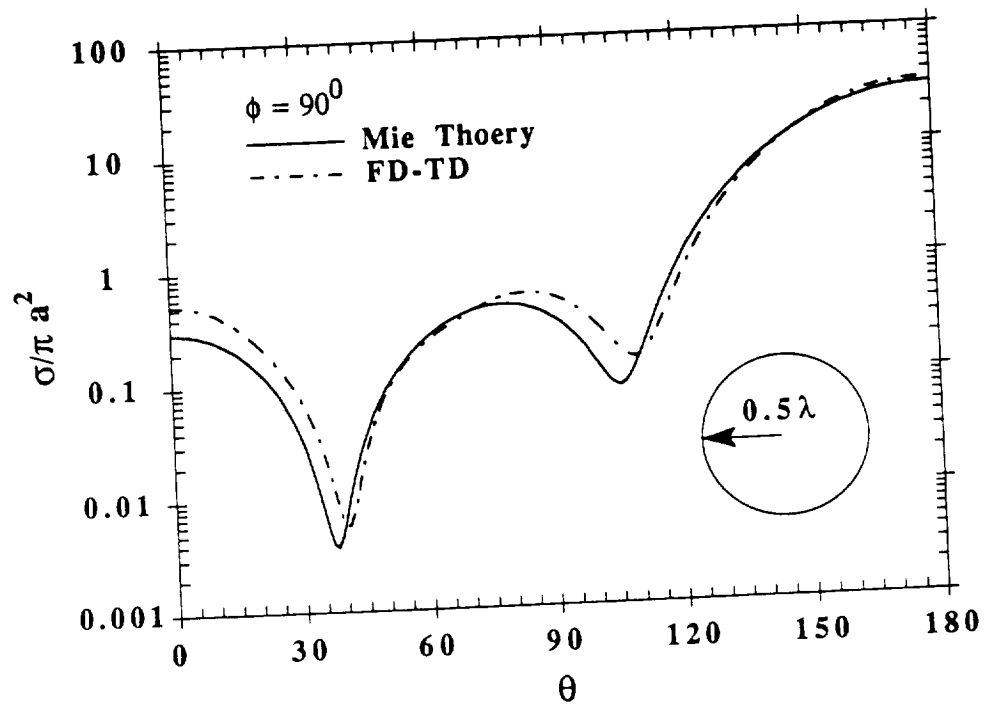


Figure 10: RCS of a dielectric sphere in the plane of $\phi = 90^{\circ}$. ($\epsilon_r = 2.0 - j0.06$)

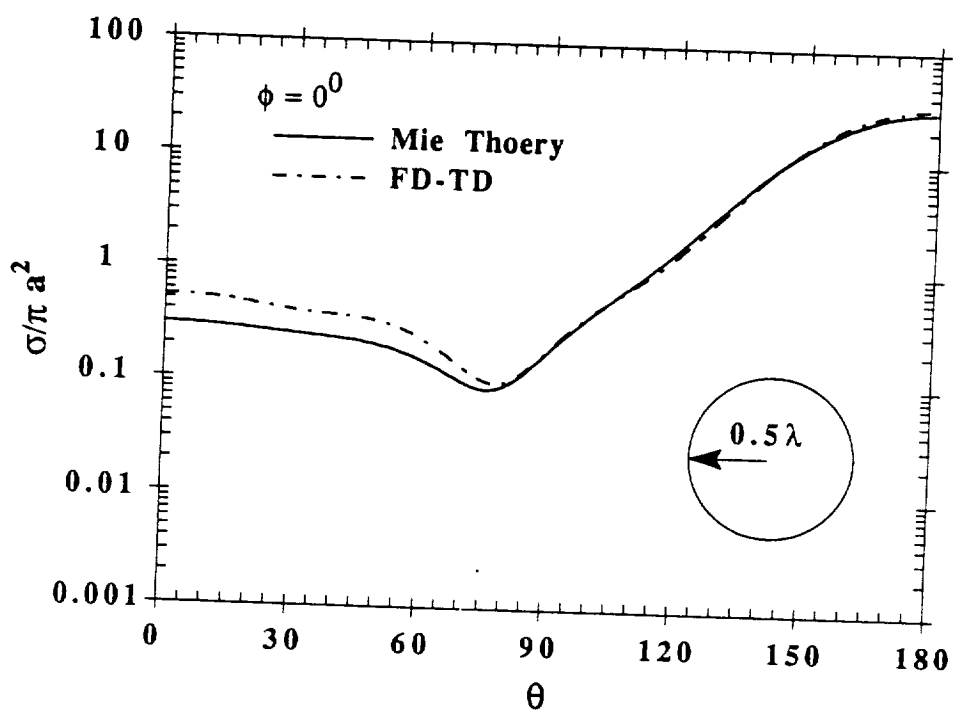


Figure 11: RCS of a dielectric sphere in the plane of $\phi = 0^\circ$. ($\epsilon_r = 2.0 - j0.06$)

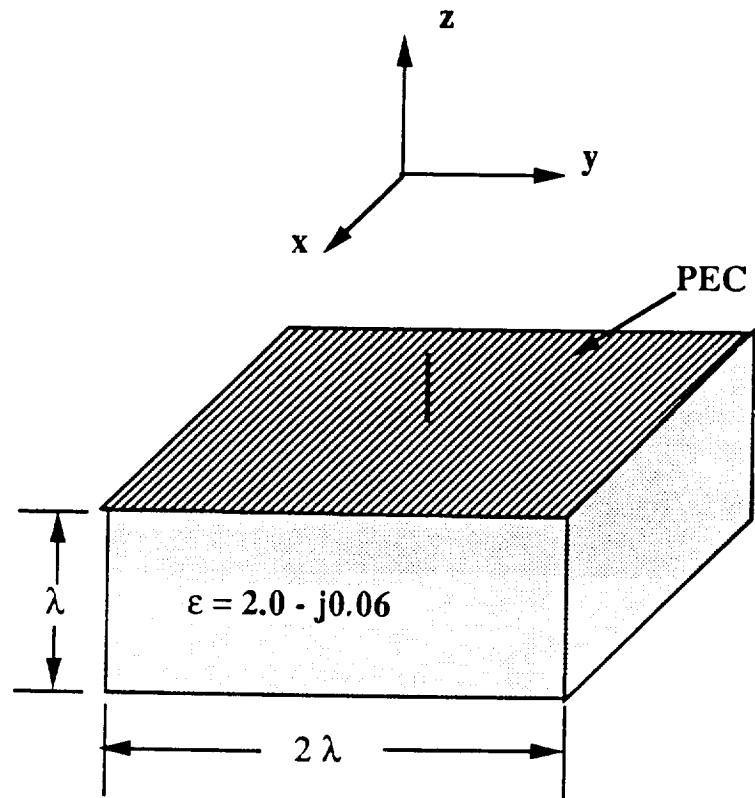


Figure 12: Geometry of a monopole grounded with PEC and dielectric substrate.

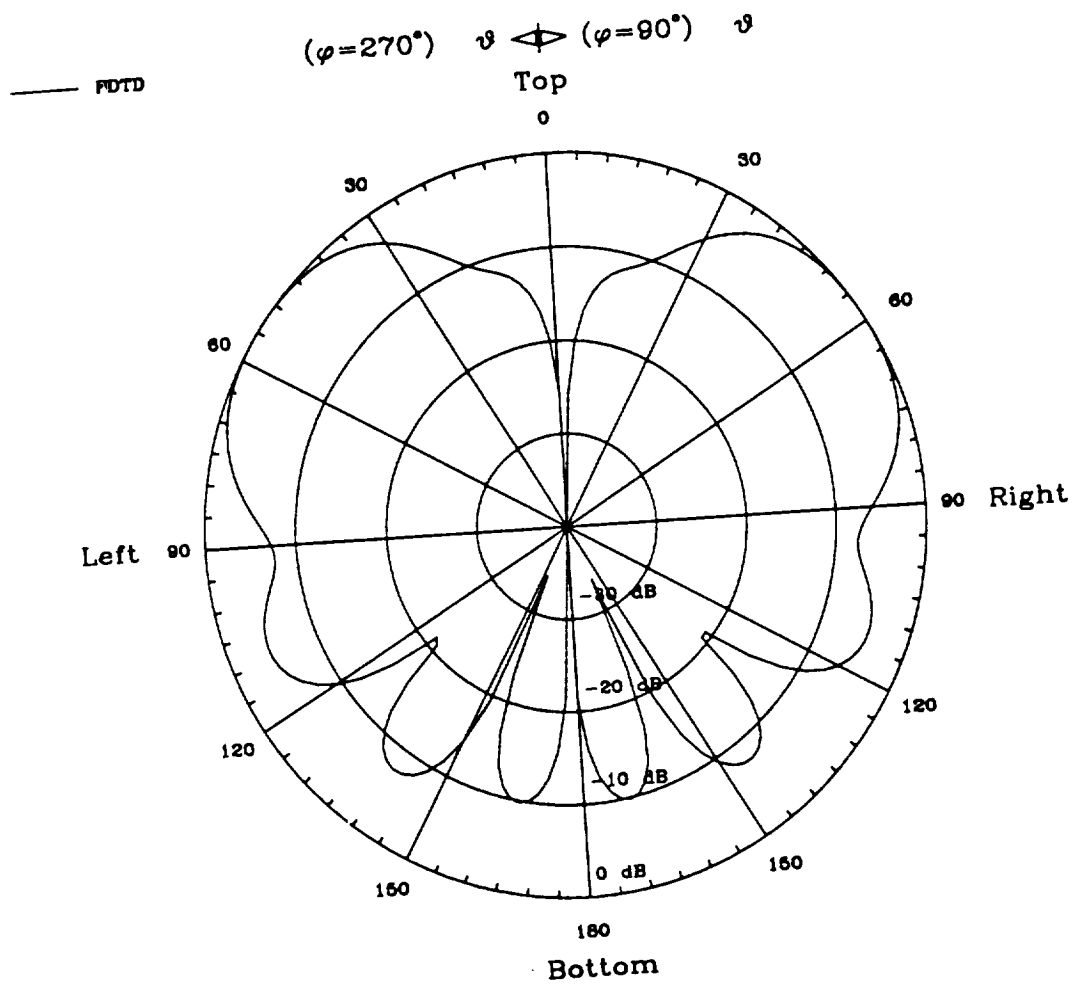


Figure 14: YZ-plane radiation pattern of a monopole grounded with PEC and dielectric substrate.

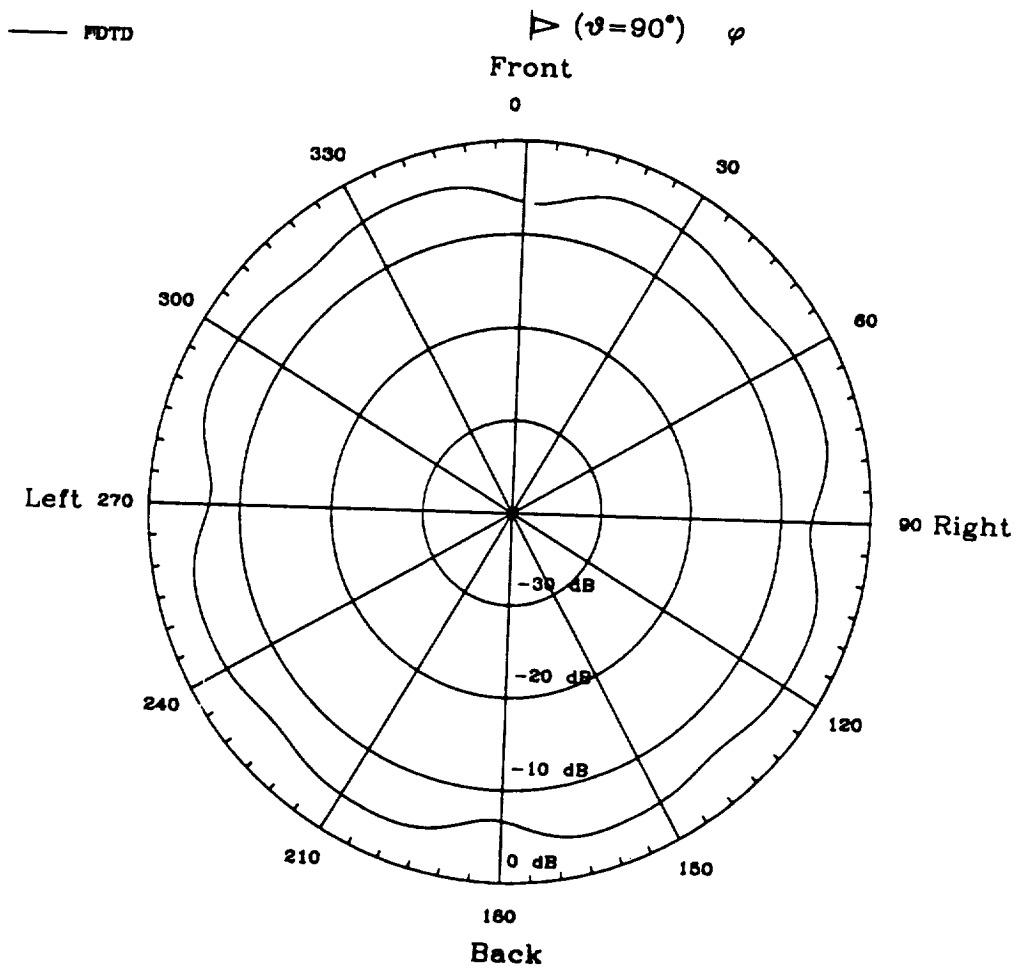


Figure 15: XY-plane radiation pattern of a monopole grounded with PEC and dielectric substrate.

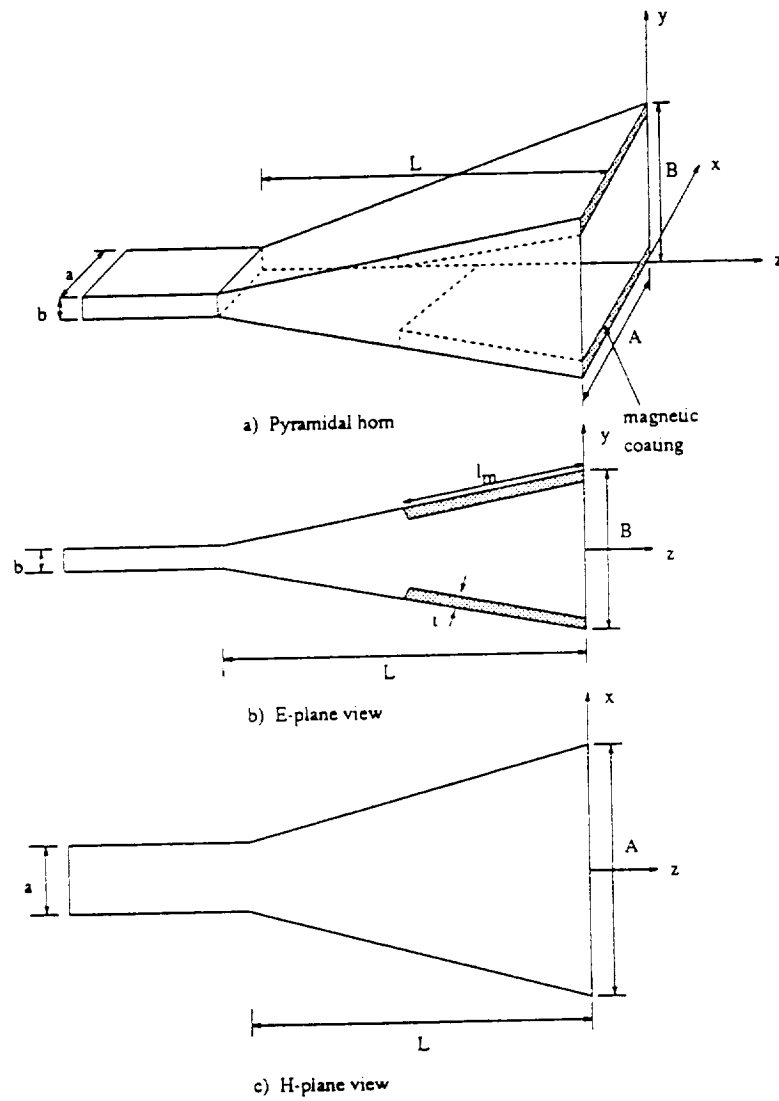


Figure 16: Geometry of a pyramidal horn antenna with composite E-plane walls.

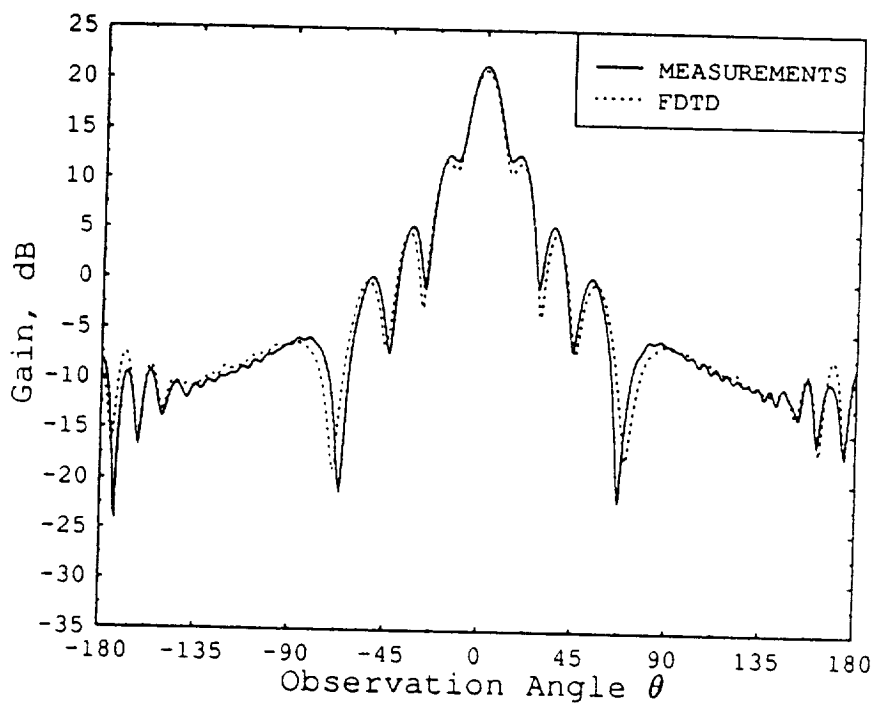


Figure 17: E-plane gain pattern of a square aperture pyramidal horn at 10.0 GHz. The antenna size was $A = 5''$, $B = 5''$, $L = 10.5''$, $a = 0.9''$ and $b = 0.4''$.

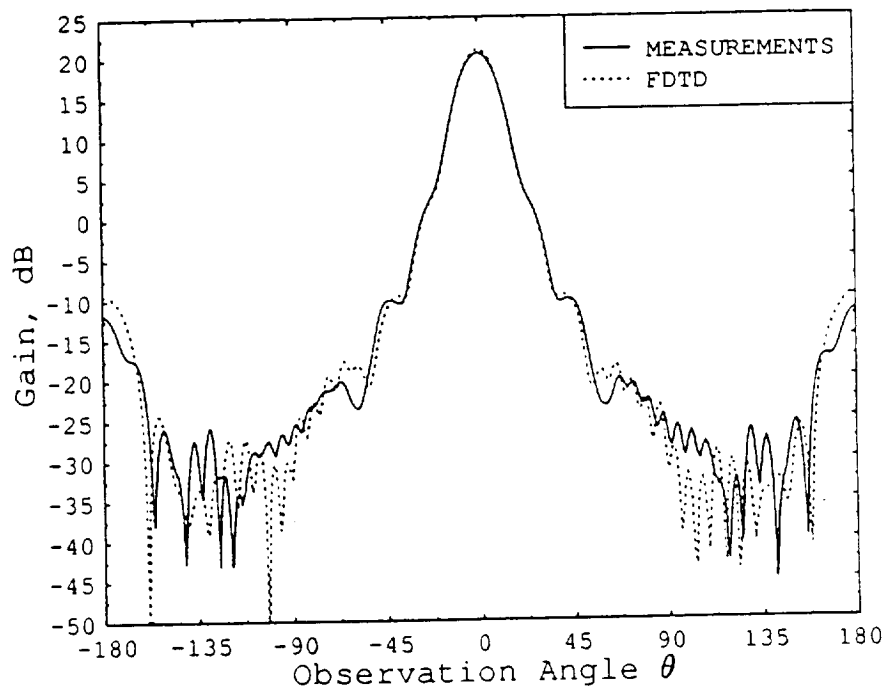


Figure 18: H-plane gain pattern of a square aperture pyramidal horn at 10.0 GHz. The antenna size was $A = 5''$, $B = 5''$, $L = 10.5''$, $a = 0.9''$ and $b = 0.4''$.

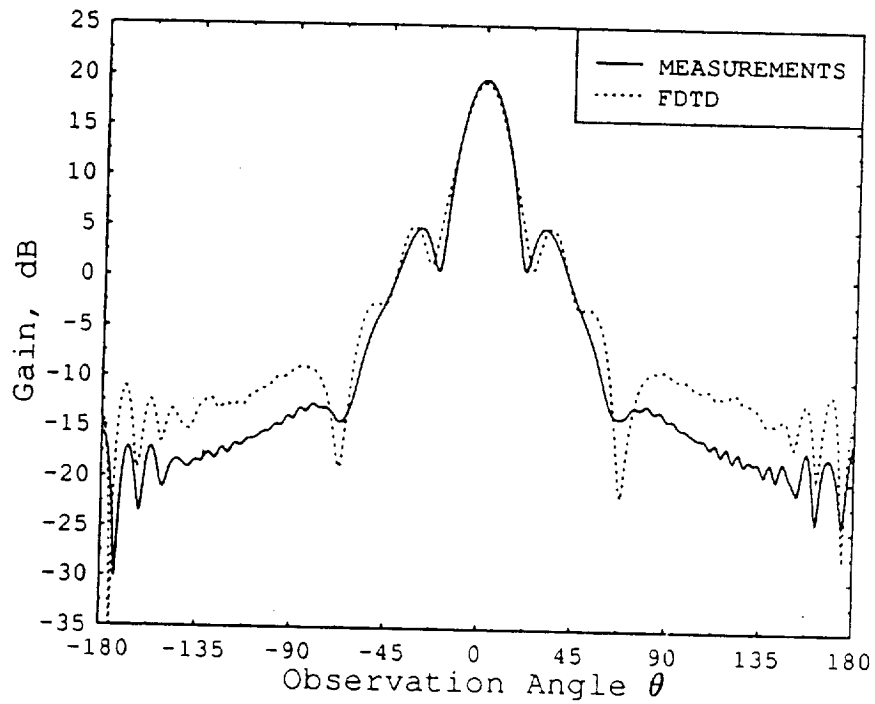


Figure 19: E-plane gain pattern of a square aperture pyramidal horn with composite E-plane walls at 10.0 GHz. The antenna size was $A = 5''$, $B = 5''$, $L = 10.5''$, $a = 0.9''$ and $b = 0.4''$. The parameters of the composite material were $l_m = 3''$, $t = 0.040''$, $\epsilon_r = 15.95 - j0.45$ and $\mu_r = 1.58 - j1.18$.

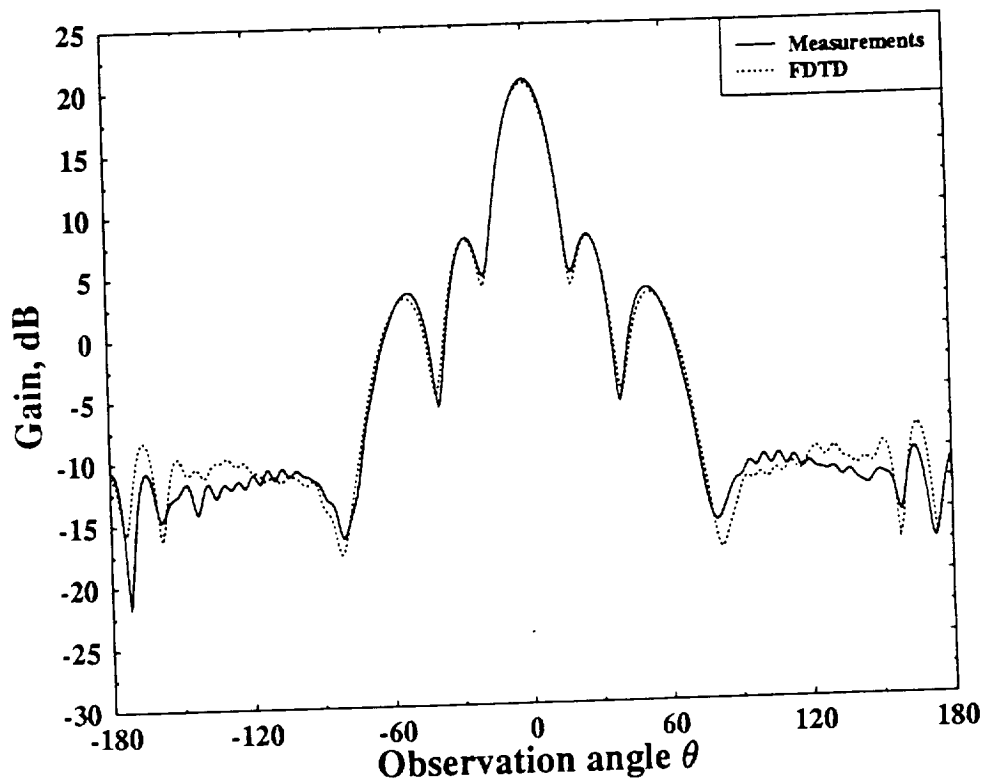


Figure 20: E-plane gain of a 20-dB standard gain pyramidal horn with conducting walls at 10.0 GHz ($A = 4.87''$, $B = 3.62''$, $L = 10.06''$, $a = 0.9''$ and $b = 0.4''$).

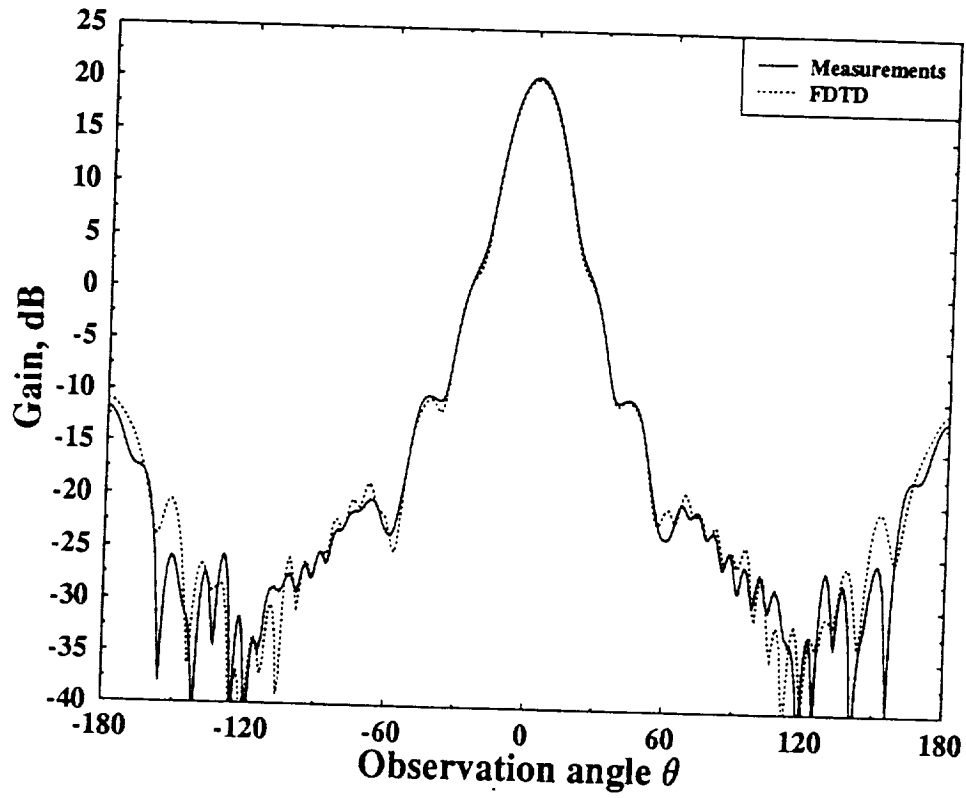


Figure 21: H-plane gain of a 20-dB pyramidal standard gain horn with conducting inner walls at 10.0 GHz.

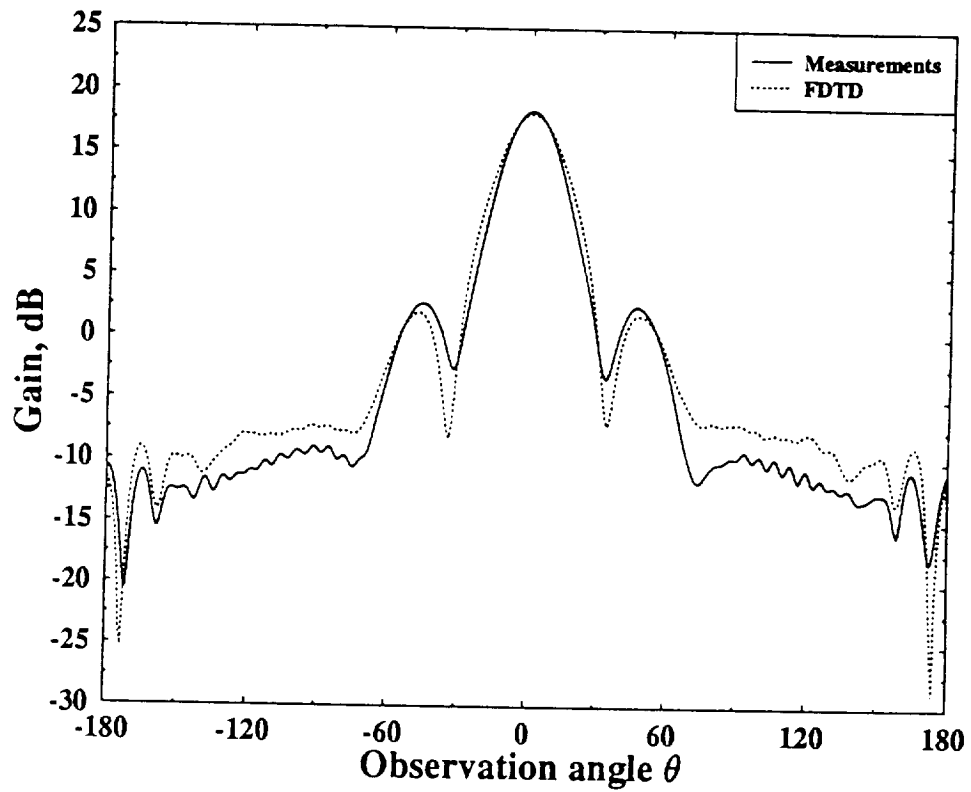


Figure 22: E-plane gain of a 20-dB standard gain pyramidal horn at 10.0 GHz, partially coated with GDS magnetic material ($\epsilon_r = 14.9 - j0.25$ and $\mu_r = 1.55 - j1.45$, $t = 33$ mil and $l_m = 2''$).

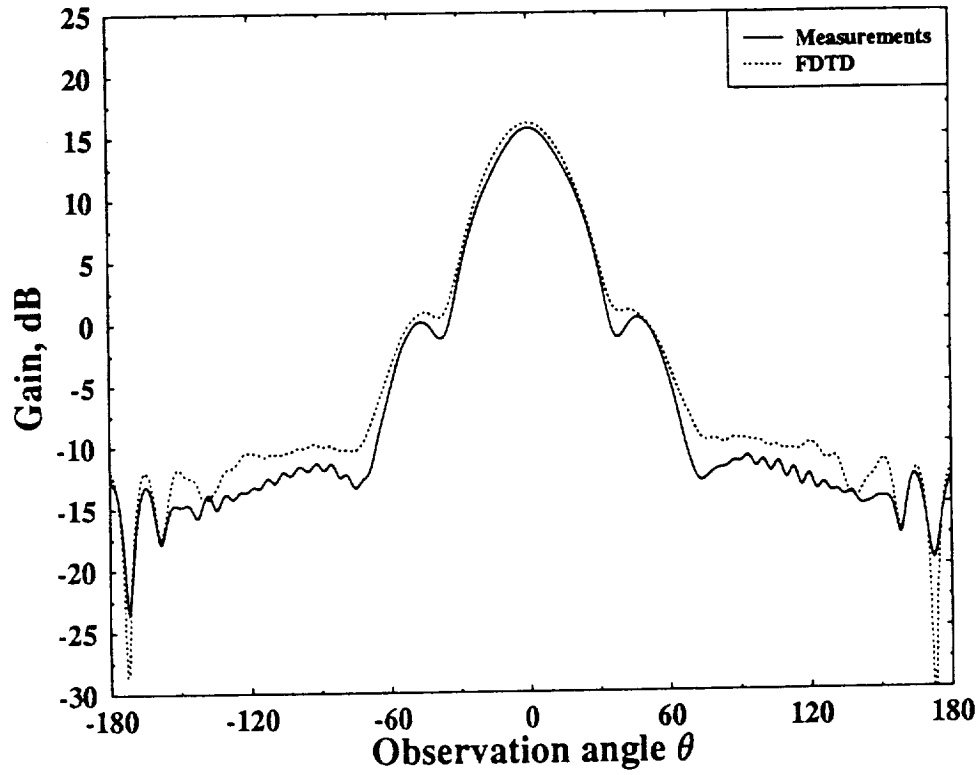


Figure 23: E-plane gain of a 20-dB standard gain pyramidal horn at 10.0 GHz, partially coated with GDS magnetic material ($\epsilon_r = 14.9 - j0.25$ and $\mu_r = 1.55 - j1.45$, $t = 33$ mil and $l_m = 4''$).

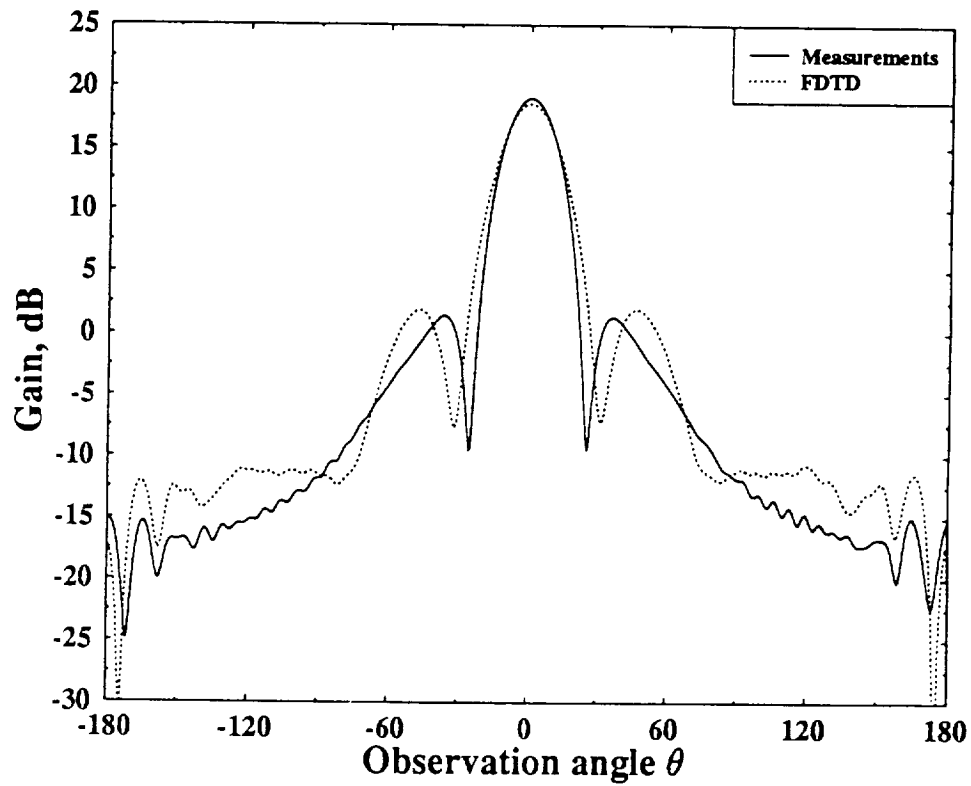


Figure 24: E-plane gain of a 20-dB standard gain pyramidal horn at 10.0 GHz, partially coated with GDS magnetic material ($\epsilon_r = 14.9 - j0.25$ and $\mu_r = 1.55 - j1.45$, $t = 66$ mil and $l_m = 2''$).

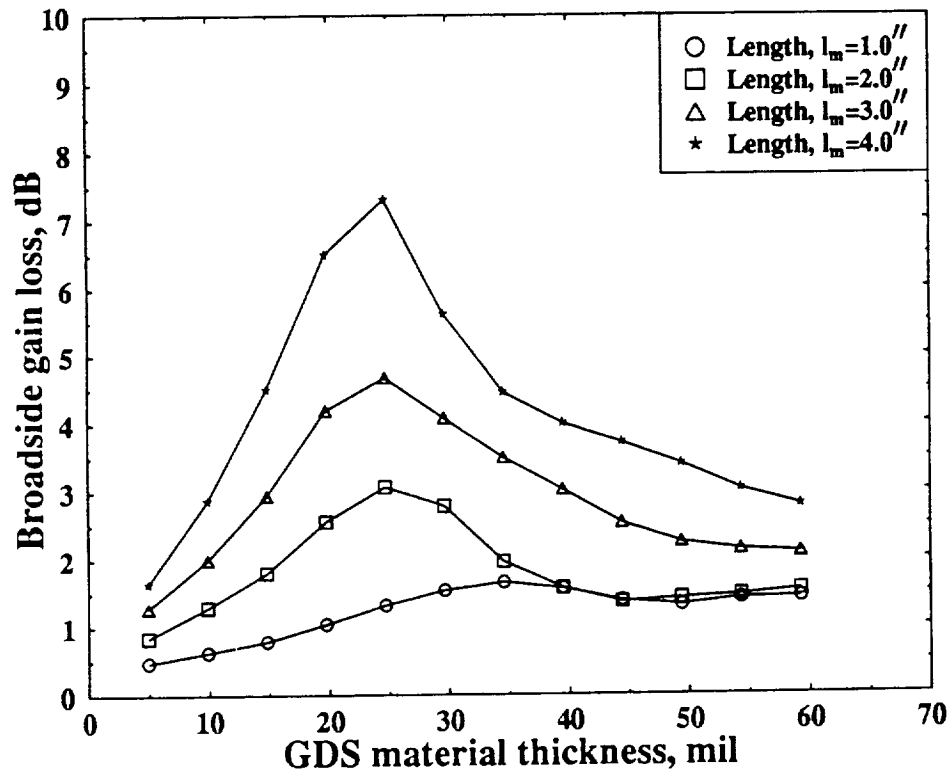


Figure 25: Broadside antenna gain loss of a 20-dB standard gain pyramidal horn at 10.0 GHz, partially coated with GDS magnetic material ($\epsilon_r = 14.9 - j0.25$ and $\mu_r = 1.55 - j1.45$).

III. ANTENNA TECHNOLOGY

A. Introduction

During this report period, special significant progress in the area of conformal cavity-backed antennas has been achieved.

In the previous report, the scattering and radiation performance of single elements of circular patches backed by circular and rectangular cavities were presented. Since then, we have succeeded in verifying some of the theoretical results by fabricating and testing a single circular patch antenna backed by a circular cavity. In addition, we have also developed numerical code for the analysis of the radiation characteristics of infinite arrays of probe-fed circular patches each backed by a circular or rectangular cavity.

During the previous periods, a two-dimensional analytical model of a magnetically-tunable CBS antenna characterized the effect of losses in the ferrite at VHF and UHF frequencies, and an experimental cavity was built that utilizes a more powerful DC magnetic bias field than in previous experiments. This period, the analytical model of a three dimensional CBS antenna has been initiated and its progress is reviewed. A discussion of a different cavity experiment is also included.

B. Cavity-Backed Microstrip Patch Antennas

One way to overcome the tradeoff that exists between bandwidth and scan volume in a microstrip patch element phased array is to surround each patch element with a cavity. By doing so, the substrate can no longer support guided wave modes. Therefore, the substrate thickness can be increased substantially to improve the bandwidth without a corresponding decrease in scan coverage.

In this report period, we have succeeded in verifying some of the theoretical results by fabricating and testing a single circular patch antenna backed by a circular cavity. Fig. 26 shows the cross section of this antenna. The parameters used for the experimental model are given by:

$R_1 = 4.55 \text{ cm}$	$R_2 = 5.72 \text{ cm}$	
$\epsilon_r = 2.2 (1 - j0.0009)$	$\mu_r = 1$	
$a = 4.55 \text{ cm}$	$c = 0.2286 \text{ cm}$	
$x_p = 1.18 \text{ cm}$	$y_p = 0$	$r_0 = 0.045 \text{ cm}$

The antenna was tested by measuring the S11 parameter, using an HP8510 network analyzer. Fig. 27 illustrates the experimental and theoretical input impedance results on a Smith chart. As can be seen, the results agree well. Fig. 28 shows the theoretical and experimental return loss. The slight variation in the resonant frequency between the theory and experiment is primarily due to the tolerance of the dielectric constant of the substrate, and the machining of the cavity.

In this report period, we have also developed numerical code for the analysis of the radiation characteristics of infinite arrays of probe-fed circular patches each backed by a circular or rectangular cavity. The geometry of an infinite array of circular patches backed by circular cavities is shown in Fig. 29.

Results of the computer codes for the two different antenna geometries are compared to those of an infinite array of conventional patches. The parameters of interest are the broadside-matched active reflection coefficient, and the active resistance of an array elements. The broadside-matched reflection coefficient is determined by matching the antenna elements at broadside ($\theta = 0, \phi = 0$), and calculating the antenna reflection coefficient as a function of scan angle (Fig. 30). This can be used to determine the scanning range of the array as a function of substrate thickness. Furthermore, by calculating the active resistance of the antenna as a function of frequency for varying substrate thickness, we can gain insight into the bandwidth performance of the antenna.

We can begin by first considering a thin substrate. The parameters for Case A for the circular cavity-backed array are given by:

$R_1 = 0.178 \lambda_0$	$R_2 = 0.222 \lambda_0$	
$\epsilon_r = 2.5$	$\mu_r = 1$	
$a = 0.27065 \lambda_0$	$c = 0.02 \lambda_0$	
$x_p = 0.089 \lambda_0$	$y_p = 0$	$r_0 = 0.004 \lambda_0$
$d_x = 0.5 \lambda_0$	$d_y = 0.5 \lambda_0$	

Fig. 31 illustrates the E-plane ($\phi=0$) broadside-matched active reflection coefficient of this antenna along with an equivalent array of circular patches backed by rectangular cavities and an array of conventional circular patches. The figure shows that for thin substrates the scan performance of conventional and cavity-backed patches are similar. However, there exists a peak in the reflection coefficient of the conventional array near grazing angle that does not appear in the cavity-backed patches. This peak corresponds to the excitation of leaky wave modes in the substrate of a conventional array that has been effectively eliminated in the cavity-backed patch geometries. Fig. 32 illustrates the H-plane ($\phi=90$) broadside-matched active reflection coefficient of the three antennas for Case A. This result is also similar for the three arrays.

Next, we increase the substrate thickness and look at the results for the three arrays. The parameters chosen for Case B are given by:

$R_1 = 0.164 \lambda_0$	$R_2 = 0.205 \lambda_0$	
$\epsilon_r = 2.5$	$\mu_r = 1$	
$a = 0.27065 \lambda_0$	$c = 0.05 \lambda_0$	
$x_p = 0.082 \lambda_0$	$y_p = 0$	$r_0 = 0.004 \lambda_0$
$d_x = 0.5 \lambda_0$	$d_y = 0.5 \lambda_0$	

Fig. 33 illustrates the E-plane reflection coefficient for Case B. The results indicate that the cavity-backed patch arrays show improvement in scan performance over the conventional patch array for the thicker substrate. Fig. 34 illustrates the H-plane reflection coefficient for Case B. The cavity-backed patch arrays also show enhanced performance in the H-plane, but not as dramatic as the E-plane. Furthermore, the leaky wave resonance in the conventional patch array has shifted closer to broadside that is an undesirable

effect of a thicker substrate. Finally, increasing the substrate thickness even more, we use parameters of Case C given by:

$R_1 = 0.156 \lambda_0$	$R_2 = 0.195 \lambda_0$	
$\epsilon_r = 2.5$	$\mu_r = 1$	
$a = 0.27065 \lambda_0$	$c = 0.08 \lambda_0$	
$x_p = 0.078 \lambda_0$	$y_p = 0$	$r_0 = 0.004 \lambda_0$
$d_x = 0.5 \lambda_0$	$d_y = 0.5 \lambda_0$	

Fig. 35 illustrates the E-plane reflection coefficient of the three arrays for Case C. The results show that the cavity-backed patch arrays demonstrate substantial improvement in their scan performance over the conventional patch array. Fig. 36 illustrates the H-plane reflection coefficient results. This also indicates that the cavity-backed patch arrays have an enhanced scan volume. Fig. 37 illustrates the E-plane reflection coefficient of the circular cavity-backed patch array as a function of substrate thickness. This clearly demonstrates the advantage of using a thicker substrate in obtaining better scan performance. In addition to scan volume enhancement, the cavity-backed patches also exhibit improvement in bandwidth. Fig. 38 illustrates the active resistance of the circular cavity-backed patch array as a function of substrate thickness. As can be seen, as the substrate thickness is increased the bandwidth of the array also increases.

The overall results of the cavity-backed patch arrays indicate that by increasing the substrate thickness, both scan volume and bandwidth performance of the array can be improved. Furthermore, surface and leaky wave resonances excited in the substrate of conventional microstrip patch phased arrays are completely eliminated in the cavity-backed patch arrays. Thus, the cavity-backed patch arrays show substantial improvement over the conventional patch arrays.

The analysis and design of cavity-backed microstrip and stacked microstrip antenna will continue. In addition, we are very interested in developing computer codes for these structures that can be implemented on a massively parallel processor (MPP) such as ASU's MASPARG machine. Because MPPs are poised to become the high-performance computing architecture of choice, their impact must be considered in antenna technology.

C. Ferrite-Controlled Cavity-Backed Slot Radiators

The cavity backed slot (CBS) antenna is also a lightweight, conformal radiator, and considered efficient due to its electrical size and material loading within the cavity. Having these characteristics, the cavity backed slot is an ideal choice for experimentation as a tuneable antenna. As stated in previous reports, the concept of using a ferrite to magnetically tune a CBS antenna is not new [6]. The literature, however, lacks any substantial work to verify the capability of such an antenna [6], [7] and [8].

Previously, a two-dimensional analytical model of a magnetically tuneable CBS antenna characterized the effect of losses in the ferrite at VHF and UHF frequencies. Also, an experimental cavity was built and the experiments showed a small magnetostatic volume wave mode resonance at 333 MHz. For completeness in this report, a short review of ferrite materials with emphasis to the present problem will be addressed first. Then the progress of the analytical model of the three-dimensional CBS antenna will be reviewed. A discussion of a different cavity experiments will follow. This new cavity configuration attempts to eliminate some of the shortcomings of the previous experimental work. Also power pattern of one CBS antenna configuration will be shown. Lastly, the conclusion to this section will outline the plans for future work.

1. Background

Ferrite substrates are ferromagnetic, or superparamagnetic, materials constructed from solid ceramic materials which have been sintered with certain metal oxides at high temperatures. At microwave frequencies they exhibit strong magnetic effects, which result in anisotropic behavior. By applying an external DC magnetic field, the permeability tensor of the ferrite is altered. This change occurs due to the interaction of the internal magnetic moment of the ferrite and the magnetic field of the material. The interaction effectively alters the electrical characteristics of the material used in the CBS structure. Consequently, the antenna will resonate at a different frequency for different values of the applied DC magnetic field.

There are two types of modes that can be excited inside the cavity. The first modes considered are the dynamic modes, which strongly depend on the the size of the cavity and the electrical properties of the materials inside the

cavity. This mode is somewhat independent of the magnetic bias of the ferrite as shown in previous reports. This has been the traditional type of modes excited within the CBS antenna. The second type of modes considered is the magnetostatic mode. These modes also depend on the external magnetic bias field. For these modes, the biased ferrite material gives rise to low frequency magnetostatic volume wave modes which become appreciable with large external bias fields. The volume wave modes travel in the direction of the bias field. Magnetostatic surface wave modes can also exist. Their cutoff frequency is higher than a volume wave mode and these modes travel perpendicular to the direction of the bias field. It is these volume wave modes that will allow the a microwave CBS antenna to operate in a frequency range lower than those of the dynamic modes.

2. Theoretical Analysis

The purpose of this section is to document the progress on the rigorous modeling of the CBS antenna filled with dielectric and ferrite layers. Before discussing the progress of the code development, the differences between the previous and the present analysis will be discussed as well as the methodology of the present analysis.

Previous work on this effort concentrated on the two-dimensional analysis of a CBS antenna filled with ferrite as shown in Figure 39. Note that both the slot and the cavity are assumed infinite in the x direction. General trends and a 'feel' for the design parameters could be extracted from the results. However, the true geometry being built has three dimensions as shown in Figure 40. The physical cavity is not infinite the x dimension; it has a finite length (x), width (y) and depth (z). This three dimensional analysis will provide direct information on tuning capabilities, radar cross section predictions, material losses, and other important parameters. Unfortunately, by adding the extra dimension to model the antenna, the theoretical and numerical analysis becomes much more intensive than the two-dimensional model. However, the method of the three-dimensional analysis is similar to that of the two-dimensional cavity.

Both approaches employ the method of moments [10, 11] and derive their respective Green's functions utilizing the spectral domain approach (SDA). Both use magnetic current basis functions to describe the fields in the slot region. However, this added dimension is not without a price. The three-

dimensional analysis adds an extra degree of complexity since it is a function of two variables while the two-dimensional analysis is only a function of one variable. The basis functions become two-dimensional and need a more complicated representation. This "extra" variable also yields a second integration and summation in the calculation of the admittance matrix which is pivotal for the moment method analysis. These added complications will take much more computation time. Some of the analytical points will now be discussed.

The modes chosen to expand the fields in the slot are the waveguide modes of a rectangular slot. These modes were chosen since they fit the geometry and are somewhat compact in describing the slot fields. The Green's function used is the same as derived by El-Sharawy [12] and utilized in the two-dimensional analysis; but as mentioned before, both the variation in x and y will now be considered.

The methodology taken to solve the present problem is the network formulation [9]. This formulation is commonly used since the resulting code is modular and the analysis is systematic.

The model considered is assumed composed of multiple connected regions having their own real or mathematical boundaries. This concept of regions is quite useful for breaking up a complex problem into smaller, more manageable ones. Each region has its own physical and electrical characteristics expressed by a boundary value problem. The connection between regions is made by enforcing the electromagnetic boundary conditions at the interface between the regions.

For the problem at hand, the exterior region is assumed as an infinite half space bounded by a perfectly conducting plane. The interior region is a rectangular cavity filled with homogeneous layers of dielectric and ferrite material. The slot which connects the two regions is represented by a magnetic current density; i.e., an electric field since $\vec{M} = \vec{E} \times \hat{n}$ (\hat{n} is a unit vector normal to the plane of the slot). The basis set or modes chosen to represent the fields of the rectangular slot are the rectangular waveguide modes. The modes assumed in the slot can be thought of as ports in the network formulation. A port has the associated electrical properties of voltage and current. These quantities are analogous to the tangential electric and magnetic fields in the slot. In general, there may be more than one port associated with a given slot. This implies that there is more than one mode (basis function) representing the field distribution in the slot and is true for this analysis.

The admittance matrix for any region relates the voltage at one port to

a contribution of current at all ports of that region. The admittance matrix contains the electrical characteristics of that region. The admittance matrix is obtained by solving a boundary value problem as mentioned previously. Again, the admittance matrix is solved by a Galerkin moment method in the spectral domain [10, 12]. The Green's function enforces that the tangential magnetic field is continuous and its physical equivalence enforces that the tangential electric field is continuous in the slot. The calculation of the matrix is extremely difficult in this case due to the formulation of the Green's function, including the ferrite, and that the problem is three-dimensional. For our problem, we need only calculate two admittance matrices, one for the interior and one for the exterior region. This system of simultaneous equations can be written as:

$$[\mathbf{Y}_{\text{ext}} + \mathbf{Y}_{\text{int}}]\mathbf{V} = \mathbf{I} \quad (11)$$

where \mathbf{Y}_{ext} and \mathbf{Y}_{int} are the exterior and interior regions admittance matrices, \mathbf{V} and \mathbf{I} are vectors to describe the unknown voltages and the known excitation currents at the ports.

Presently, only the exterior region has a source, which is a plane wave impinging on the slot. This source will be used as the excitation for the calculation of the RCS of the CBS antenna.

Once the total admittance matrix and excitation vector is calculated, the unknown magnetic currents may be calculated by

$$[\mathbf{Y}_{\text{ext}} + \mathbf{Y}_{\text{int}}]^{-1}\mathbf{I} = \mathbf{V} \quad (12)$$

and the scattered field and RCS then can be determined.

To this date, the exterior admittance matrix, which is a twofold infinite integration, and the exterior excitation has been properly calculated. The radar cross section of a rectangular slot in an infinite ground screen has been calculated correctly as well.

In the interior region, the admittance matrix, which is a double infinite summation, has been properly computed for a dielectric loaded cavity. The combination of ferrite and dielectric loaded cavity still needs to be more carefully examined. The code is still in its testing stage and needs more time for debugging before it can be considered accurate under most conditions. During the next quarter, the dielectric/ferrite filled cavity will be brought under scrutiny and the theory necessary for the analysis of the strip feed will begin.

3. Cavity Backed Slot Experiments 1

Before describing the experiments performed this period, there should be a reminder about the goals to be achieved in this portion of the project and a discussion about the differences between this experiment and the experiment from the last quarter. The project goals of this CBS antenna filled with ferrite are twofold:

- a. To verify the ability to excite a magnetostatic volume wave mode in the ferrite of the CBS antenna at UHF and VHF, which is much lower than the dominant mode.
- b. To design and to predict the response of an efficient CBS antenna at both the UHF/VHF frequency by exciting the magnetostatic volume wave mode of the cavity.

Last time, the magnetization using one permanent magnet was insufficient to bias the design. In the present sets of experiments, two permanent magnets were used to bias the ferrite material. Another set of problems reported last quarter were in regard to the ferrite material.

Both the thickness and loss of the material were not favorable for the experiment. The ferrite material was too thin. The thickness of the ferrite material allows only a portion of the DC magnetic lines to pass through the ferrite material. The thicker the layer, the stronger the ferrite material is biased. Also increasing the surface area of the cavity and ferrite material will increase the magnetostatic volume wave mode since the mode is a function of the ferrite material's volume. Another drawback of previous experiments was the ferrite material was lossy. Loss will tend to dampen the resonance. Lower loss and thicker material was utilized in this experiment.

This experiment was to measure the effect of biasing the ferrite with the new cavity, ferrites and two permanent magnets. Figure 41 gives a top and side view of the cavity-backed structure with multiple layers of ferrite and dielectric materials. The frequency band of interest for this experiment was 0.045 to 2.0 GHz. All measurements were performed using an Hewlett Packard-8510B network analyzer.

The first measurement characterized the microstrip line with the slot electrically closed (short circuit). This isolated the microstrip line from the cavity and helped to determine how the connectors and line performed over

the frequency band. Figure 42 shows the return loss of the microstrip line with the slot shorted. The return loss is better than -24 dB over the frequency band of interest. The ripple in the measurement is a function of electrical length of the line and the standing wave seen on the line. This gave a reference point for the match to all future measurements.

The second measurement examined the slot with the cavity unbiased. Since, the measurement was only up to 2.0 GHz, the dynamic mode was not expected to be seen. The cavity is expected to resonant above 2 GHz. Figure 43 shows the return loss versus frequency for this configuration. As expected the return loss is worse at the higher frequencies due to the loading of the line with the CBS configuration. At low frequencies, the match improves since the slot is now electrically small, therefore no power can enter the cavity and coupling between the slot and the microstrip line decreases.

Although not shown in this figure, the resonance of the unbiased cavity's dominant mode was found to be 2.975 GHz. This frequency was found by measurement on the HP-8510B Network Analyzer.

The third measurement examined is the same configuration as above with the ferrite biased by two strong permanent magnets. In this case, the magnetostatic mode should appear at low frequencies. Figure 44 shows the return loss versus frequency for this biased configuration. By comparing Figures 43 and 44, a deep null (-39.6 dB) in the return loss can be seen at 1.87 GHz. This effect is due to the DC magnetic field biasing the cavity yielding an excitation of a magnetostatic wave mode. Presently, we have no way to tune the cavity by varying the applied DC applied magnetic field, except by removing one of the two permanent magnets.

For the sake of brevity, by varying the cavity configuration by either moving or removing one ferrite layer and decreasing the applied DC bias field (removing a magnet), the magnetostatic wave mode was no longer excited. This suggests that for this magnetization and cavity configuration there is some minimum acceptable volume range and magnetization level to excite the magnetostatic wave mode. Note: For this experiment more than half the cavity was filled with ferrite.

4. Antenna Measurements

Since a null was seen at 1.87 GHz in the return loss, it was obvious that there was a strong coupling from the microstrip line to the slot. By examining the

insertion loss of the structure (Figure 45) at the frequency, the transmission coefficient is approximately 0 dB. This suggests all power excited at port 1 travelled to port 2. There was no radiation. By examining Figures 44 and 45 more closely, one may notice that the return and insertion loss do not add to 0 dB at about 1.75 GHz. This discrepancy can be attributed to radiation of the slot/microstrip configuration. For this reason, it was decided to measure the power pattern of the fixture. A true gain measurement could not be performed since there was no standard gain horn in the range of interest for comparison.

Figure 46 shows the vertical polarization of the slot at 1.748 GHz. The pattern is relatively symmetric and fairly constant. The peak occurs just off broadside of the antenna. The pattern seen is a combination of the dominant mode of the slot and the microstrip line. That is why the power pattern does not decay as the radiation is measured towards grazing. The same is true for the horizontal polarization as shown in Figure 47; however, the pattern is skewed appreciably off center. This is due to the asymmetry of the ground plane for the horizontal polarization. A larger ground plane should be used when measuring the power pattern to remove the asymmetry in the pattern.

Figures 48 and 49 show a waterfall plot of the power pattern vs. frequency for both the vertical and horizontal polarization. A second resonance can be seen in the power pattern at approximately 800 MHz. This is another magnetostatic wave mode excited within the ferrite. This mode was unseen when the scattering parameters of the fixture were measured. It is reasonable to assume that this mode is not excited by the dominant microstrip mode of the fixture. This volume wave mode was excited due to the plane wave impinging on the structure. This second excitation is asymmetric and its field lines run perpendicular as compared to the first excitation.

5. Cavity Backed Slot Experiments 2

To review, a cavity backed slot antenna was built employing low loss ferrite and dielectric layers and a two permanent magnet bias system. The slot was fed from a microstrip line centered in the slot which was centered in the cavity as shown in Figure 50. The scattering parameters were measured with an HP-8510 network analyzer and showed a magnetostatic wave resonance at 1.87 GHz. The power pattern of the CBS antenna was measured and agreed with s-parameter measurements by showing a peak in the gain

about 1.75 GHz. It is expected that at 1.87 GHz, the slot/microstrip configuration is tightly coupled and no radiation should occur. Slightly off that frequency is where the radiation happens since the feed match is still good, but the slot/microstrip coupling is now weaker. A second peak in the gain was seen at 800 MHz. This is a second lower frequency peak, and it is also a magnetostatic wave resonance. Unfortunately, it was only excited during the radiation measurements. This led to the belief that a different, perhaps, odd excitation of the slot was necessary to have this mode appear in the S-parameter measurement. This second peak is near the frequency range desired. Because of this possibility of an odd excitation, the experiments were focused on varying the slot/microstrip feed to better understand the mechanism for resonance and to excite the lower frequency magnetostatic wave mode.

Three new feed configurations were examined to try understand how the magnetostatic mode is excited. These slot/microstrip/cavity configurations are shown in Figure 51. The old configuration will be referred to as the straight parallel microstrip line, since the line is straight and is parallel to the long dimension of the cavity. Similarly the three new configurations will be referred to as the straight perpendicular, bent parallel and bent perpendicular microstrip line. The idea of utilizing the microstrip line bent around slot is that the magnetic field does not change sign across the length of the slot. This can be shown by using the right-hand rule about the microstrip line.

Also, the cavity was loaded with dielectric in lieu of the ferrite to determine what effect the 'unmagnetized' ferrite would have in the cavity. Remember, once the ferrite has been exposed to a DC magnetic bias and the bias is removed, the ferrite is in a latched state and still has some alignment of its magnetic moments. Its internal magnetic moments are no longer completely random. Note that all measurements were taken with an HP-8510 network analyzer over a frequency range of 50 MHz to 2 GHz.

The first set of measurements shown are the four configurations with the cavity loaded with dielectric in lieu of the ferrite. Both S_{11} and S_{21} are shown for the straight and bent microstrip cases in Figure 52 and 53, respectively. For the straight microstrip line, the match improves as the frequency decreases. This happens since the slot becomes electrically small to the point of being almost invisible to the microstrip line. For the bent microstrip line, there are discontinuities in the line associated with the corners necessary to wrap the line about the slot. These discontinuities cause a reflection in the

line before the signal gets from one port to another. These reflections add in phase at 1.27 GHz to yield a good match. Since these lines are electrically small, that is the only strong cancellation effect seen to improve the match. Again at low frequencies, the aperture becomes electrically small and its effects are almost negligible. These cases are shown as a reference for the next set of measurements, which is the ferrite loaded cavity.

The next set of measurements examined are the ferrite loaded cavity with the straight microstrip line in Figure 54. The ferrite is biased by two permanent magnets. For the parallel case we see the same magnetostatic resonance in S_{11} at 1.87 GHz, that was discussed last quarter. For the perpendicular case, the resonance shifts to a frequency greater than 2 GHz. This effect occurs due to the rotation of both the slot and the microstrip line thereby changing the coupling mechanism. Both nulls in S_{11} are very deep and narrow, obviously a high Q resonance. By examining the nulls in S_{21} for the parallel and perpendicular cases, the perpendicular case's null is slightly broader. Unfortunately, no lower frequency magnetostatic modes are seen.

The last set of measurements examined in this section are the ferrite loaded cavity with the bent microstrip line for the parallel and perpendicular configurations in Figure 55. Again, the ferrite is biased by two permanent magnets. For the parallel case we see the same magnetostatic resonance in S_{11} at 1.87 GHz; however its null is not very deep (-9.6 dB). For the perpendicular case, the resonance shifts to a 1.92 GHz and its null is extremely deep (\ll -40 dB). Again, this change between S_{11} occurs due to the rotation of both the slot and the microstrip line, thereby changing the coupling mechanism to the magnetostatic mode. Unfortunately, no lower frequency magnetostatic modes are seen by this case either.

Putting the all the measurements together, one can come to the following conclusions. By examining the nulls seen in Figure 55 only the perpendicular bent line is coupled strongly to the cavity. Given the direction of magnetization and the cavity and slot dimensions, this must be a magnetostatic surface wave mode. For the straight configurations, Figure 54, the resonance simply changed in frequency. To excite a magnetostatic volume wave mode for the given cavity configuration, a different feed system must be considered .

The volume wave mode has a vertical magnetic field which must be excited to see a low frequency resonance. Thus far, our feeds have been isolated from the ferrite through the slot. To couple strongly to this vertical component of the magnetic field, a mechanism must be used which can excite a

vertical magnetic field. Obviously, a vertical magnetic dipole could perform this task but it is a fictitious device. An electric current loop could also excite a vertical magnetic field. This loop must be located close the ferrite, in the cavity, to avoid any modal distortion seen by coupling through the slot like the previous efforts. Therefore, this new feed, probe, must lie within the cavity. Modifications to the fixture must be performed to be able to place the probe in the cavity. This is the next configuration type to be considered in the experiments.

6. Future Work

The analysis of the three-dimensional CBS filled with ferrite and dielectric layers will continue. When the ferrite layer is correctly added to the analysis capability, information on tuning the slot, material losses, and radar cross section vs. magnetization and frequency will be available. Also, the derivation of the theory necessary to include the feed will begin. Once the feed is added to the analysis capabilities, radiation, input impedance and other useful information can be extracted.

Additional experimental work on modifications to the cavity and feed network will be performed. The goal of modifying the cavity and feed is to strongly excite the volume wave mode seen in the power pattern measurements and in the previous cavity design. Also, some possible ways to control the bias field may be considered.

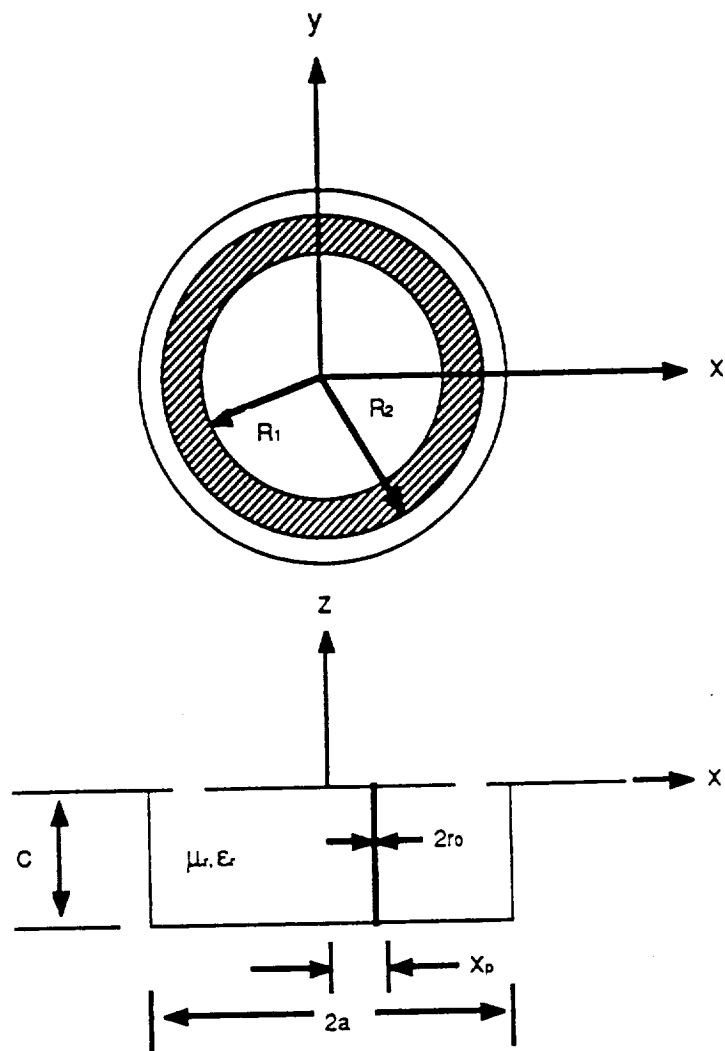


Figure 26: Geometry of a probe fed circular patch backed by a circular cavity.

- THEORETICAL
- EXPERIMENTAL

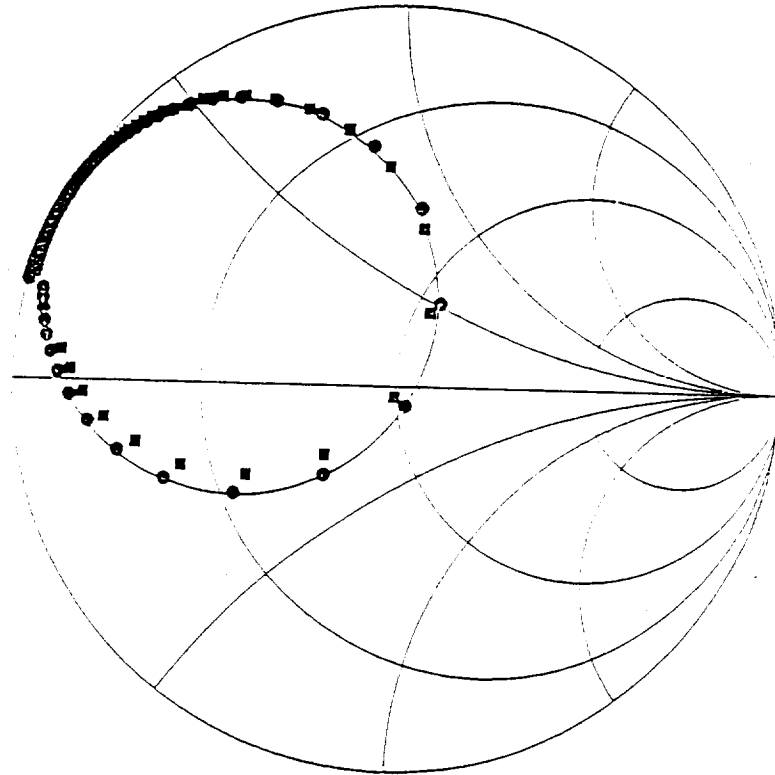


Figure 27: Input impedance versus frequency for circular cavity-backed circular patch on Smith chart (experimental and theoretical results) ($\epsilon_r = 2.2$).

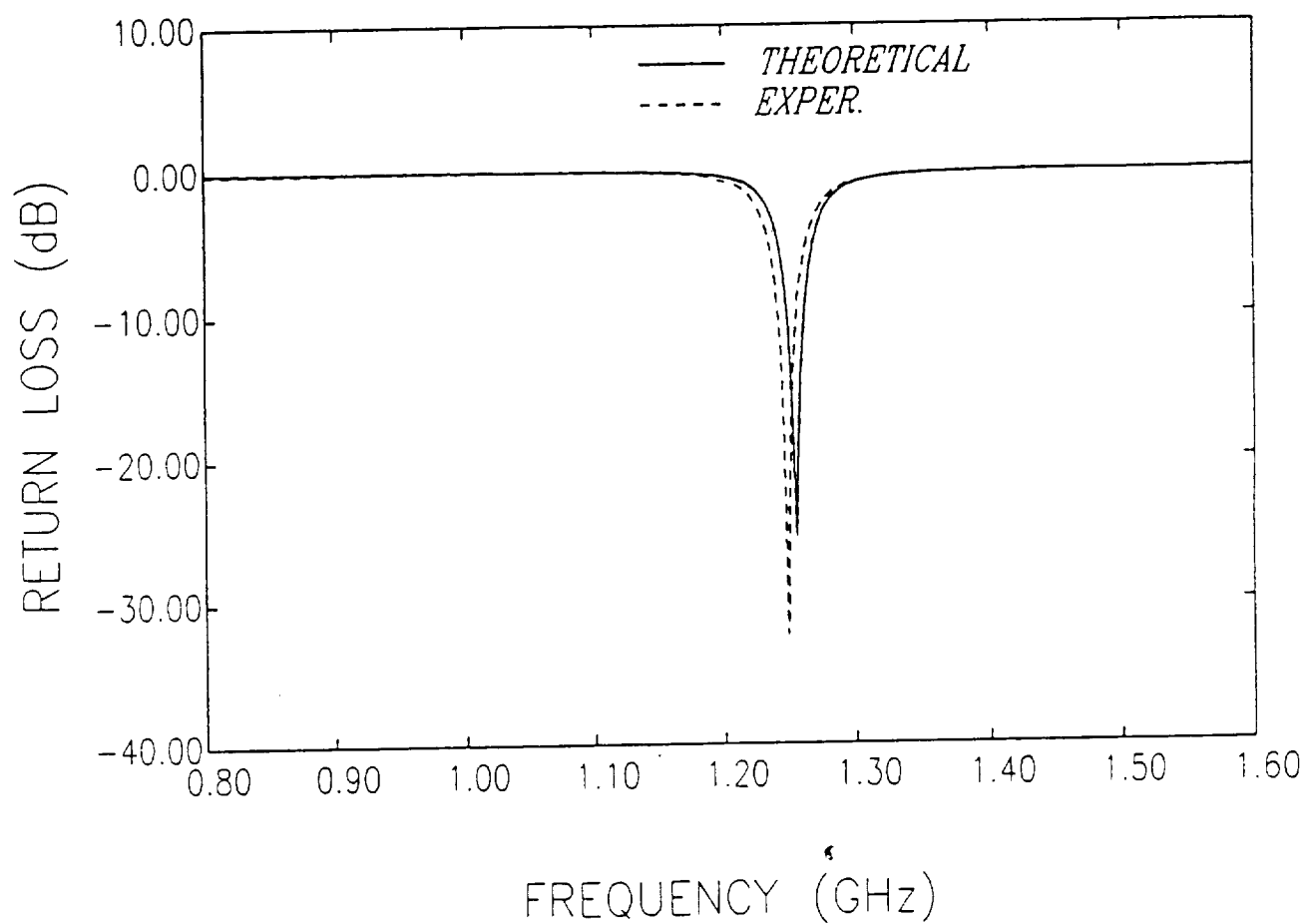


Figure 28: Return loss versus frequency for circular cavity-backed circular patch (experimental and theoretical results) ($\epsilon_r = 2.2$).

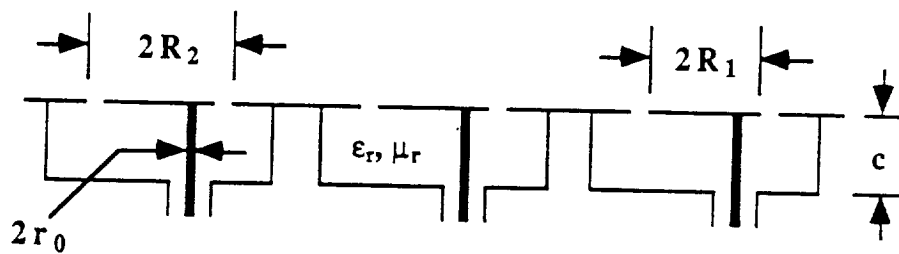
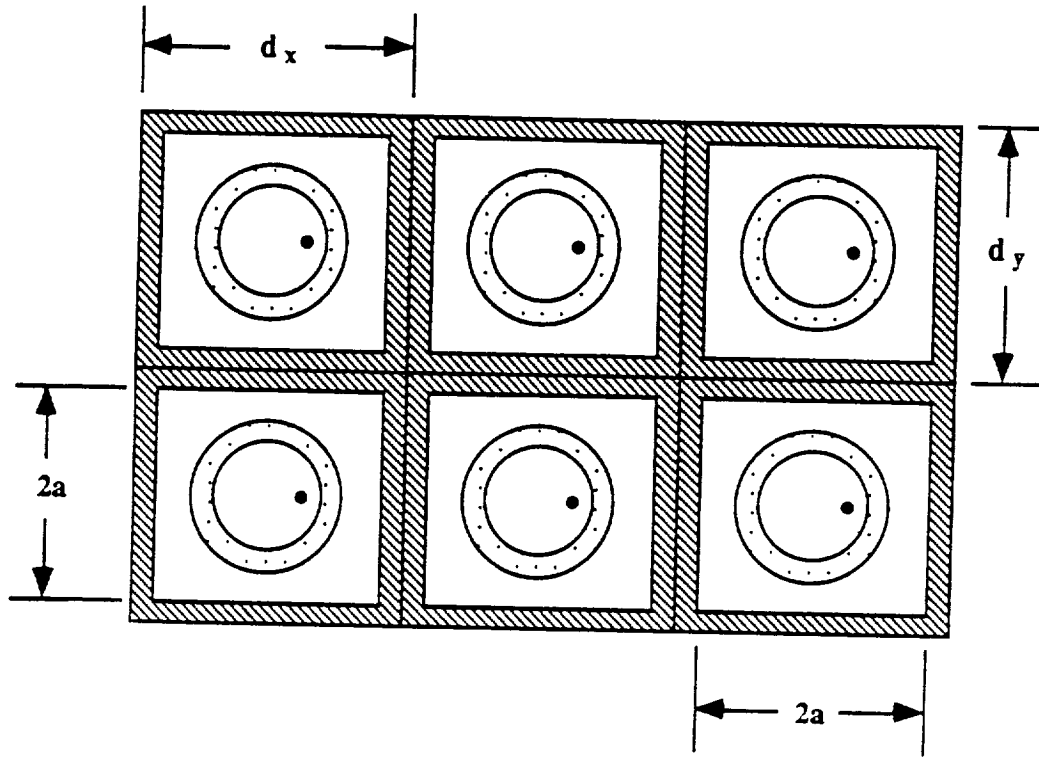
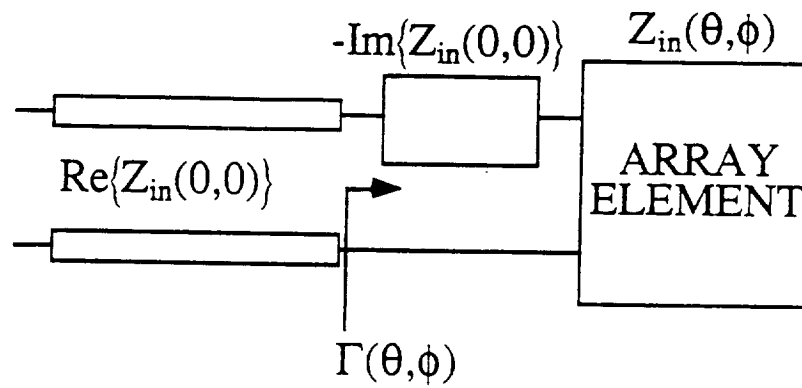


Figure 29: Schematic of an infinite array of probe fed circular microstrip patches each backed by a circular cavity.



$$\Gamma(\theta, \phi) = \frac{Z_{in}(\theta, \phi) - Z_{in}(0, 0)}{Z_{in}(\theta, \phi) + Z_{in}^*(0, 0)}$$

Figure 30: Broadside-matched active element reflection coefficient of the cavity-backed patch antenna.

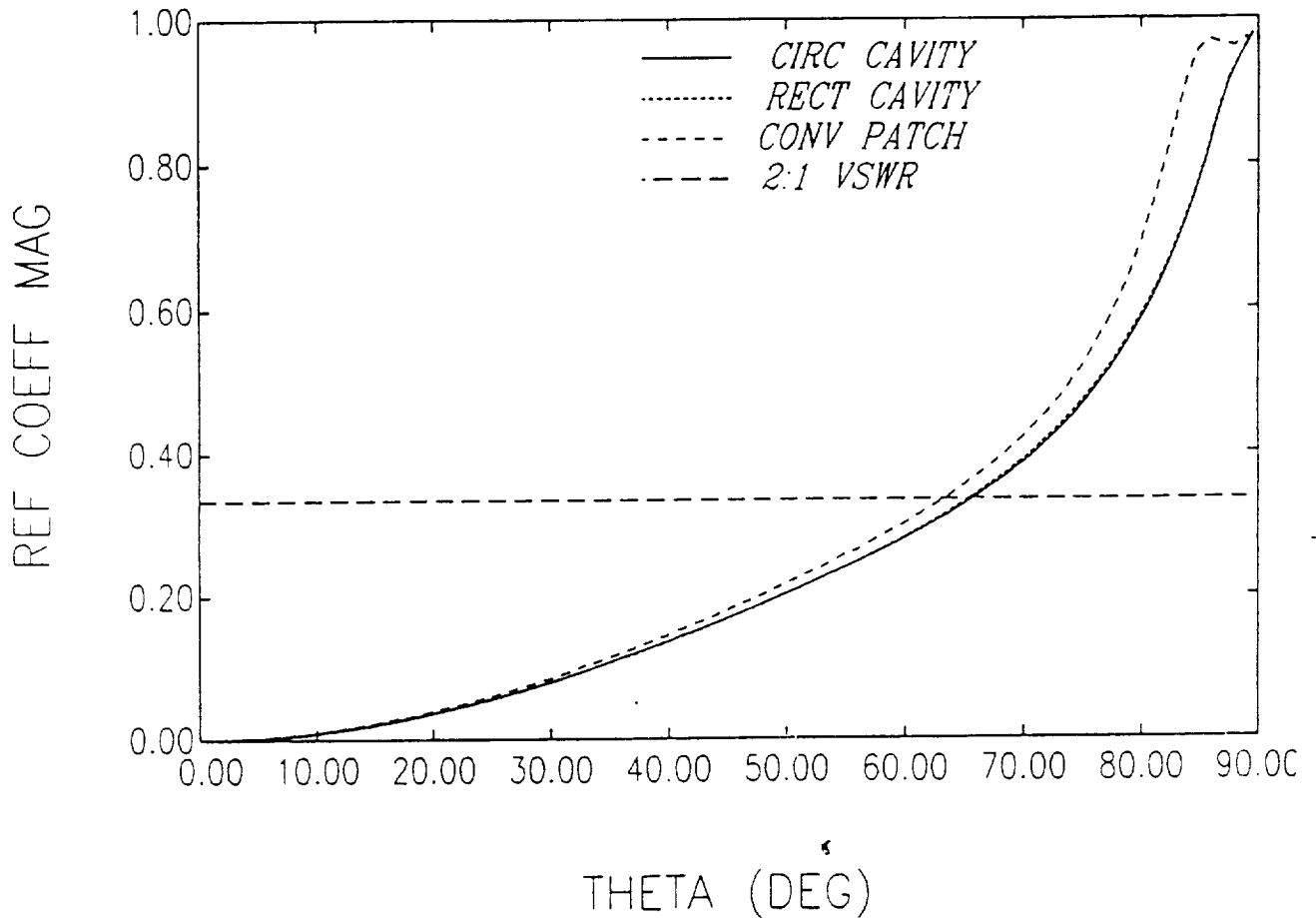


Figure 31: E-plane broadside-matched reflection coefficient versus scan angle for infinite arrays of circular and rectangular cavity-backed and conventional patches ($d=0.02 \lambda_0$).

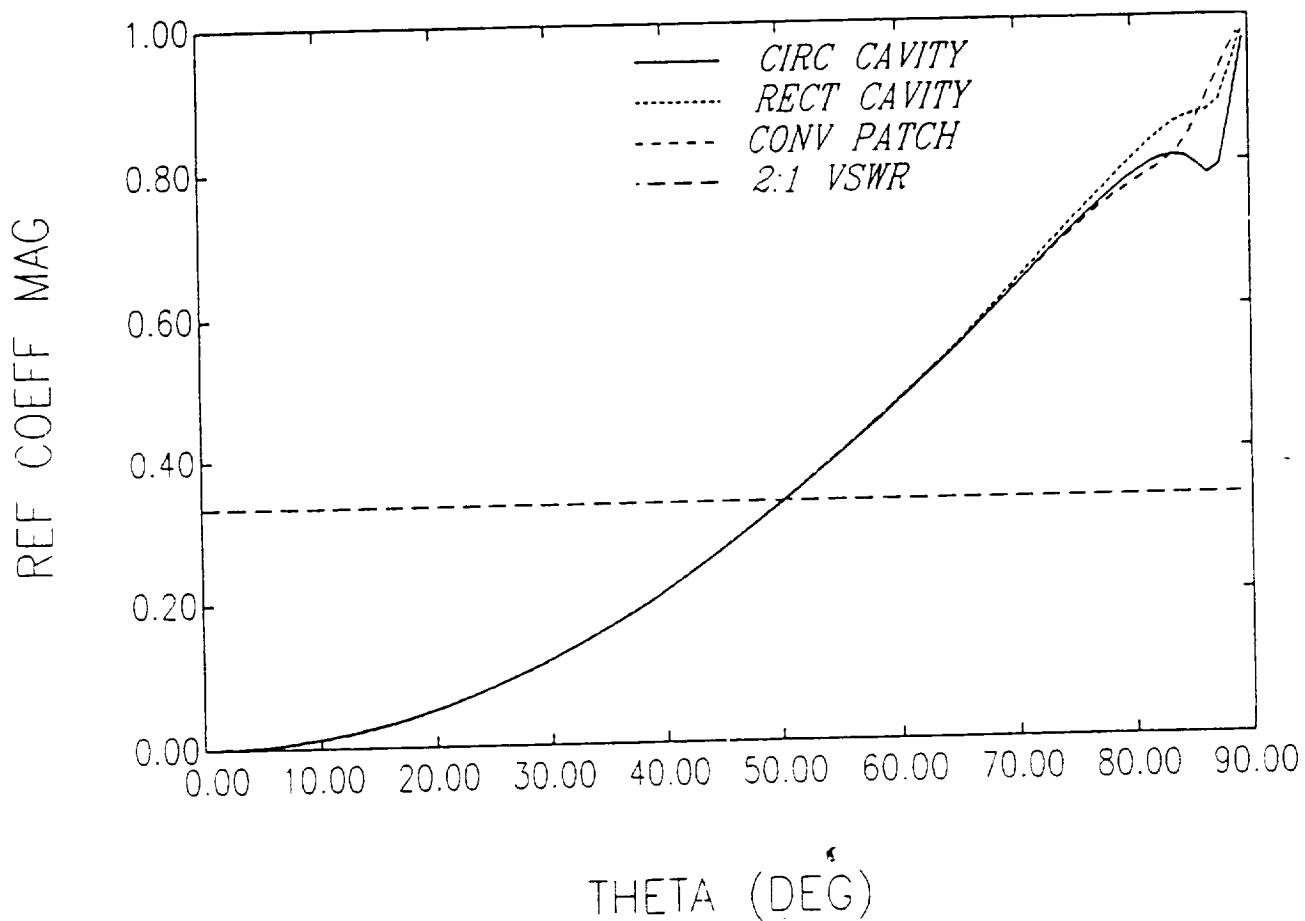


Figure 32: H-plane broadside-matched reflection coefficient versus scan angle for infinite arrays of circular and rectangular cavity-backed and conventional patches ($d=0.02 \lambda_0$).

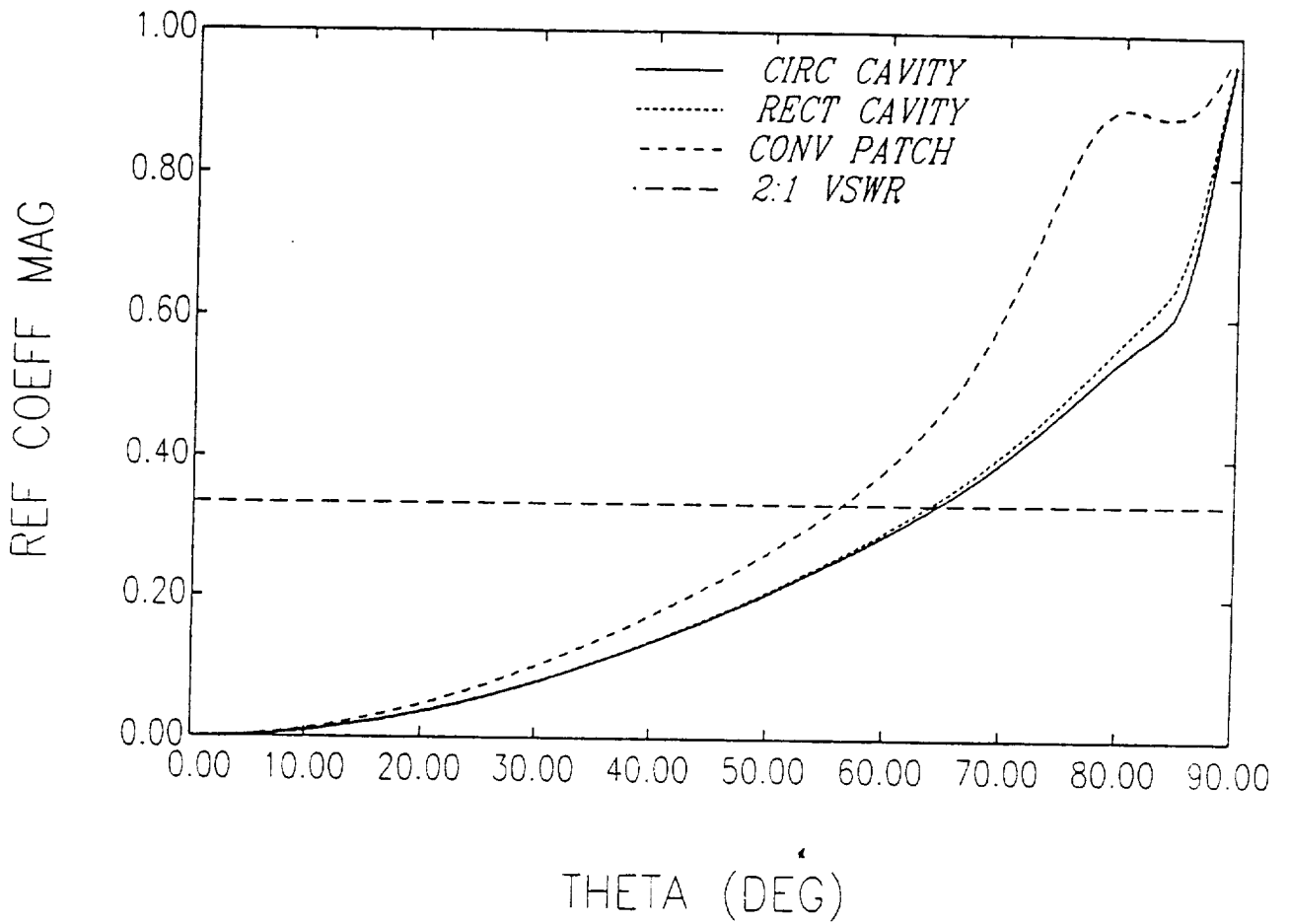


Figure 33: E-plane broadside-matched reflection coefficient versus scan angle for infinite arrays of circular and rectangular cavity-backed and conventional patches ($d=0.05 \lambda_0$).

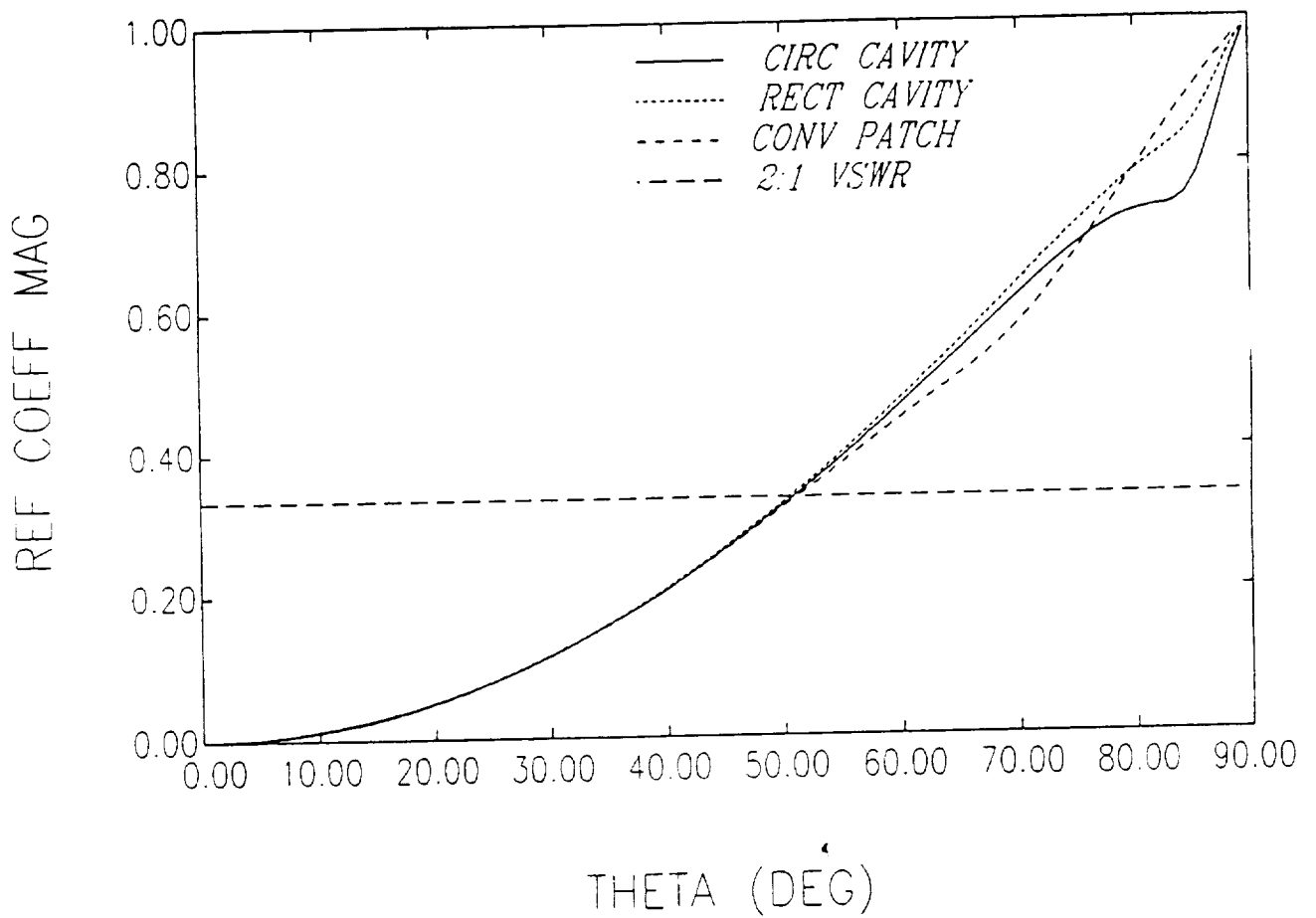


Figure 34: H-plane broadside-matched reflection coefficient versus scan angle for infinite arrays of circular and rectangular cavity-backed and conventional patches ($d=0.05 \lambda_0$).

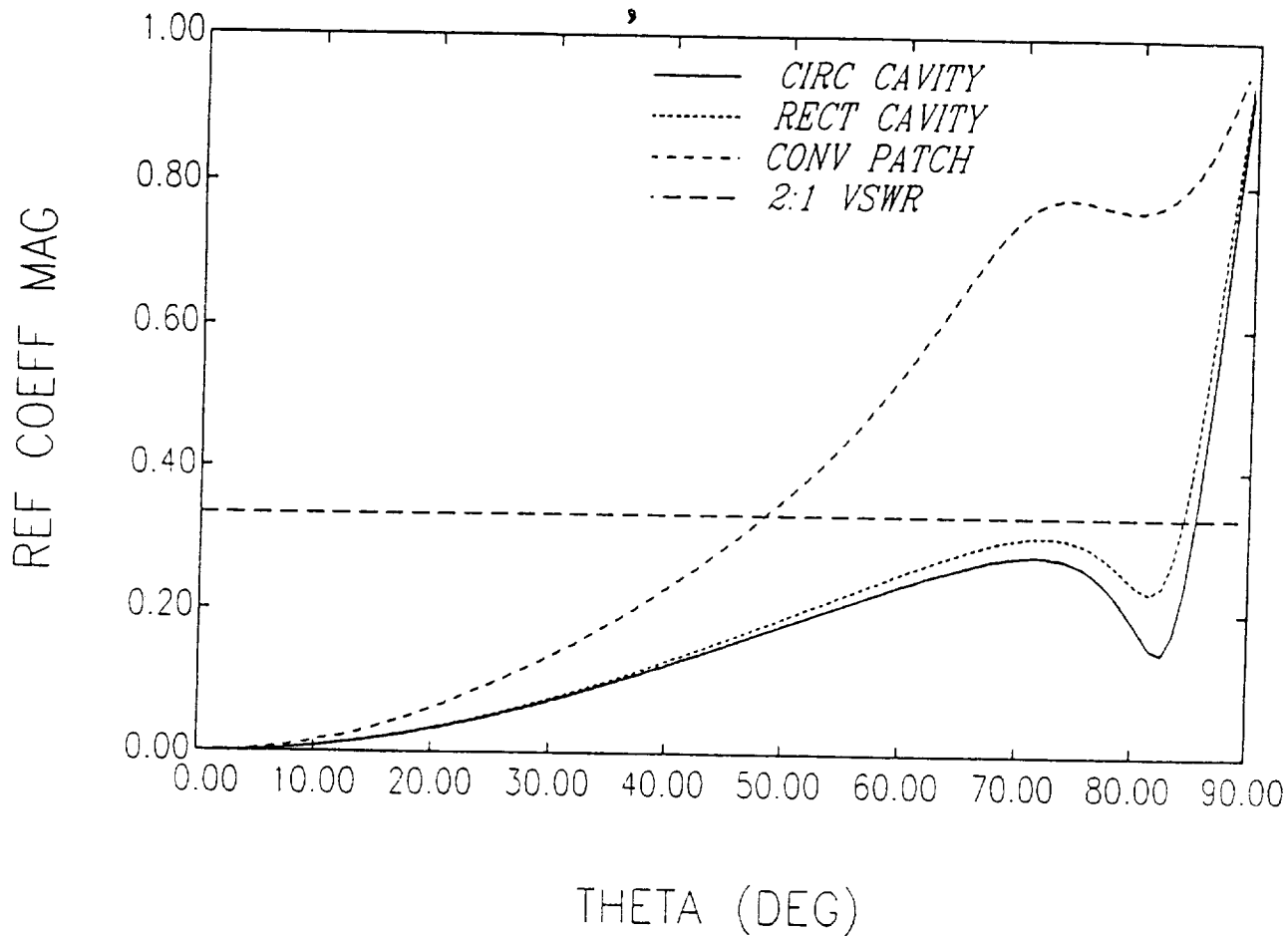


Figure 35: E-plane broadside-matched reflection coefficient versus scan angle for infinite arrays of circular and rectangular cavity-backed and conventional patches ($d=0.08 \lambda_0$).

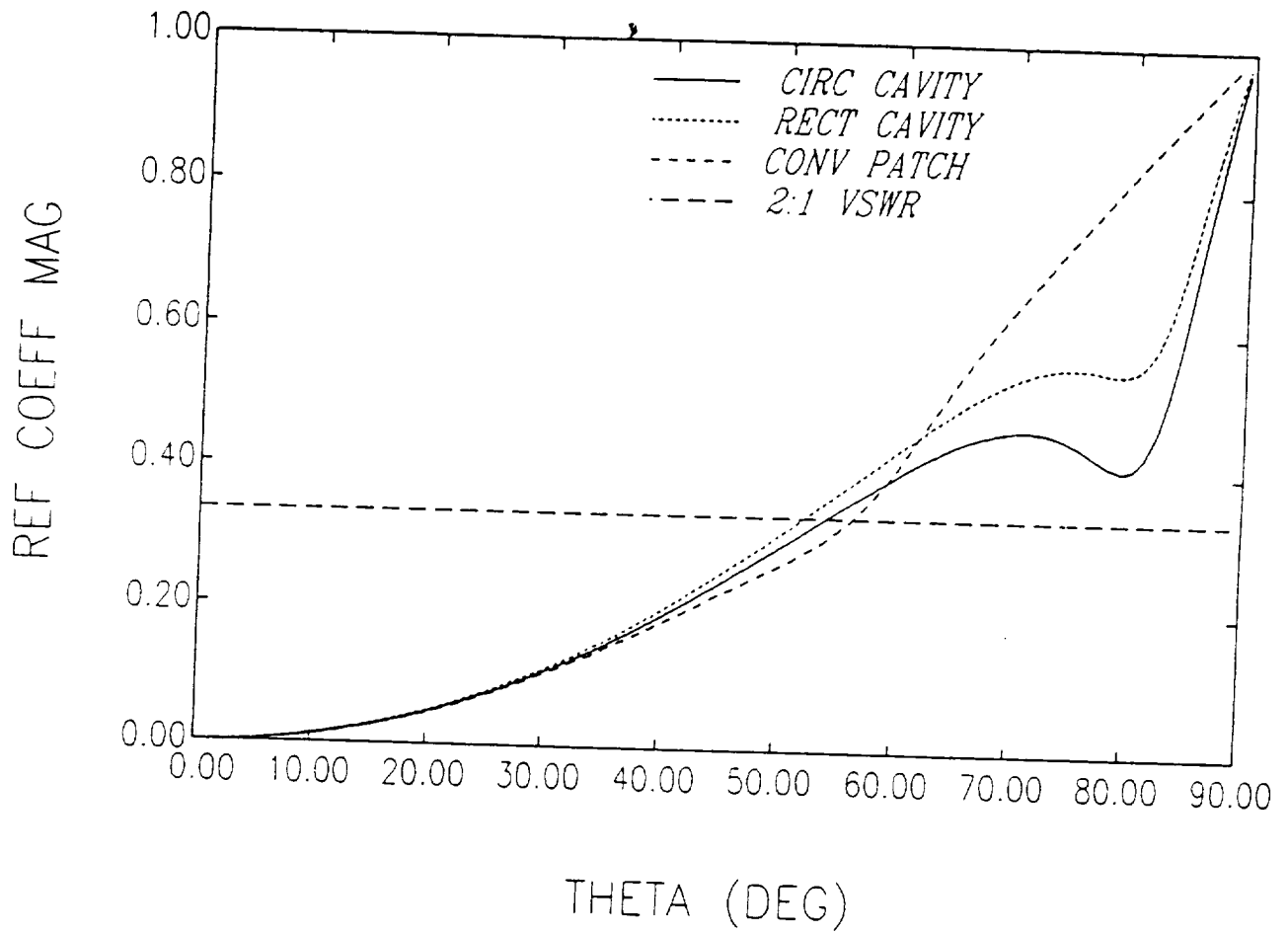


Figure 36: H-plane broadside-matched reflection coefficient versus scan angle for infinite arrays of circular and rectangular cavity-backed and conventional patches ($d=0.08 \lambda_0$).

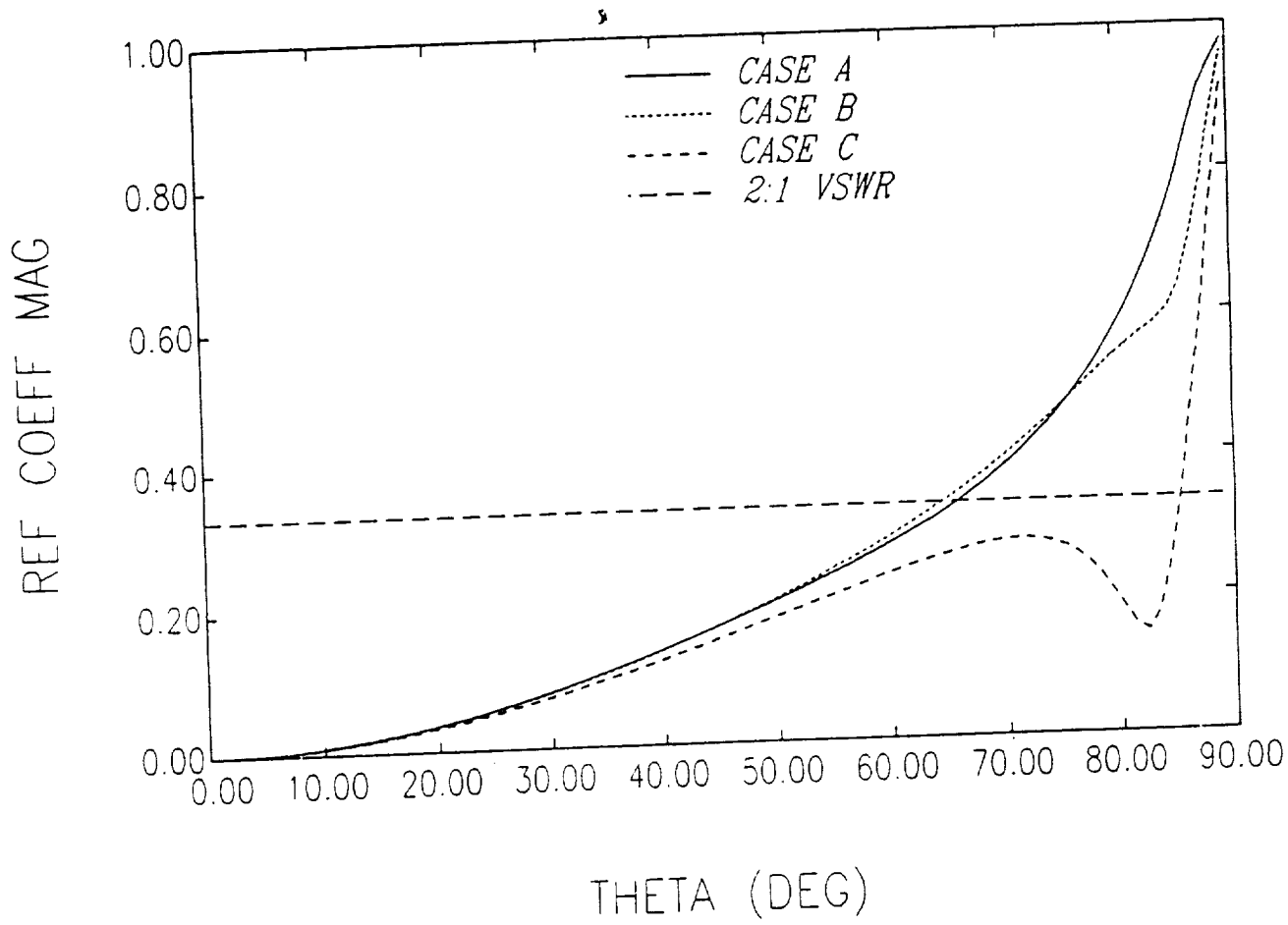


Figure 37: E-plane broadside-matched reflection coefficient versus scan angle for and infinite array of circular cavity-backed circular patches as a function of substrate thickness.

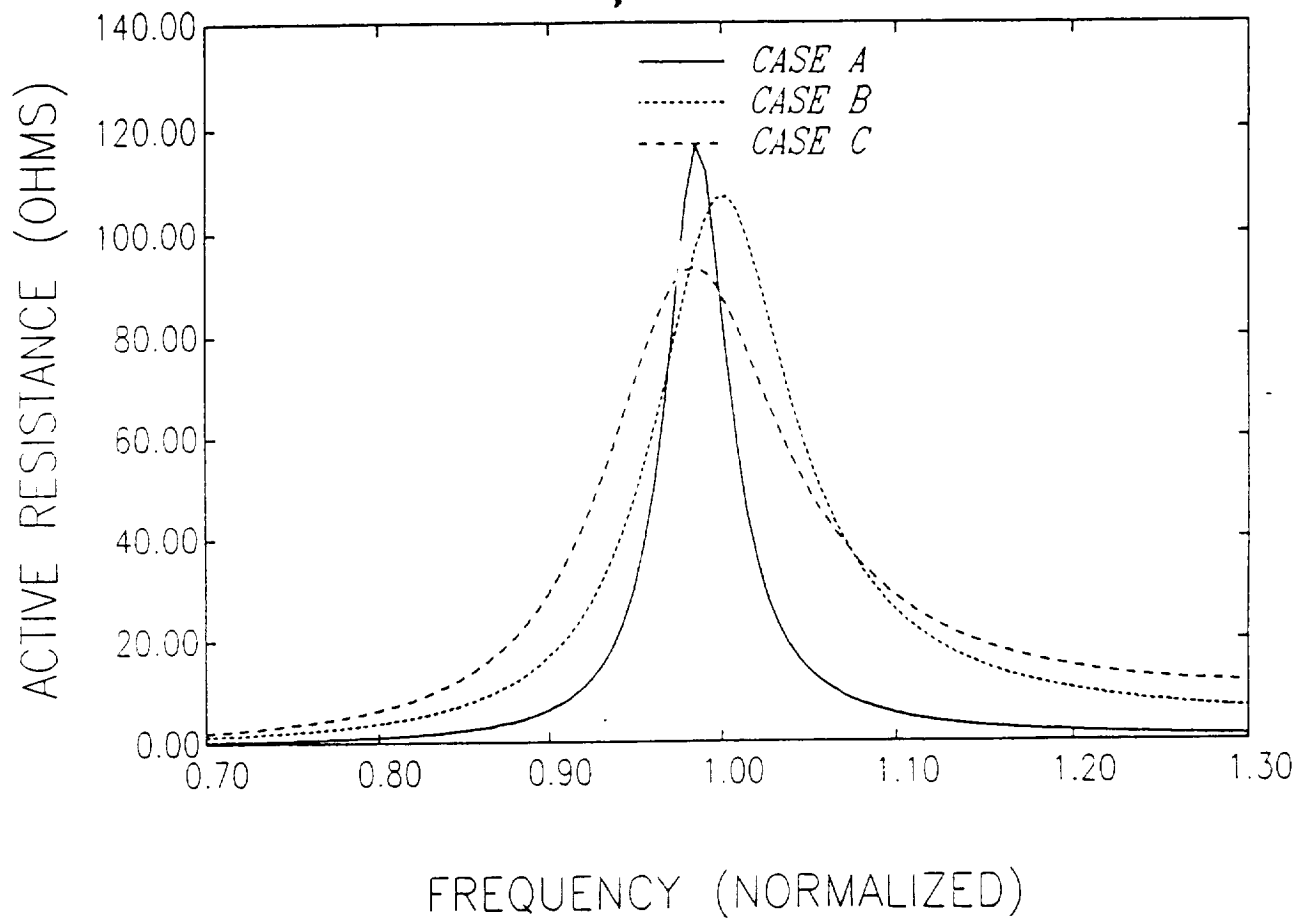


Figure 38: Active resistance versus frequency for an infinite array of circular cavity-backed circular patches as a function of substrate thickness.

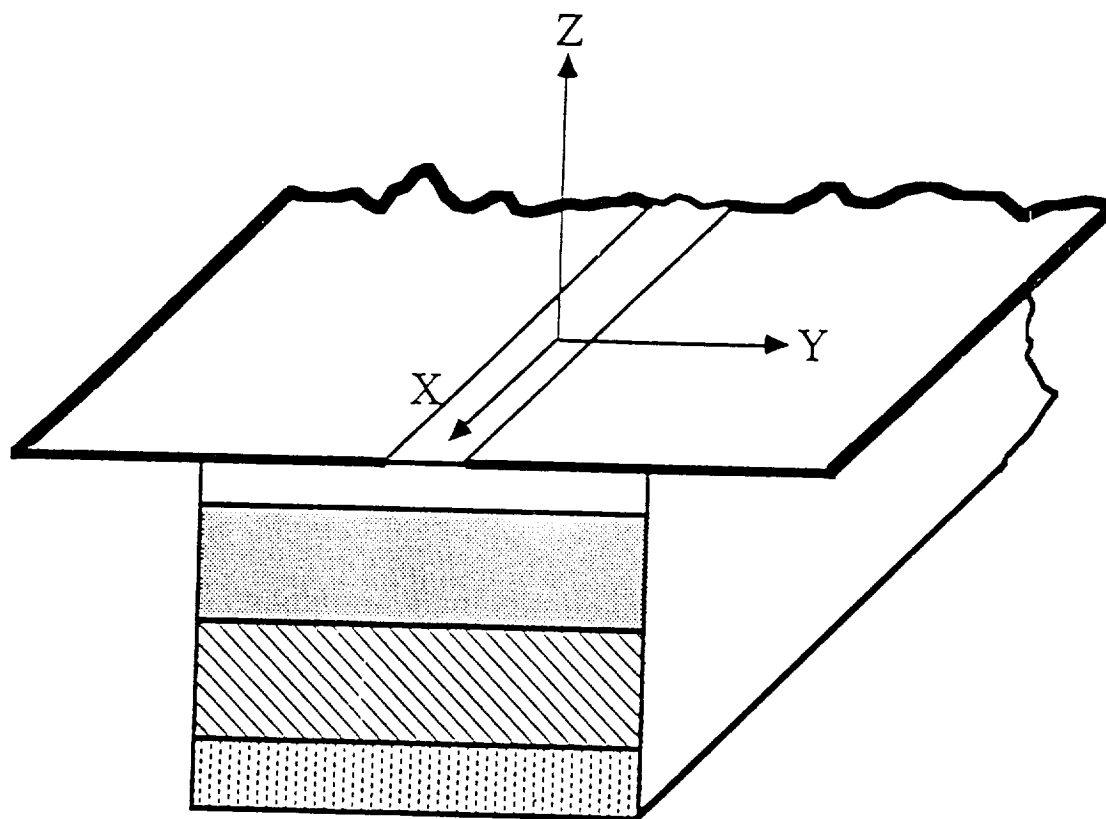


Figure 39: Cross section of two-dimensional CBS.

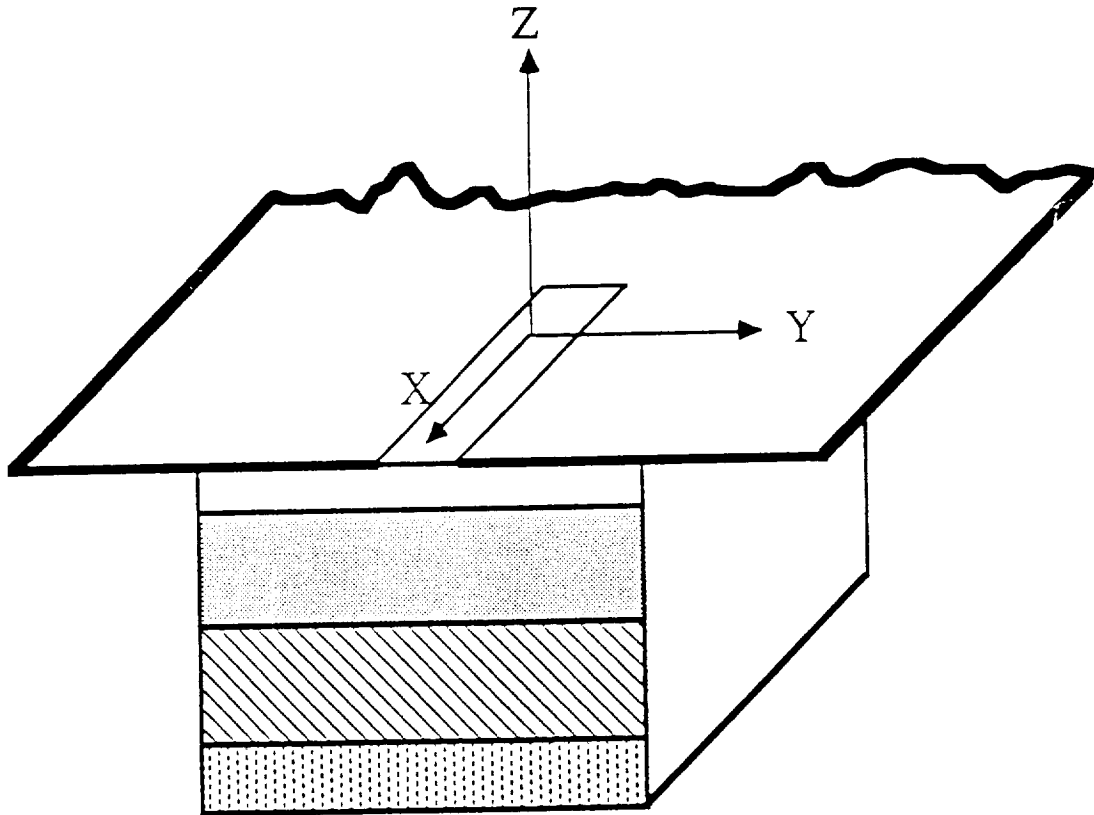


Figure 40: Cross section of three-dimensional CBS.

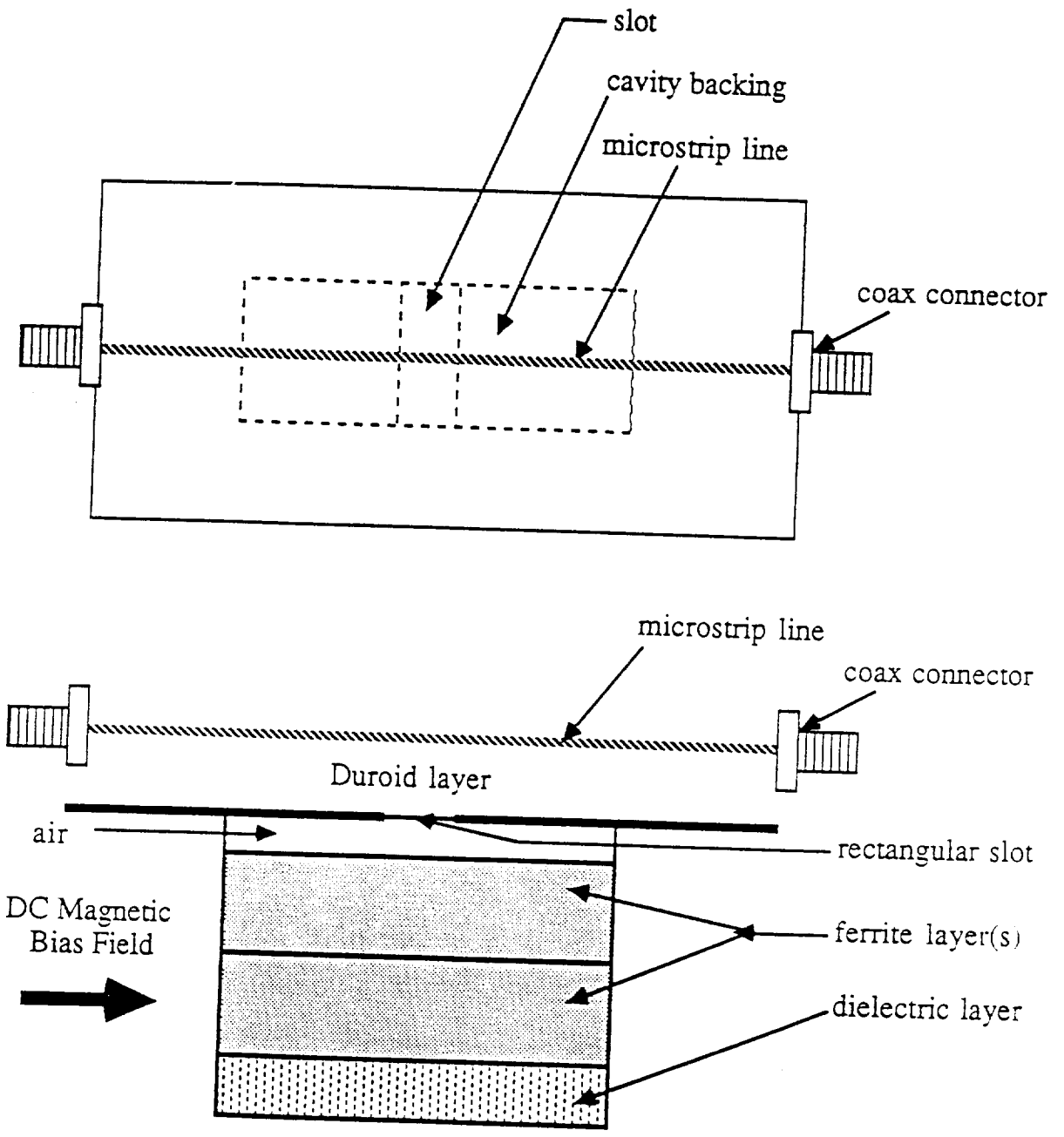


Figure 41: Top and side view of cavity experiment.

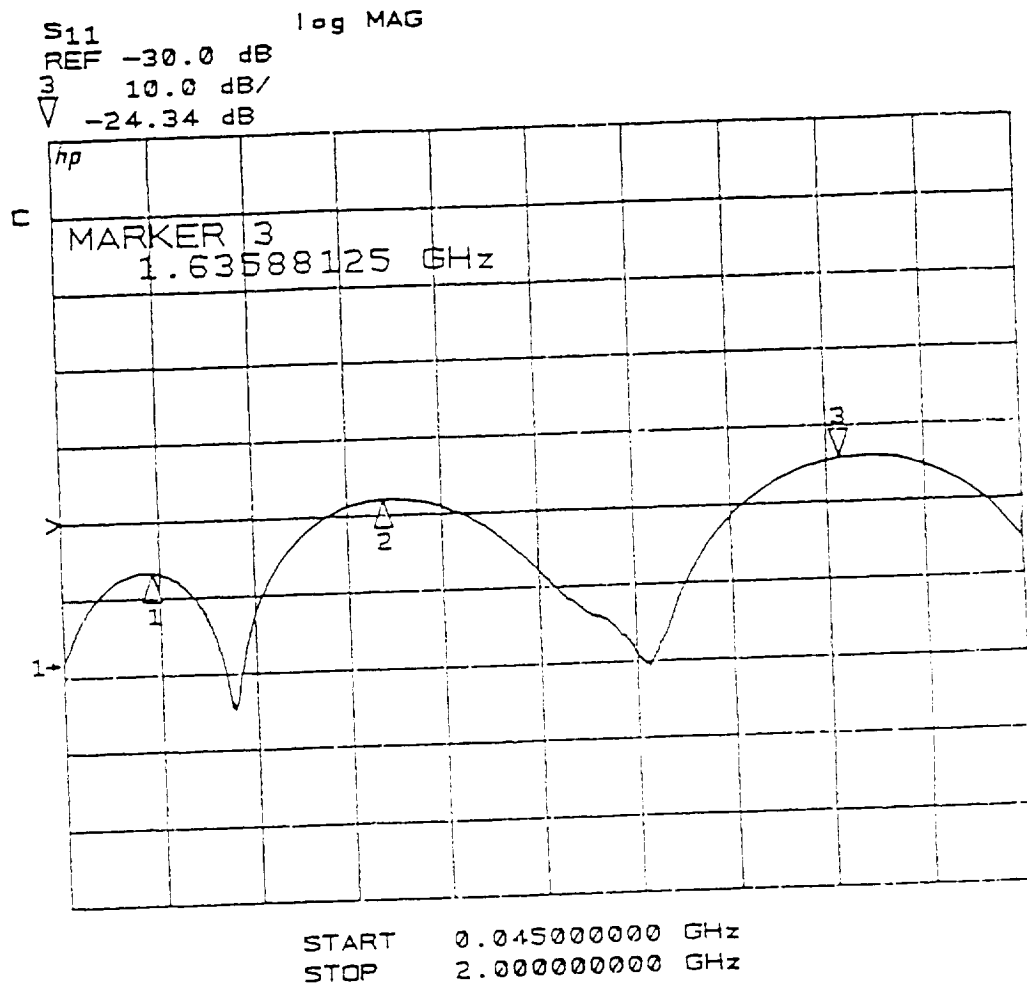


Figure 42: Return Loss of the microstrip line with the slot shorted.

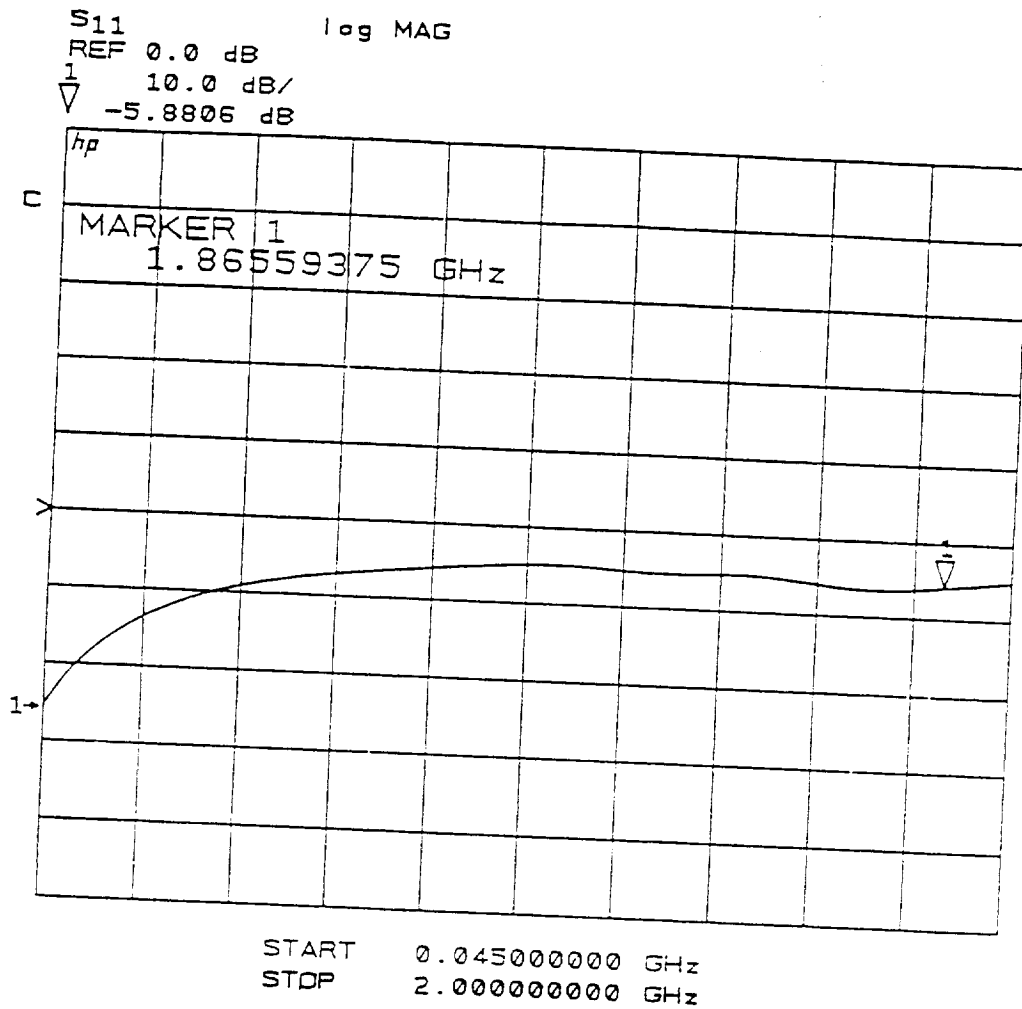


Figure 43: Return loss of the cavity loaded with ferrite and dielectric layer with no bias field applied.

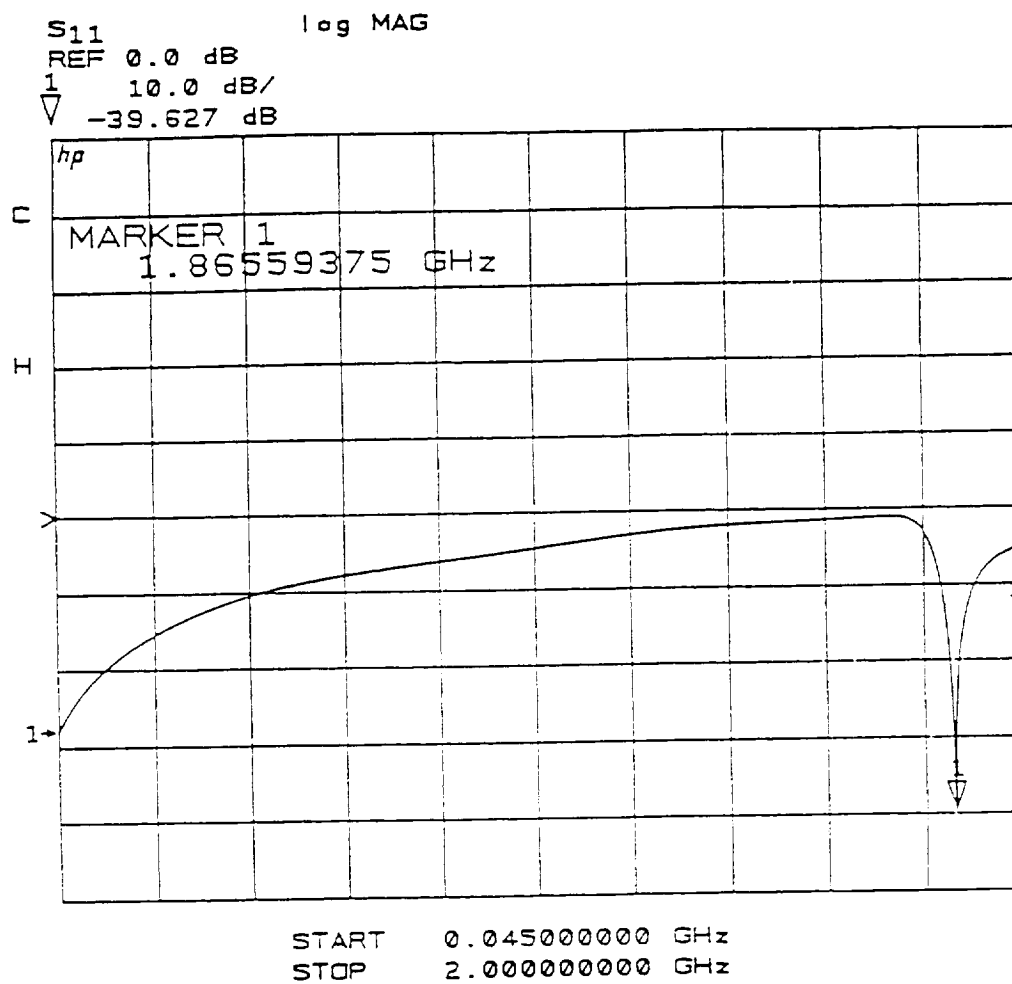


Figure 44: Return loss of the cavity loaded with ferrite and dielectric layer with maximum bias field applied.

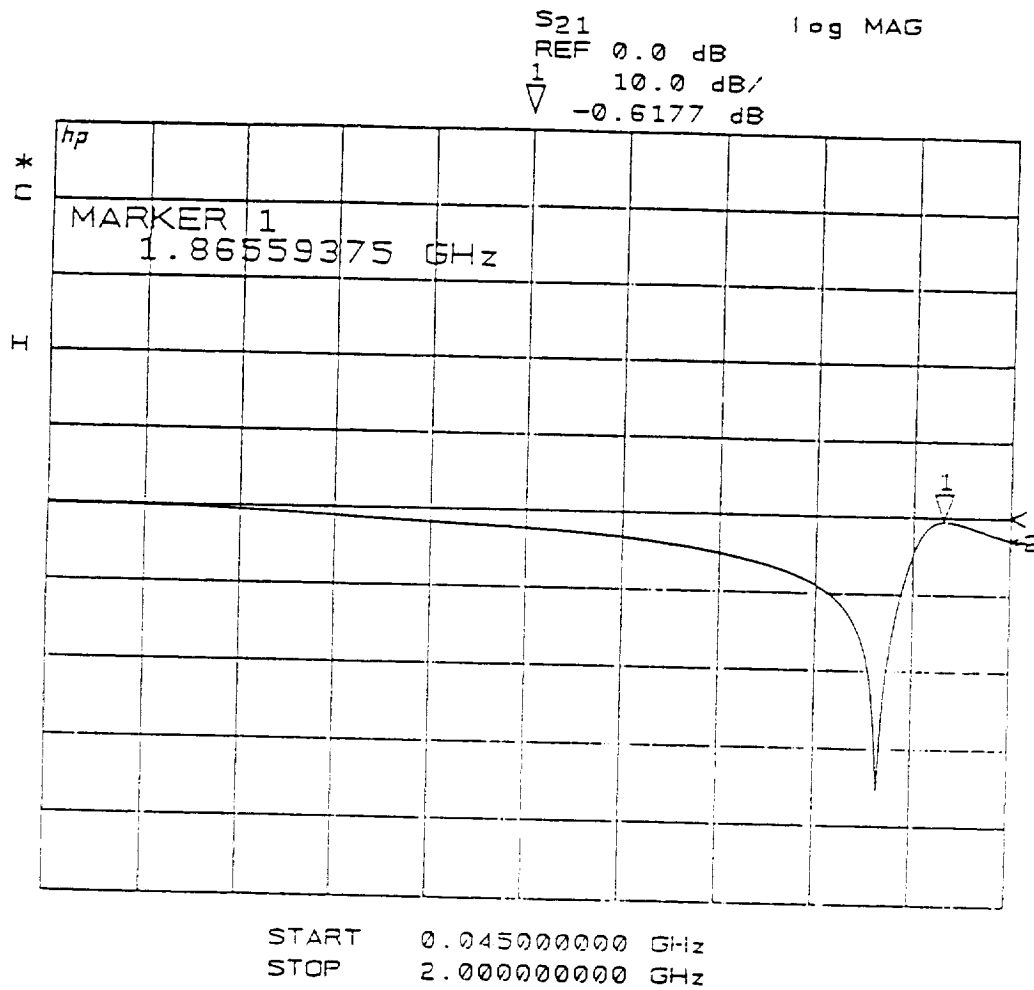


Figure 45: Insertion loss of the cavity loaded with ferrite and dielectric layer with maximum bias field applied.

dielectric filled cavity (vertical)
a030901.rep
A: VH
FREQUENCY = 1.748 GHz

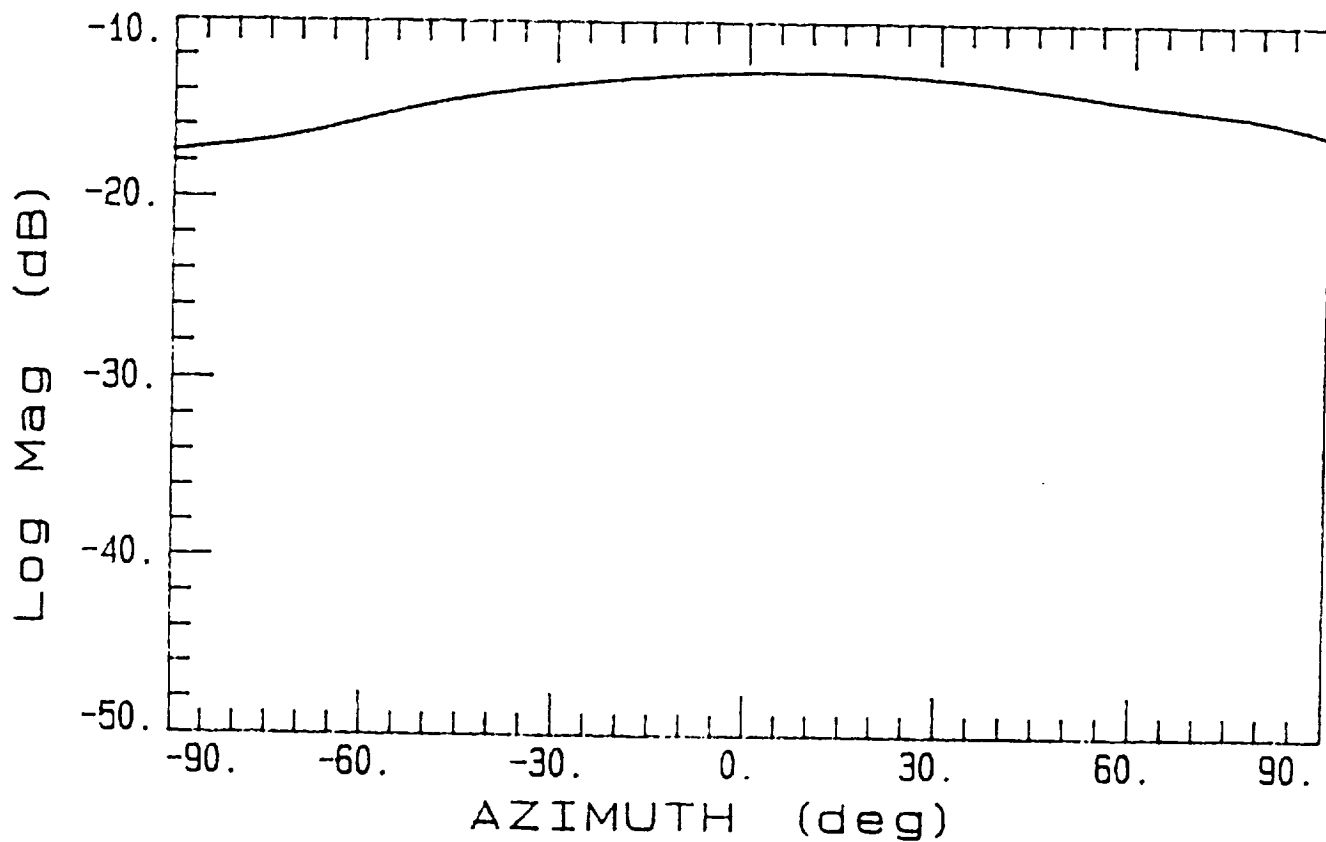


Figure 46: Power pattern cavity loaded with ferrite and dielectric layer with maximum bias field applied. (Vertical Polarization @ 1.748 GHz)

dielectric filled cavity (horizontal)
a031001.rep
A: HV
FREQUENCY = 1.748 GHz

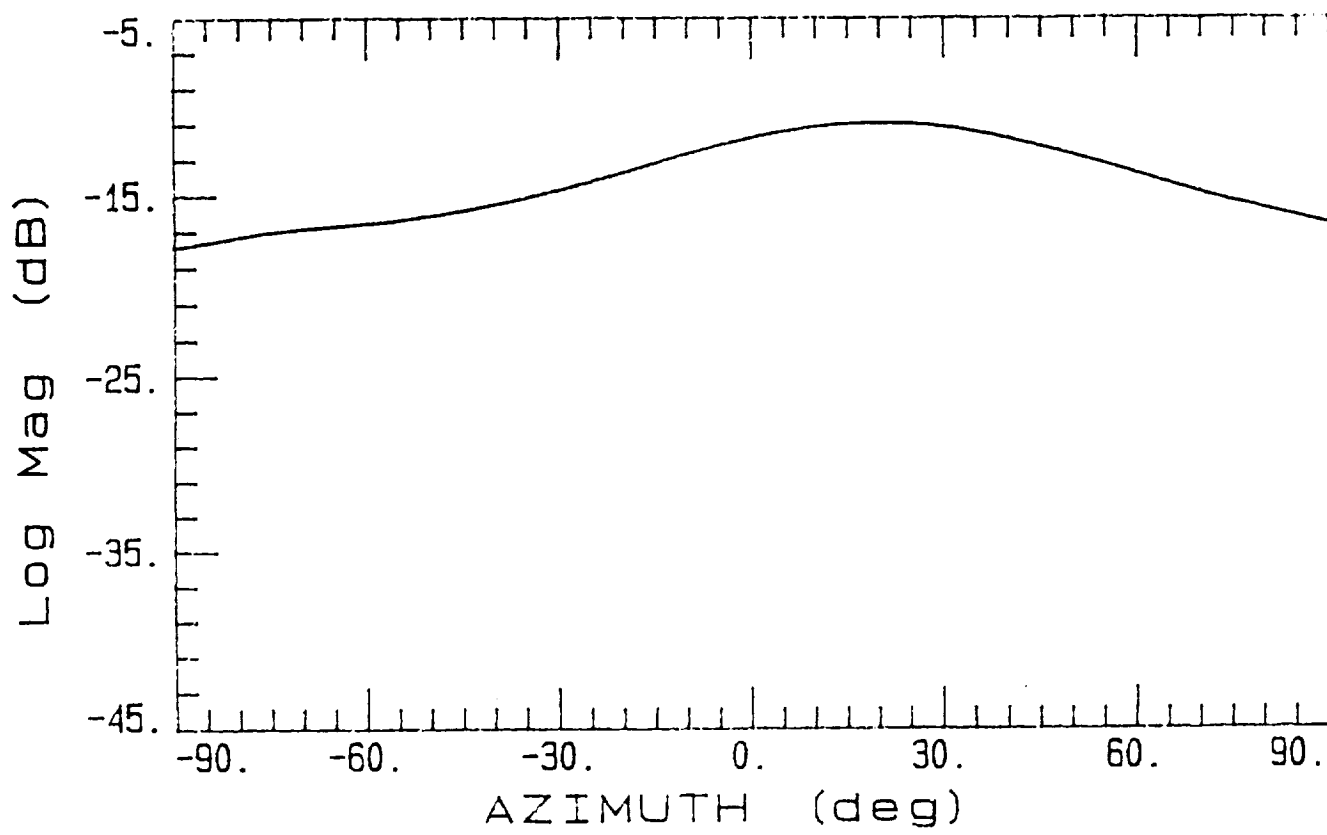


Figure 47: Power pattern cavity loaded with ferrite and dielectric layer with maximum bias field applied. (Horizontal Polarization @ 1.748 GHz)

dielectric filled cavity (vertical)
a030901.rep VH

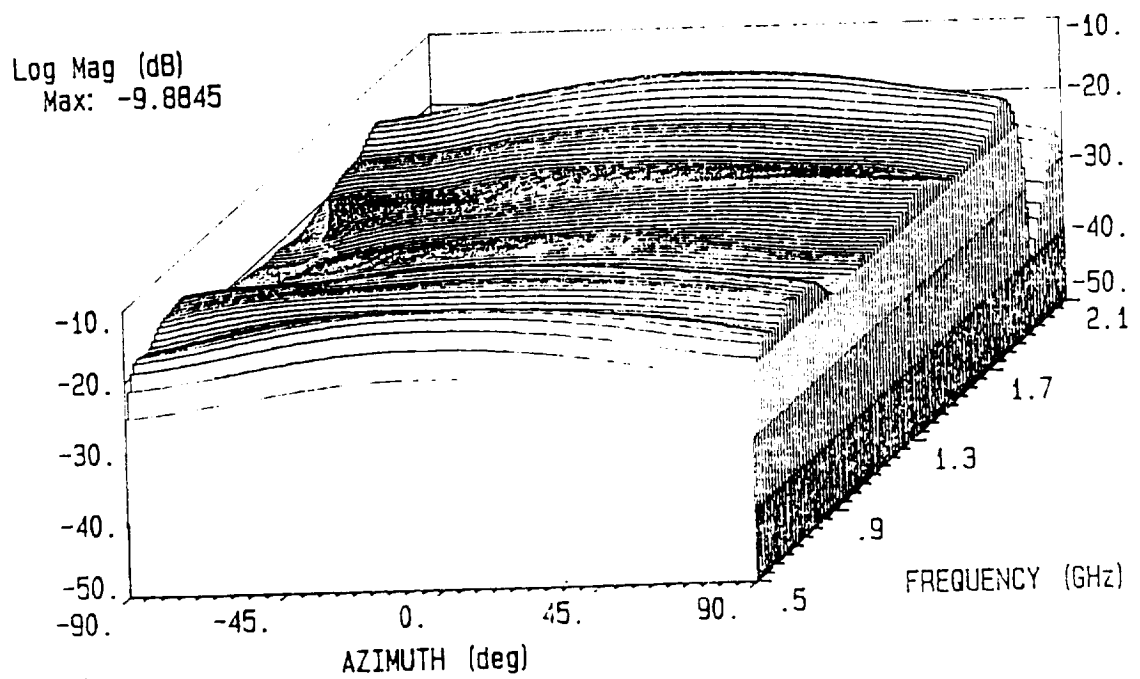


Figure 48: Power pattern cavity loaded with ferrite and dielectric layer with maximum bias field applied. (Vertical Polarization from 0.5 to 2.1 GHz)

dielectric filled cavity (horizontal)
a031001.rep HV

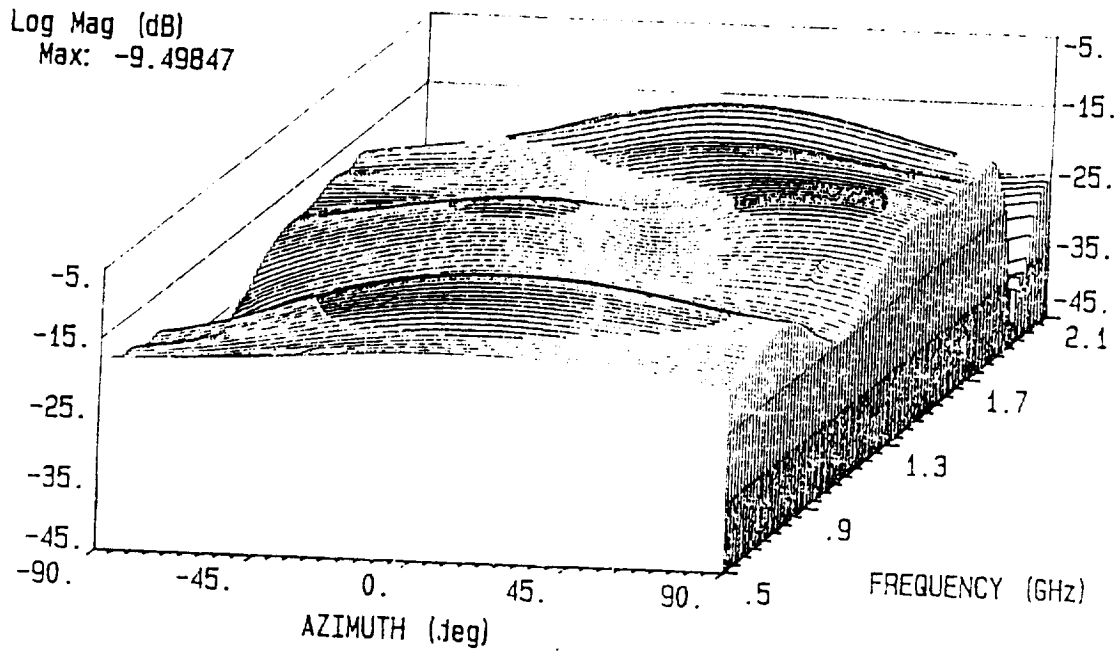


Figure 49: Power pattern cavity loaded with ferrite and dielectric layer with maximum bias field applied. (Horizontal Polarization from 0.5 to 2.1 GHz)

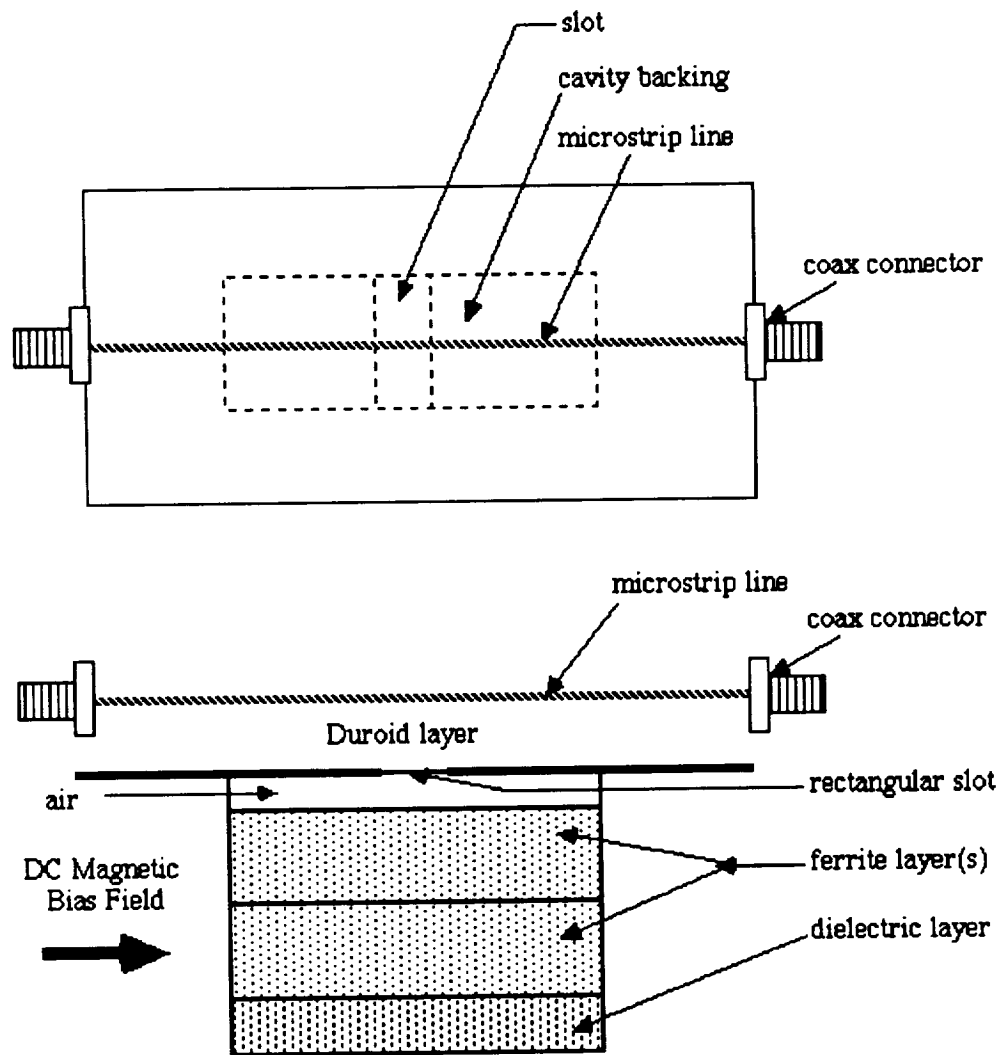
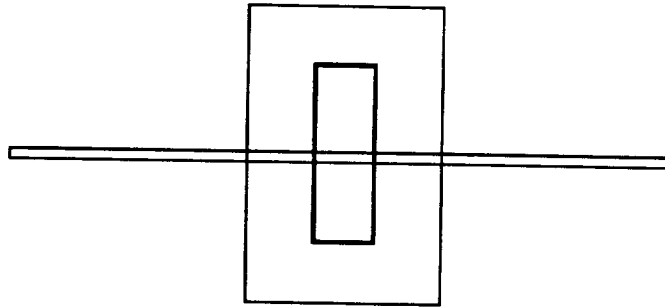
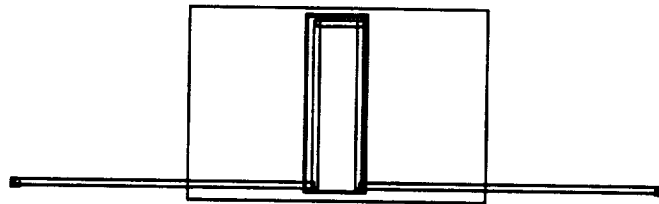


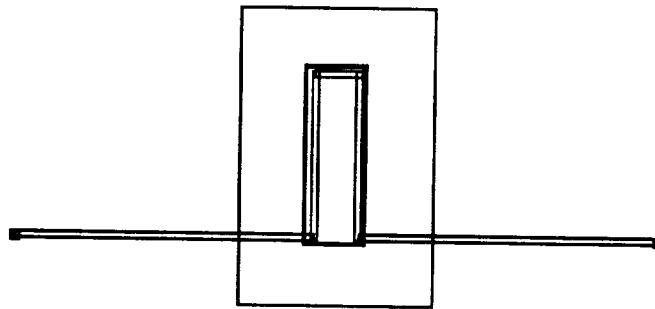
Figure 50: Original fixture for CBS antenna.



perpendicular straight



parallel bent



perpendicular bent

Figure 51: Slot/Microstrip configurations under examination.

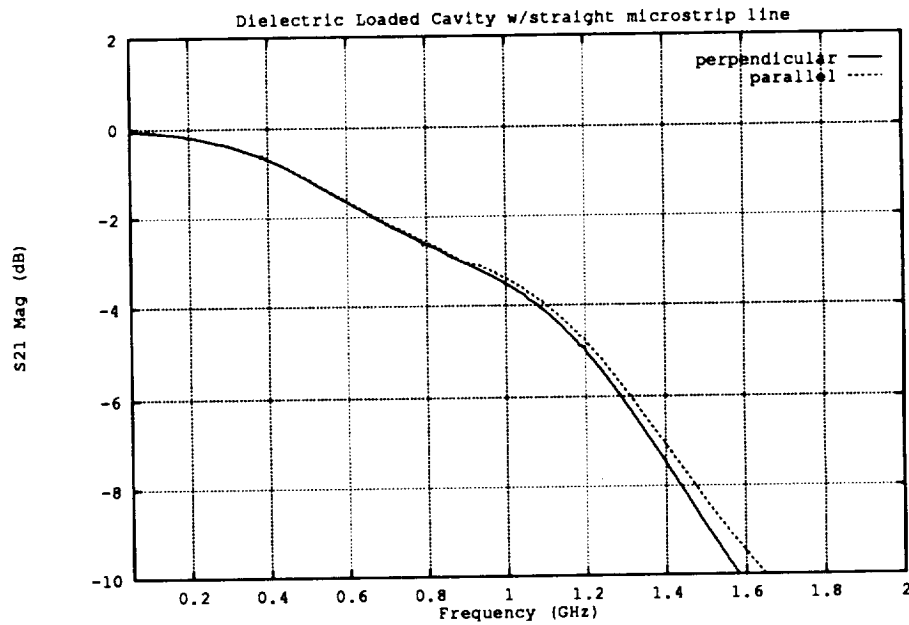
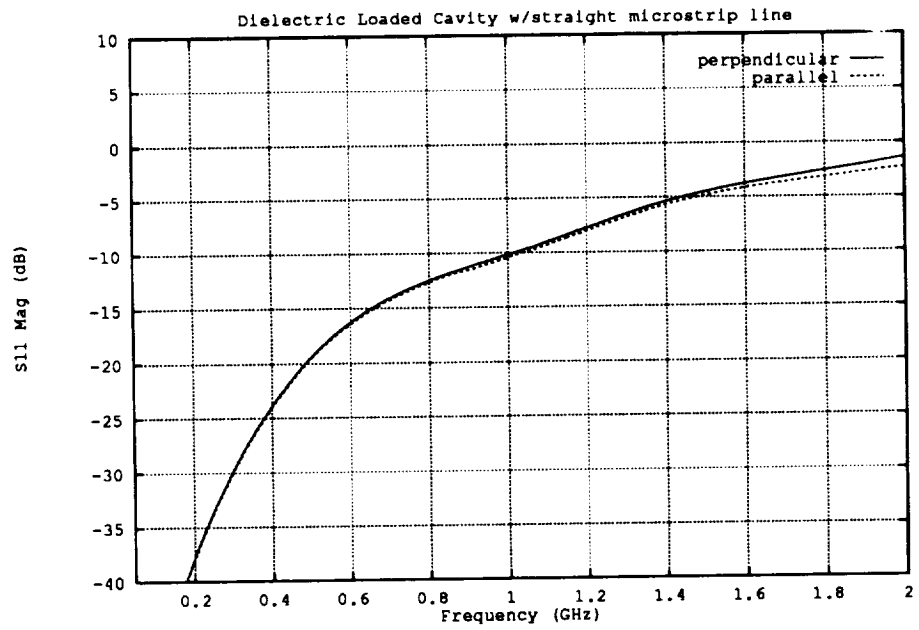


Figure 52: S_{11} and S_{21} of the Dielectric loaded cavity with the straight microstrip line.

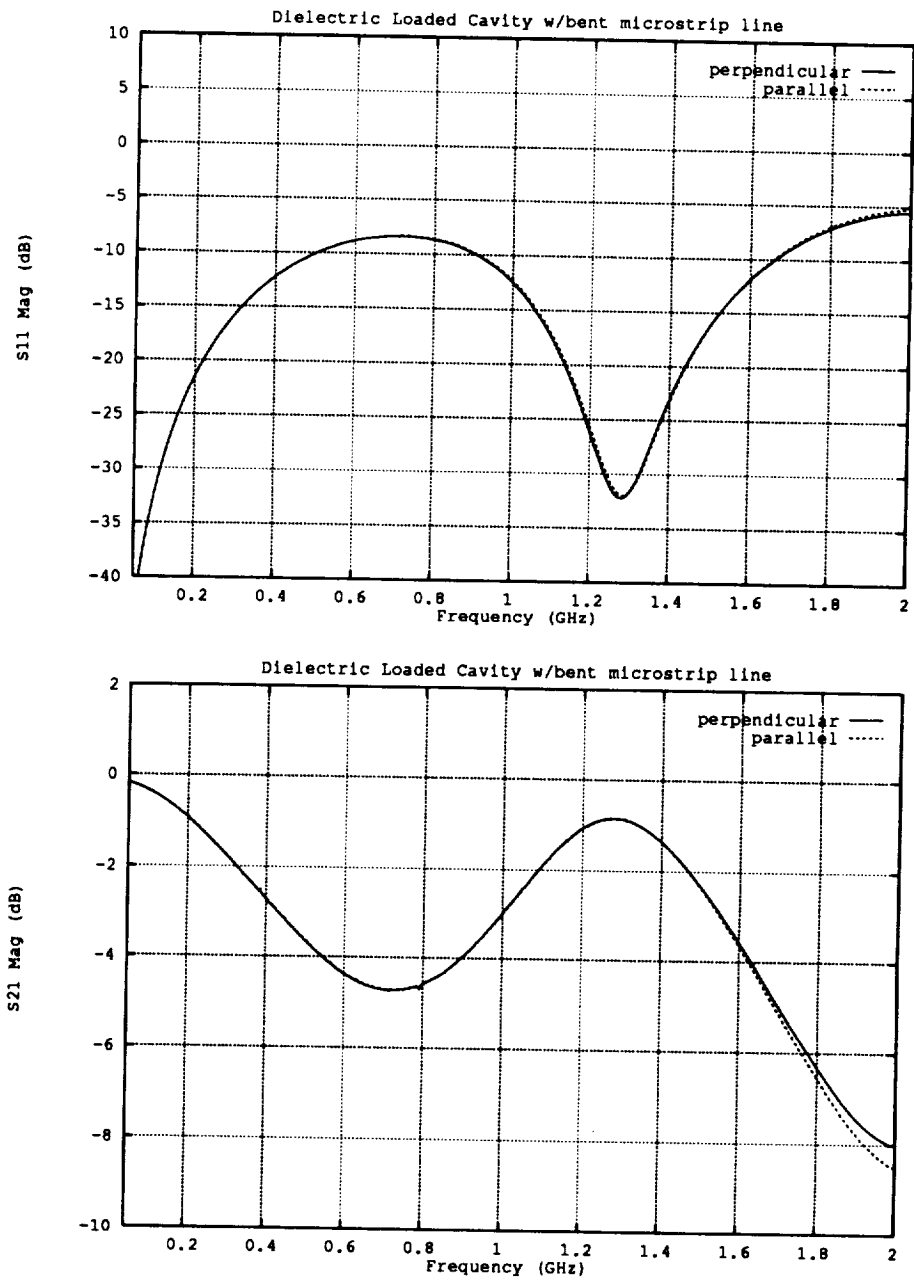


Figure 53: S_{11} and S_{21} of the Dielectric loaded cavity with the bent microstrip line.

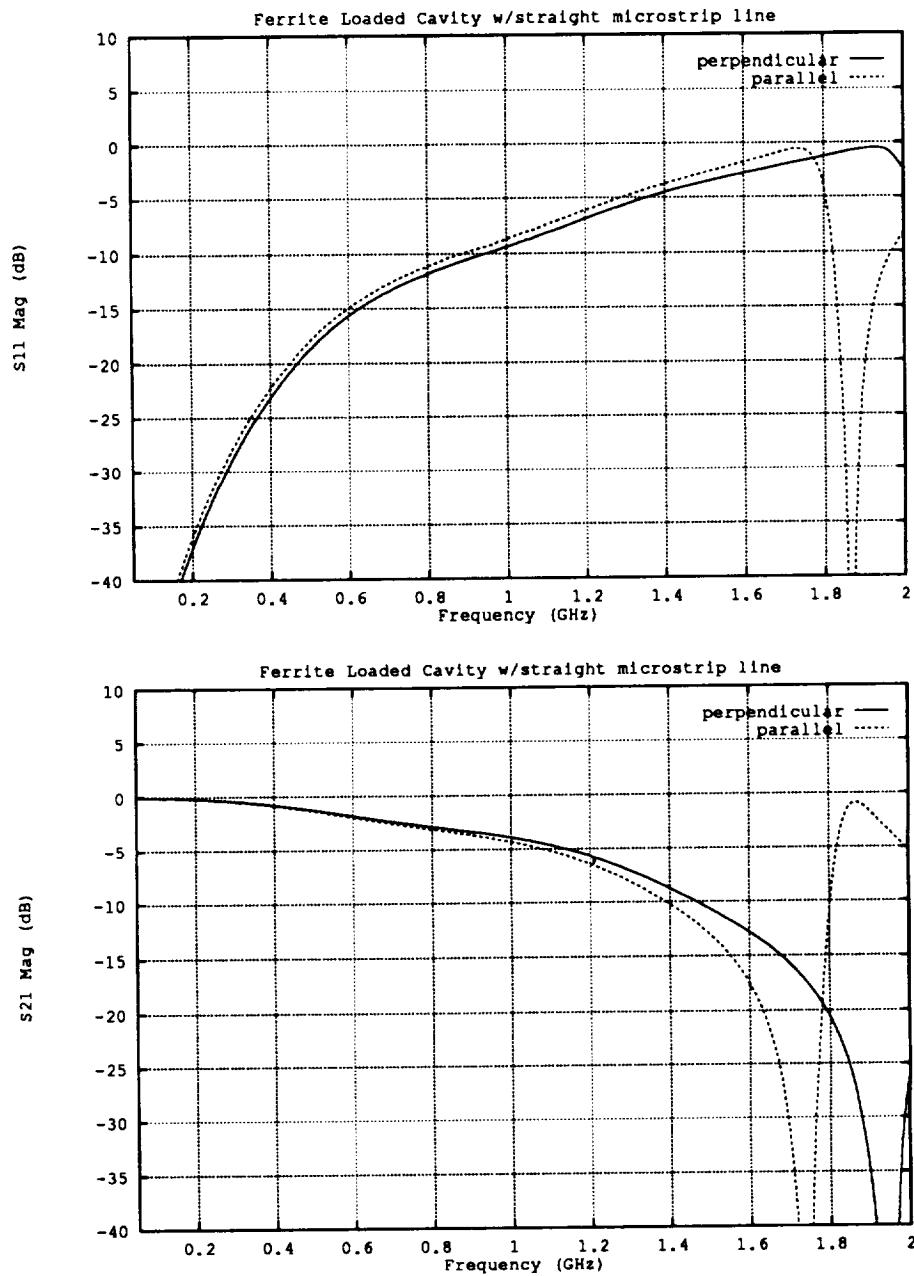


Figure 54: S_{11} and S_{21} of the Ferrite loaded cavity with the straight microstrip line.

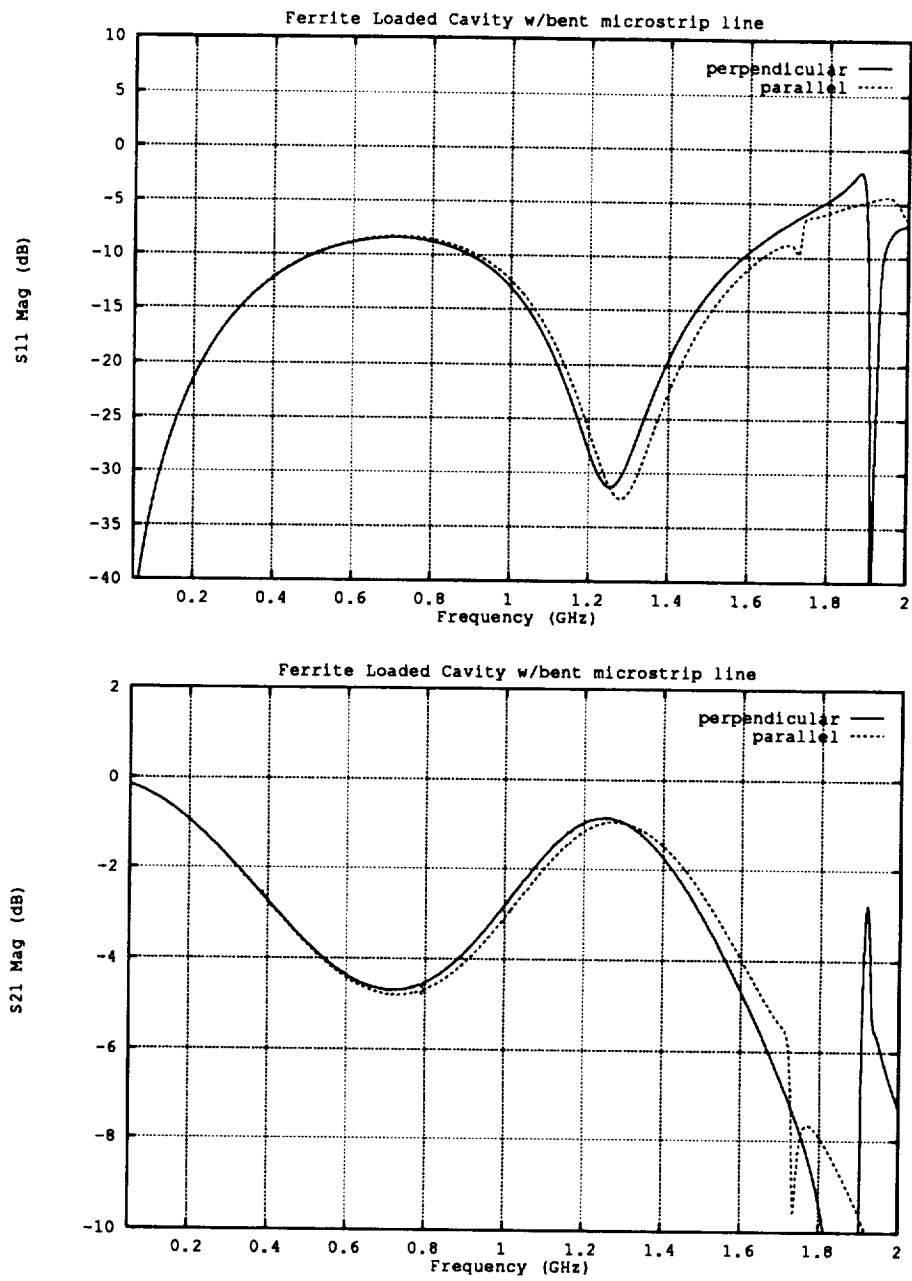


Figure 55: S_{11} and S_{21} of the Ferrite loaded cavity with the bent microstrip line.

References

- [1] Taflove, A. and Umashankar, K. R., "The Finite-Difference Time-Domain Method For Numerical Modeling of Electromagnetic Wave Interactions," *Electromagnetics*, Vol.10, pp. 105-126, Jan., 1990.
- [2] Kats, D. S. and Picket-May, M. J. and Taflove, A. and Umashankar, K. R., "FDTD Analysis of Electromagnetic Radiation from Systems Containing Horn Antennas," *IEEE Trans. on Antennas and Propagat.*, Vol. 39, pp. 1203-1212, Aug., 1991.
- [3] Tirkas, P. A. and Balanis, C. A., "Finite-Difference Time-Domain Method for Antenna Radiation," *IEEE Trans on Antennas and Propagat.*, Vol. 40, pp. 334-340, Mar., 1992.
- [4] Tirkas, P. A., Balanis, C. A. and Renaut, R. A., "Higher order absorbing boundary conditions for the Finite-Difference Time-Domain Method," *IEEE Trans. Antennas and Propagat.* Vol. 40, pp. 1215-1222, Oct., 1992.
- [5] C. A. Balanis, *Antenna Theory: Analysis and Design*. New York, John Wiley and Sons, 1982.
- [6] A.T. Adams, "Flush Mounted Rectangular Cavity Slot Antennas - Theory and Design," *IEEE Trans. Antennas and Prop.*, vol. AP-15, pp. 342-351, May 1967.
- [7] D.J. Angelakos and M.M. Korman, "Radiation from Ferrite Filled Apertures," *Proc. of the IRE*, vol. 44, pp. 1463-1468, October 1956.
- [8] M.A. Morgan, D.L. Fisher and E.A. Milne, "Electromagnetic Scattering by Stratified Inhomogeneous Anisotropic Media," *IEEE Trans. Antennas and Prop.*, vol. 35, no. 2, p. 191, Feb. 1987.
- [9] R.F. Harrington, *Time-Harmonic Electromagnetic Fields*, New York, New York, Mc-Graw Hill, Inc., 1961.
- [10] R.F. Harrington, *Field Computation by Moment Method*, Malabar, FL: Krieger, 1968.

- [11] M.M. Ney, "Method of Moments Applied to Electromagnetic Problems," *IEEE Trans. Micro. Theo. Tech.*, vol. MTT-33, no. 10, pp. 972-980, Oct. 1985.
- [12] E. El-Sharawy, "Full Wave Analysis of Printed Lines on Magnetic Substrates," Ph.D. dissertation, University of Massachusetts, 1989.